TWO-DIMENSIONAL INVESTIGATION OF VOID GROWTH AND COALESCENCE DURING DEFORMATION

TWO-DIMENSIONAL INVESTIGATION OF VOID GROWTH AND COALESCENCE DURING DEFORMATION

By

Jing Li, B. Eng

A Thesis
Submitted to the school of Graduate Studies in Partial
Fulfillment of the Requirements
for the Degree
Master of Science

McMaster University

Master of Science (2013) McMaster University

Department of Materials Science and Engineering Hamilton, Ontario

TITLE: Two-Dimensional Investigation of Void Growth and Coalescence during Deformation

AUTHOR: Jing Li, B. Eng (Zhengzhou University)

SUPERVISOR: Dr. David S. Wilkinson

NUMBER OF PAGES: xvii, 117

Abstract

Void growth and coalescence in a single layer model material with holes were visualized by the environmental electron scanning microscope coupled with in situ tensile test. Single sheet model materials were manufactured with a line of laser drilled holes through thickness. In order to investigate the effect of shear localization, the line of holes were oriented with the misorientation angle $\theta = 0°$, 15°, 30°, and 45°. The α-brass samples were studied to introduce the work hardening effect in comparison with the pure copper samples.

By taking images at intervals with small strain increments, the void growth behaviors were visualized during the interrupted tensile testing. The void coalescence (defined consistent with Hosokawa et al (2011), as the point at which the voids stopped shrinking laterally) was successfully captured for the first time in the two dimensional studies. The evolutions of void shape change and void rotation during deformation were also studied quantitatively. The results showed that the higher work hardening behaviors can suppress the void coalescence. It also showed that the effect of local volume fraction dominated the coalescence event rather than the void spacing and shear localization. A comparison of the classic models with the experimental results were also made.

Acknowledgements

I would like to express my sincere gratitude to my supervisor, Dr. David S. Wilkinson. It has been my great honor to work with him. Throughout all the stages of this project, I am indebted to him from his incredible knowledge and sharp mind in the field of mechanical behaviors of materials. He also taught me, consciously and unconsciously, to keep the natural passion and self-motivate attitude. His continuing guidance, encouragement and direction lead me to complete this work.

I am deeply grateful to Dr. Jidong Kang who offered constructive suggestions throughout this work. His assistance had a great influence on my understanding of this project. Dr. Akihide Hosokawa and Dr. Yaping Lue also provided valuable discussions and comments. Mr. Michael Nemcko kindly helped me to be familiar with all the facilities. As my good friend, he also showed me his wonderful life in Canada. I obtained enormous help from Ms. Connie Barry, Dr. Juan Kong, and Ms. Felicia Annor in the lab. I also wish to thank Mr. Klaus Schultes, Mr. Jim Garrett, Mr. Chris Butcher, Mr. Doug Culley, Dr. Xiaogang Li, and Mr. Ed McCaffery for their assistance in sample preparation and testing.

I especially want to thank my family for all of the years support and guidance. Thei0r understanding and love encouraged me to follow my heart and accomplish this work.

Table of Contents

List of Figures

List of Tables

Chapter 1

Introduction

Ductile fracture refers to the process during which materials break apart following a large amount of plastic deformation along with high energy absorption. In the history of fracture study, ductile fracture was regarded not as threatening as brittle fracture since it was not catastrophic and always gave warning before it was imminent. Thus, not as many efforts as the brittle fracture were put on investigating the mechanisms of the ductile fracture. The importance of understanding its nature has been realized in the past half century since most engineering metallic materials fail in the ductile manner. However, there is still a lack of experimental work to reveal its fundamental behavior especially the last stages of this process.

In the microscopic point of view, ductile fracture occurs through a successive progress by void nucleation, growth, and coalescence among which the last stage was the least understood. For decades, researches were limited to the ex situ, in another word, post linkage study after the fracture surfaces were formed. The detailed information on the growth and coalescence of micro voids has not been explored comprehensively not only in the simple two dimensional thin sheet case but also in the more complex three dimensional bulk case. Limitations for this situation are as follows:

Firstly, given the quality of imaging techniques, it was not possible to capture void coalescence during a continuous experiment. Unfortunately, void coalescence is a stochastic event and occurs over a small increment of strain. Thus, it is difficult to capture the coalescence event. Secondly, the processes of ductile fracture are continuous in engineering materials. When voids nucleate and grow to a critical condition, i.e., the threshold of size, shape, or spacing et al., they start to coalesce and link. Simultaneously, new voids nucleate and intervene in the process. Thus, it is essential to get rid of the effect of void nucleation on the study of void growth and coalescence.

Meanwhile, numerical models have been developed to predict the void growth manner and provide the coalescence criterion in the scope of different conditions and assumptions. However there is still great need for precise experimental results to validate and modify them.

The main objectives of this thesis are focused on the detailed growth and coalescence behavior of micro voids in the two dimensional thin sheet materials. The aims are as follows:

- To fabricate a series of 2-D thin sheet model materials containing ultrafast laser drilled voids with predefined arragnements.
- To visualize the sequences of void growth and capture the void coalescence of the model materials by utilizing interrupted in situ tensile testing.
- To extract the detailed dimensional changes from the SEM image and provide detailed quantitative evaluation for the classic void coalescence models.

A literature review of the ductile fracture mechanism and previous work are presented in Chapter 2 following this introduction. The experimental approaches are described in Chapter 3. Chapter 4 shows the experiment results obtained and corresponding discussions within which detailed comparison with the classic models are included. The final chapter summaries this thesis and addresses some future work.

Chapter 2

Literature Review

2.1 Ductile Fracture

Ductile fracture occurs by continuous processes of void nucleation, growth, and coalescence described by Garrison and Moody (1987). However, it is impossible to separate these processes when one stage ends and the next begins in the engineering materials. These process starts with microvoid nucleation at material inhomogeneities. Increasing the plastic deformation will then drive the voids to enlarge. When they are large enough to coalesce, elliptical cracks with the long axis perpendicular to the loading direction then form and propagate rapidly which lead to the tearing and failure of the material. As a result of the plastic deformation, a cup-and-cone fracture surface will typically form. During the substantial plastic deformation, a large amount of energy is stored.

2.1.1 Void nucleation

It is well known that voids initiate either by decohesion of the particle-matrix interface or fracture of the particle as shown in Figure 2.1. There has been extensive experimental work showing the effects of material parameters on void nucleation. The fracture of particles strongly depends on the shape of the particle, particle orientation, the strength of the particle-matrix bond et al. Also, the particle size, stress state, strength of the matrix material, and particle volume fraction et al. showed great impact on the particle-matrix decohesion (Garrison and Moody (1987)). Moreover, raising the temperature (Zhao et al. (1994)) and the hydrostatic pressure (Chen (1961), French and Weinrich (1974), Weinrich and French (1976)) will also postpone the nucleation event. Although the nucleation strain is used to quantify the void nucleation process, it is not an absolute value given the same type of particles. Rather the process is stochastic meaning that nucleation events occur continuously over a large range of strains. The competition of the matrix material strength and interface strength will have a critical effect on void nucleation.

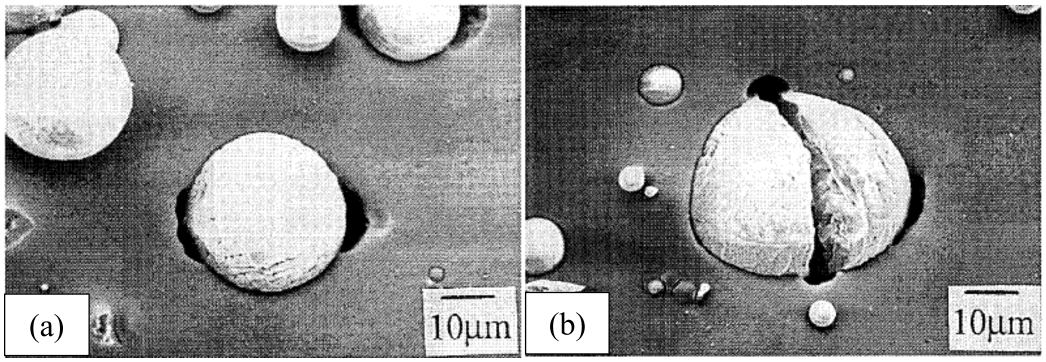

Figure 2.1: SEM micrographs of two damage nucleation mechanisms in metallic matrix composites (aluminum 6061 alloy matrix and spherical Al_2O_3 particles), (a) interface debonding and (b) particle cracking. Loading direction is horizontal. Kanetake et al. (1995).

2.1.1.1 Experimental investigations

Void nucleation is made of succession of discrete nucleation events which are normally associated with the existence of inclusions or second phase particles. It is effective to reveal the microstructure and keep track the behavior of the inclusions and particles during deformation. The traditional way to visualize the nucleation process is by taking images at various strain levels using optical or electron microscope which can help to provide two-dimensional information of the damage initiation on the surface. There have been miscellaneous experimental evidences based on this method (Puttick (1959), Argon and Im (1975), Argon et al. (1975), Goods and Brown (1979), Kanetake et al. (1995), Benzerga et al. (2004), Huber et al. (2005), Kadkhodapour et al. (2011)). By using the digital image correlation, the local strain corresponding to the nucleation strain can also be measured.

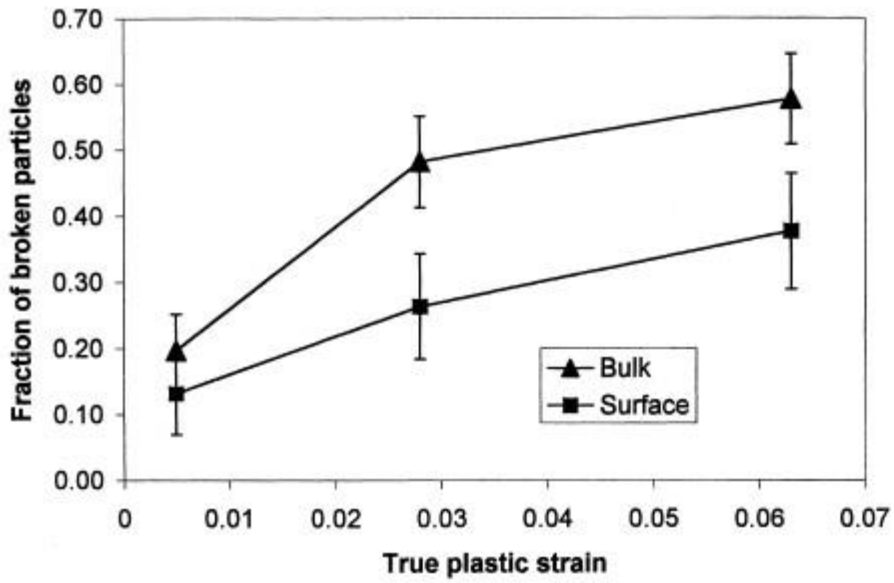

Figure 2.2: Fraction of particles broken by the plastic deformation as a function of the true plastic strain in the SiC reinforced 6061 Al alloy. Buffiere et al. (1999).

However, it has been challenging to present the nucleation event of the bulk sample using simple surface detection. And it has also been found that the circumstances on the surface and in the bulk are different. As shown in Figure 2.2 by Buffiere et al. (1999), the fraction of broken particles is found to be larger in the bulk than on the surface for all the investigated strains. Thus, it is essential and important to develop a new methodology to visualize the nucleation event in the bulk. Even though there are plenty of techniques to study ductile facture - for instance, ultrasound, serial sectioning (Weck et al. (2006)), and small angle X-ray scattering coupled with X-ray diffraction (Pan et al. (2010)) et al. X-ray computed tomography is the most sophisticated one. Babout et al. (2004) studied the effect of the matrix strength on the nucleation mode using X-ray tomography. They found that under the conditions of the same type and volume fraction of particles, decohesion preferred to occur in the soft pure aluminum matrix system whereas particle fracture was found more in the precipitate hardened Al 2124 matrix system as shown in Figure 2.3. After the development of X-ray computed tomography, there has been increasing visualization and quantitative measurements to reveal the nucleation process (Buffiere et al. (1999), Babout et al. (2001, 2004a, b), Maire et al. (2001), Gupta et al. (2009), Landron et al. (2010), Scheck and Zupan (2011), Taylor and Sherry (2012)).

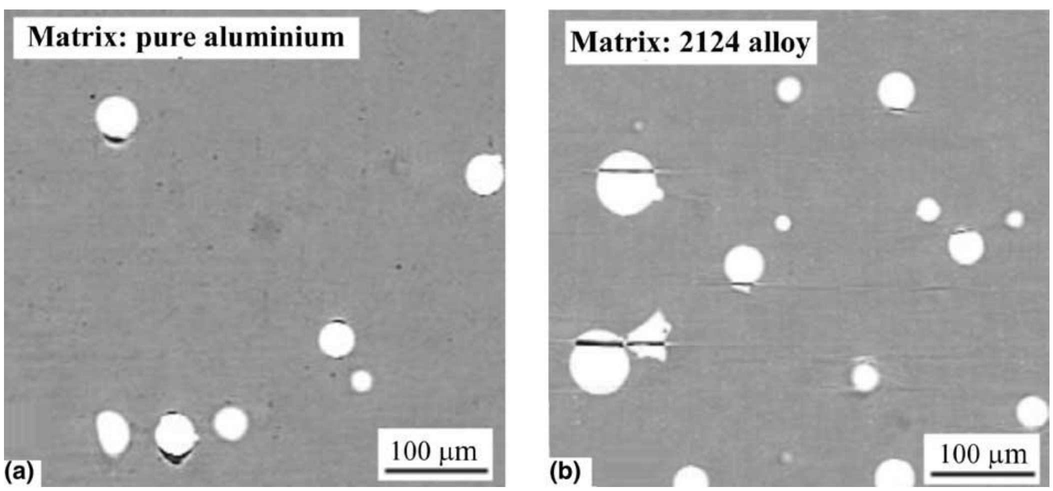

Figure 2.3: Reconstruction images from 3-D X-ray tomography showing decohesion in (a) Al + 4% ZrO_2/SiO_2 composite and particle cracking in (b) Al 2124(T6) + 4% ZrO_2/SiO_2 composite. Loading direction is vertical. Babout et al. (2003).

2.1.1.2 Models

Gurland and Plateau (1963) first proposed the condition for particle fracture based on the energy criterion when the strain energy released by particles can compensate the void surface energy. The applied stress σ for particle fracture was then given as follows:

$$\sigma = \frac{1}{q}\left(\frac{E\gamma}{a}\right)^{1/2} \tag{2.1}$$

where q is the stress concentration factor; E is the average Young's moduli of the particles; γ is the specific surface energy of the crack formed within the particle; and a is the particle diameter.

Since the size of the particles ranges from few nanometers to tens of micrometers, and the different theories depend on various scope of particle size, it is essential to separate the models by particle size.

For the small particles with radius $r < 1$ μm, the dislocation theory is required since the small particles can interact with dislocations. When particles radius r is larger than 1 μm, the continuum micromechanics model can apply (Brown and Stobbs (1976)). The dislocation density around the particle ρ is given by:

$$\rho = \frac{1.7\varepsilon_1}{rb} \tag{2.2}$$

where ε_1 is the macroscopic strain and b is the Burger's vector. And the local flow stress σ is given by:

$$\sigma = \alpha G b(\rho)^{1/2} = 1.3\alpha G\left(\frac{\varepsilon_1 b}{r}\right)^{1/2} \tag{2.3}$$

where α is a constant equal to 1/3 to 1/7 and G is the shear modulus. In addition, the presence of the particle increases the local stress on the interface of particle and matrix by a factor of 4.2 approximately. Therefore the elevated local stress can be given by:

$$\sigma_E = 5.4\alpha G\left(\frac{\varepsilon_1 b}{r}\right)^{1/2} \tag{2.4}$$

Therefore the critical condition for particle-matrix debonding is given by:

$$\sigma_c = \sigma_T = \sigma_E + \sigma_h + S_1 \tag{2.5}$$

where σ_c is the critical cohesive strength of the interfaces; σ_T is the maximum stress on the particle; σ_h is the hydrostatic stress; S_1 is the maximum deviatoric stress. So the nucleation strain by particle-matrix decohesion is shown as:

$$\varepsilon_1 = Kr(\sigma_c - \sigma_h)^2 \tag{2.6}$$

where K is the material constant. Thus, there is a linear relationship between the nucleation strain and the particle radius .

Argon et al. (1975) considered a circular cylindrical inclusion around both non-hardening and linear hardening plastic flow and proposed a stress based criterion for void nucleation by particle-matrix decohesion as expressed below:

$$\sigma_c = \sigma_m^{max} = \bar{\sigma} + \sigma_h \tag{2.7}$$

where σ_c is critical stress and σ_m^{max} is the maximum stress on the interface; $\bar{\sigma}$ is the equivalent or effective stress. Therefore a criterion without including any parameter on particle radius was developed. Besides the analytical modeling work described above, there are also some successful finite element modeling for void nucleation proposed (Needleman and Tvergaard (1987), Nutt and Needleman (1987)).

2.1.2 Void Growth

After nucleating either by decohesion or particle cracking, the voids appear in the shape of thin cracks and act as the stress concentrator in the bulk materials. Once nucleated, they grow immediately driven by the flow stress.

2.1.2.1 Experimental investigations

The original approach to visualize the void growth behavior is metallographic examination as the experiment carried out by Puttick (1959), Cox and Low (1974), et al. It can only provide limited information and the quality of surface refinement is critical. There was no high quality and comprehensive study for a long time until the utilizing of scanning electron microscopy coupled with in situ tensile testing.

Later, thanks to the development of computer assisted X-ray tomography (Hounsfield (1972), Cormack (1963, 1964)), it has been possible to investigate the void growth sequence (Figure 2.4) in the bulk materials (Babout et al. (2001), Ryzalla et al. (2005), Beckmann et al. (2007), Williams et al. (2010), Landron et al. (2011), Toda et al. (2011), Taylor and Sherry (2012)).

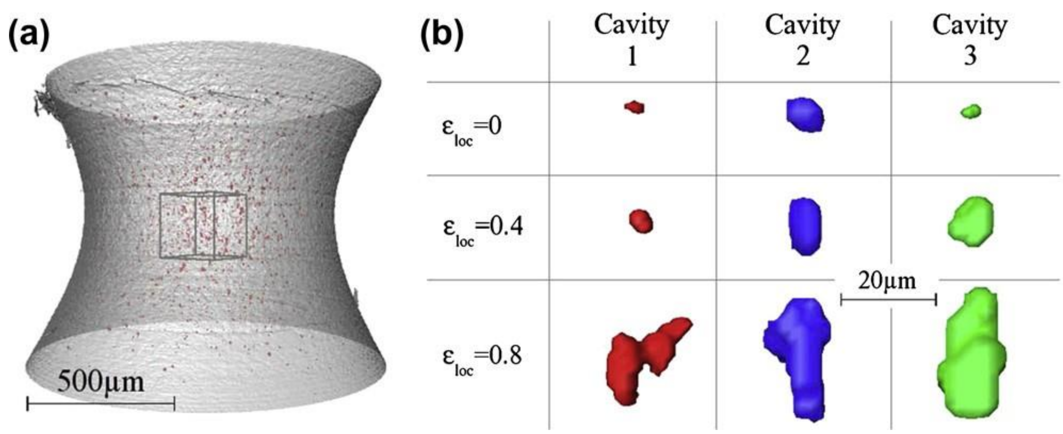

Figure 2.4: 3-D views of volumes obtained by tomography: (a) whole sample, with the outer surface shown in light gray and the outer surface of the cavities in dark gray; (b) three chosen cavities selected in the center of the sub-region where the morphology of the cavities was quantified (in the cube shown in (a)) at the center of a DP steel sample at various steps of deformation. Landron et al. (2011).

2.1.2.2 Models

It has been commonly accepted that at the beginning stage of the void growth, the voids extend individually without interacting with each other. Therefore numerical models for void growth were initially developed by the isolated voids in the infinite matrix without interaction between neighbor voids.

McClintock Model

The pioneer work was done by McClintock (1968a, b) who described the growth behavior of the isolated cylindrical void in a rigid perfectly plastic matrix (Figure 2.5) and then extended it for the elliptical holes. His simple model states that the void grow in a manner proportional to the applied strain and overestimates the fracture strain.

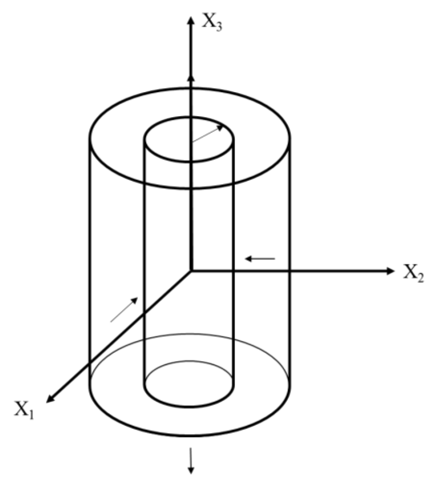

Figure 2.5: A cylindrical void in a representative volume element after McClintock (1968).

Rice and Tracey Model

Rice and Tracey (1969) developed the most successful void growth model of a spherical void with radius R as shown in Figure 2.6 in an infinite, rigid and perfectly plastic material under a uniform remote strain field ε_{ij} and remote stress field $\sigma_{ij} = S_{ij} + \sigma_m \delta_{ij}$. The strain rate was evaluated by defining a Lode variable ϑ:

$$\vartheta = -\frac{3\dot{\varepsilon}_2}{\dot{\varepsilon}_1 - \dot{\varepsilon}_3} \tag{2.9}$$

where $\dot{\varepsilon}_1 > \dot{\varepsilon}_2 > \dot{\varepsilon}_3$ are the principal components of the remote field.

In uniaxial tension and biaxial compression, $\vartheta = 1$;

In simple shear, $\vartheta = 0$;

In biaxial tension and simple compression $\vartheta = -1$.

The general form of the Rice and Tracey model can be described as:

$$\dot{R}_K = \left((1 + E)\dot{\varepsilon}_K + \left(\frac{2}{3}\dot{\varepsilon}_L\dot{\varepsilon}_L\right)^{1/2} D \right) R_K \tag{2.10}$$

where *K, L* = 1, 2, 3

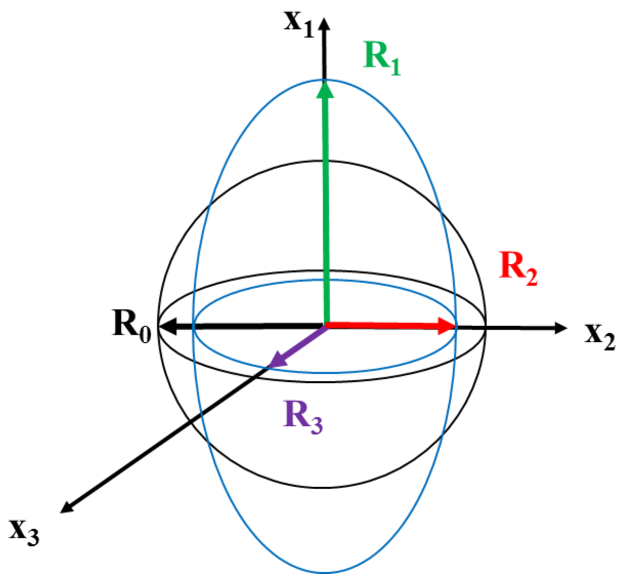

Figure 2.6: Schematic illustration of a spherical void growth into an ellipsoid by Rice and Tracey (1969).

In Equation 2.10, $(1+E)\dot{\varepsilon}_K$ corresponds to the shape change and is only affected by the deviatoric stress, and $\left(\frac{2}{3}\dot{\varepsilon}_L\dot{\varepsilon}_L\right)^{1/2} D$ corresponds to the volume change and is only affected by the hydrostatic stress. During deformation, the change in shape and volume of the void can be obtained in different deformation conditions and the spherical void initially will change into an ellipsoid. The principal radii of the ellipsoidal void can be calculated as a function of strain as:

$$R_1 = \left(A + \frac{(3+\upsilon)}{2\sqrt{\upsilon^2+3}} B \right) R_0 \tag{2.11}$$

$$R_2 = \left(A - \frac{\upsilon}{\sqrt{\upsilon^2 + 3}} B \right) R_0 \tag{2.12}$$

$$R_3 = \left(A + \frac{(\upsilon - 3)}{2\sqrt{\upsilon^2 + 3}} B \right) R_0 \tag{2.13}$$

where

$$A = \exp\left(\frac{2\sqrt{\upsilon^2 + 3}}{(3 + \upsilon)} D\varepsilon_1 \right) \tag{2.14}$$

$$B = \left(\frac{1 + E}{D} \right)(A - 1) \tag{2.15}$$

$1 + E \approx 5/3$ for linear hardening materials and low values of σ_m with non-hardening materials;

$1 + E \approx 2$ for large values of σ_m with non-hardening materials;

$D = 0.75\frac{\sigma_m}{Y}$ for linear hardening materials;

$D = 0.558\ Sinh\left(\frac{3}{2}\frac{\sigma_m}{Y} \right) + 0.008 Cosh\left(\frac{\sigma_m}{Y} \right)$ for non-hardening materials.

In uniaxial tension, substituting equation (2.14) and (2.15) into (2.11), (2.12), and (2.13), the principal radii can be obtained as:

$$R_1 = \left(exp\left(D\varepsilon_1\right) + \frac{\left(1+E\right)}{D}\left(exp\left(D\varepsilon_1\right) - 1\right) \right) R_0 \tag{2.16}$$

$$R_2 = R_3 = \left(exp\left(D\varepsilon_1\right) - \frac{\left(1+E\right)}{D}\ \left(exp\left(D\varepsilon_1\right) - 1\right) \right) R_0 \tag{2.17}$$

The Rice and Tracey model has been used to model the void growth on various systems. An example was shown by Le Roy et al. (1981).

Gurson model

Gurson (1977) developed a micromechanical model derived from a similar analysis to the Rice and Tracey model for an isolated void based on a simplified spherical cell with a void. The estimation of the yield function for the porous material was given and used to derive the plastic flow direction. The yield surface is given as follows:

$$\emptyset = \frac{\sigma_n^2}{\sigma_{ys}^2} + 2f\cosh\left(\frac{3\sigma_m}{2\sigma_{ys}}\right) - (1 - f^2) = 0 \tag{2.18}$$

where f is the initial porosity and σ_n, σ_{ys}, and σ_m are the von Mises equivalent stress, yield stress and mean normal stress respectively. When $f = 0$, this yield surface is identical to the von Mises criterion. Following the theoretical analysis of Gurson (1977), it has been found that the yield surface cannot predict the fracture and coalescence event compared with experimental results. A lot of extended works was then performed. One of the most successful extension is the model proposed by Tvergaad and Needleman (1984). Several new parameters were introduced to allow a more accurate description of the void growth kinetics thus this model is often referred to as the Gurson-Tvergaad-Needleman (GTN) model.

2.1.3 Void Coalescence

Models of ductile fracture generally assume that the particle size, shape, spacing, and distribution are uniform and the nucleation of voids occurs at all particles simultaneously. In reality, particles in materials are not uniform and there are pre-existing voids due to manufacturing process. Therefore the void nucleation event occurs all along the deformation process. As long as some certain voids grow large enough or the critical spacing is reached, the coalescence will be triggered. Therefore, large voids coalesce first during the deformation, overlapping with new void nucleation and growth, which makes the nucleation and growth neither separable nor sequential. For void coalescence alone, it has become the most stochastic event and rather difficult to capture experimentally. Meanwhile, void coalescence controls the final stage of failure and the coalescence strain is so close to final fracture strain that separating coalescence and final fracture is very difficult. As a consequence, there is limited experimental and quantitative data to reveal the nature of this event.

As classified by Garrison and Moody (1987), void coalescence occurs either by internal necking (also known as void impingement) or void sheeting in which shear bands are formed. Puttick (1959) observed the typical internal necking behavior in pure copper (99.9%) where the ligament between voids neck down to a point as shown in Figure 2.7 (a). When there are different classes of particles, as the classic example in the AISI 4340 Steel system studied by Cox and Low (1974), the coalescence of large voids initiated at manganese sulfide inclusions has been accelerated by the formation of a collection of small voids at carbide precipitates as shown in Figure 2.7 (b). This is the result of deformation concentration in the narrow bands (generally oriented at approximately 45 degree with the tensile direction) between the main voids after the critical size or spacing between them is reached. In addition, void sheeting can also occur without the secondary particle population, thus, the requirement for void sheeting is that voids nucleate and coalesce in the localized shear region (Garrison and Moody, (1987)).

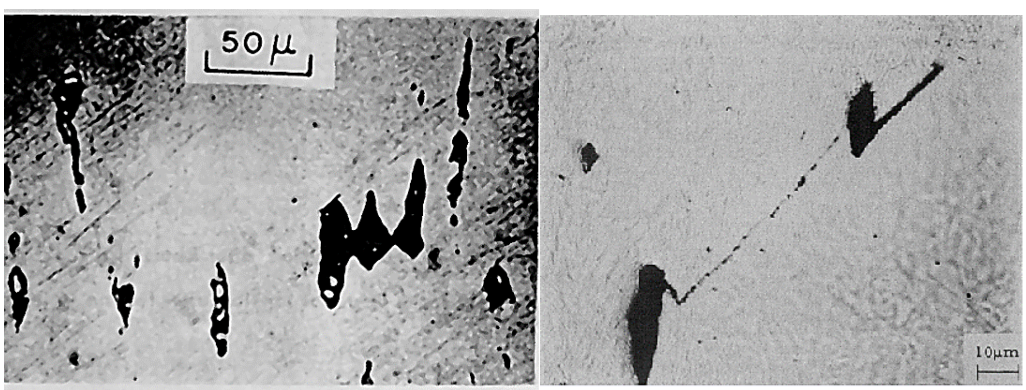

(a) (b)

Figure 2.7: Micrographs of (a) internal necking in the Copper. Puttick (1959). (b) Void sheeting in AISI 4340 Steel. Cox and Low (1974).

Faleskog and Shih (1997) showed that when a secondary population of voids was located in the shear band joining the primary voids, the thickness of the shear band was controlled by the size of the secondary voids as shown in Figure 2.8. Although the shear controlled void sheeting mechanism is quite important, there is still a lack of quantitative work on it. Because of the difficulties of experimental work, a lot efforts has been put in modelling of void coalescence event.

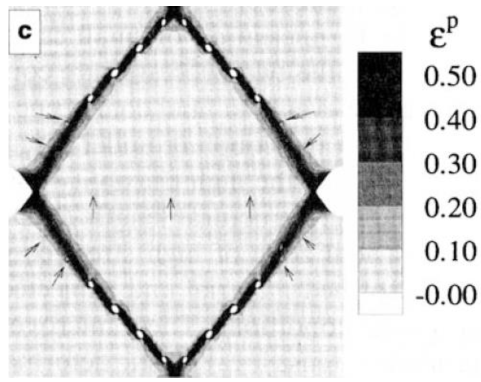

Figure 2.8: Void sheeting mechanism involving large primary voids and a secondary population of small voids for low strain biaxiality and low work hardening exponent. Faleskog and Shih (1977).

McClintock Model

McClintock (1968) provided an analytical solution for the expansion of a cylindrical void in a strain hardening cylindrical representative volume element (RVE) as shown in Figure 2.5. It indicates that the ductile fracture occurs when the lateral diameter of the voids grow to half of the mean spacing, in other words, void impingent with each other as shown in Figure 2.9. This theory ignores the interactions of the voids and the deformation localization process and therefore overestimates the fracture strain.

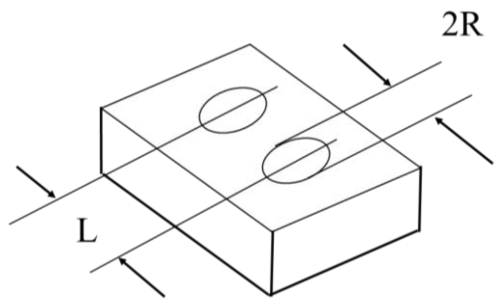

Figure 2.9: Strain plane of a cube containing two holes coalescing. McClintock (1968).

Brown and Embury Model

Brown and Embury (1973) established a brief model indicating that coalescence occurs when the length of the elongated holes is equal to their spacing, so the shear bands at 45° can form as shown in Figure 2.10. According to the Brown and Embury analysis, nucleating with a radius of r_0, voids grow to the length of $2r_0(1+\varepsilon_g)$ with a further strain of ε_g. Given the void nucleation strain ε_n and void volume fraction V_f, the failure strain ε_f can be expressed as:

$$\varepsilon_T = \ln\frac{A_0}{A_f} = \ln\left(1+\varepsilon_g+\varepsilon_n\right) = \ln\left(\sqrt{\frac{\pi}{6V_f}} - \sqrt{\frac{2}{3}} + \varepsilon_n\right) \qquad (2.19)$$

where

$$2r_0\left(1+\varepsilon_g\right) = r_0\left(\sqrt{\frac{2\pi}{3V_f}} - \sqrt{\frac{8}{3}}\right) \qquad (2.20)$$

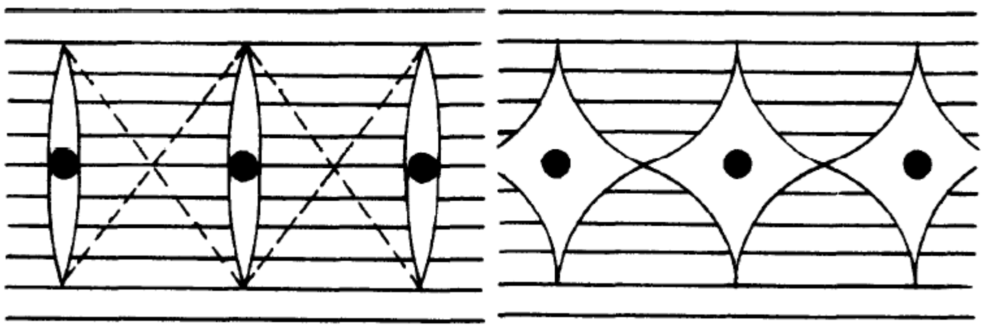

Figure 2.10: (a) Schematic illustration of condition for the onset of local necking and (b) illustration of the cross section after local necking. Brown and Embury (1973).

This model does not consider the triaxiality component and generally overestimates the fracture strain. A modified version considering the triaxiality component was given later by Le Roy et al. (1981).

Thomason Model

Thomason (1968, 1990) proposed the onset of void coalescence condition in two-dimensions (Figure 2.11 (a)) based on the plane strain model. The incipient limit-load condition for internal necking can be reached when the following equation is verified:

$$\left(\frac{0.3A_{n-2D}}{a/c(1-A_{n-2D})}+0.6\right)\left(1-V_f\right)^{-1}=\frac{\sigma_m}{Y}+\frac{1}{2} \tag{2.21}$$

In this equation, the meanings of each parameters are listed below:

A_{n-2D} – area fraction of intervoid matrix, $A_{n-2D} = e/W$;

$2e$ – edge to edge distance between holes;

$2W$ – center to center distance between holes;

$2a$ – length of the hole;

$2c$ – diameter of the hole;

V_f – initial void volume fraction, $V_f = (\pi / 4)(c_0 / W_0)^2$;

σ_m/Y – stress triaxiality;

σ_m – mean stress;

Y – plastic equivalent stress.

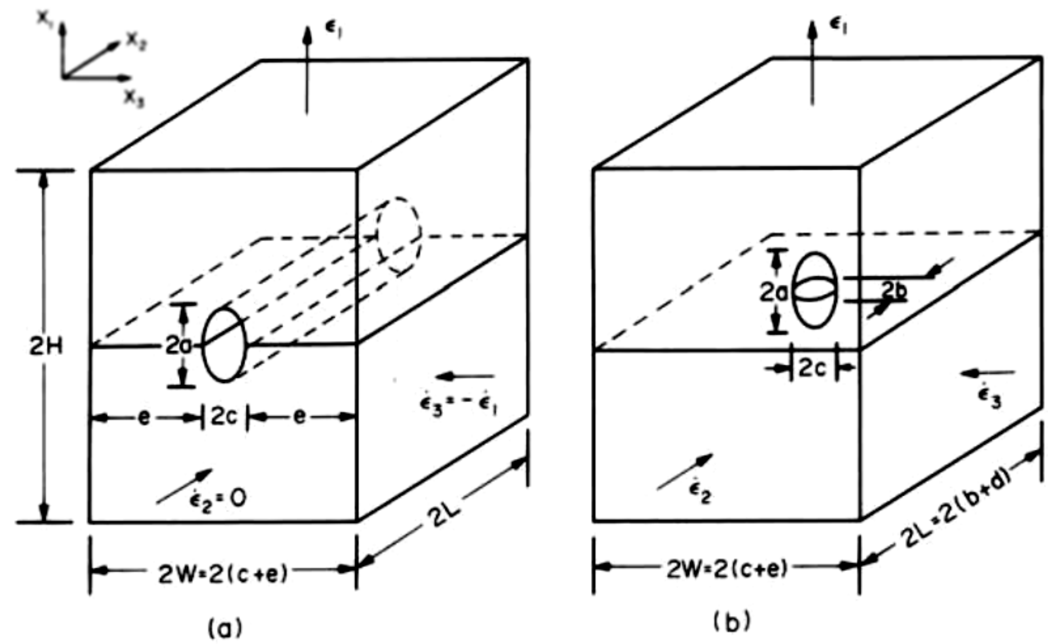

Figure 2.11: (a) Two-dimensional condition with prismatic elliptical void and (b) three-dimensional condition with ellipsoidal void in unit cells. Thomason (1990).

As shown in Figure 2.11 (b)), the 3-D criterion (Thomason (1985a, b, 1990), by limit load condition assuming an initially cubic unit cell containing a spherical void is given by Equation 2.22:

$$\left(\frac{0.1}{\left(\frac{a}{d}\right)^2}+\frac{1.2}{\left(\frac{b}{b+d}\right)^{1/2}}\right)\left(1-V_f\right)^{-1}\left(1-\left(\frac{3\sqrt{\pi}V_f}{4}\right)^{2/3}\left(\frac{b}{b_0}\right)^2\right)exp(\varepsilon) = \frac{\sigma_m}{Y}+\frac{1}{2} \tag{2.22}$$

In this equation, the geometry factors of b, b_0, and d are added and ε is the applied tensile plastic strain. The surface to surface intervoid distance is then determined by the following equation:

$$d = a_0\left(\sqrt[3]{\frac{\pi}{6V_f}}\right)exp\left(-\frac{1}{2}\varepsilon\right) - \left(\frac{b}{b_0}\right) \tag{2.23}$$

and the initial void volume fraction V_f is estimated by:

$$V_f = \frac{V^{void}}{V^{cell}} = \frac{V^{void}}{(2a+2d)(2b+2d)(2c+2d)} \tag{2.24}$$

where V^{void} is the volume of a single void and V^{cell} is the volume of a unit cell including the void.

Pardoen and Hutchinson Model

Pardoen and Hutchinson (2000) modified the Thomason model by including the effect of work-hardening. They introduced two exponents α and β into Equation (2.24) where $\beta(n)$ is almost constant and can be taken as 1.24 and

$$\alpha(n) = 0.1 + 0.217n + 4.83n^2 \quad (0 \leq n \leq 0.3) \tag{2.25}$$

Thus, the equation given by Pardoen and Hutchinson is as:

$$\left(\frac{\alpha(n)}{\left(\frac{a}{d}\right)^2}+\frac{\beta(n)}{\left(\frac{b}{b+d}\right)^{1/2}}\right)\left(1-V_f\right)^{-1}\left(1-\left(\frac{3\sqrt{\pi}V_f}{4}\right)^{2/3}\left(\frac{b}{b_0}\right)^2\right)exp(\varepsilon) = \frac{\sigma_m}{Y}+\frac{1}{2} \quad (2.26)$$

Besides these classical models, Gammage et al. (2004) also proposed a model for the coalescence based on penny shaped cracks in metal matrix composites incorporating Thomason's limit load condition. The coalescence criterion is reached when the far field work hardening rate θ is equal to the stress acting between two penny shaped voids with a distance λ as shown:

$$\theta = \sigma_a\left(1+\alpha\sqrt{\frac{a}{\lambda}}\right) \quad (2.27)$$

where σ_a is the far field applied stress, a is the average particle diameter, and α is the stress concentration factor of the order 2. This model simply assumed the far field work hardening rate is equal to the local work hardening rate in the intervoid matrix. Nevertheless, it showed good agreement with the experimental data for the penny shaped voids coalescence in a metal matrix composite.

Besides the models described above, void coalescence by internal necking has also been studied using numerous finite element simulations (Koplik and Needleman (1988), Worswick and Pick (1990), Brocks et al. (1995), Kuna and Sun

(1996), Pardoen and Hutchinson (2000)).

2.1.4 Summary

It has been acknowledged that the ductile fracture process consists of the void nucleation, growth, and coalescence. There is still lack of quantitative experimental study for void coalescence especially for the shear localization mechanism. Moreover, a lot more attention should be paid to develop more accurate and reliable models considering the shear effect.

2.2 Previous Work Done by the Wilkinson Group at McMaster

2.2.1 Model materials fabrication

As mentioned above, void coalescence controls the failure process of the metallic materials. However, the understanding of this process is limited because of the interruption of void nucleation all through the deformation process. To solve this problem, efforts have been put on fabricating model materials with pre-existing holes to eliminate the void nucleation process.

Magnusen et al. (1988), Nagaki et al. (1988), and Jia et al. (2002) fabricated model materials by drilling holes through metallic sheets in order to eliminate the void nucleation process. The holes were controlled to be arranged as shown in Figure 2.12. However the size of holes were approximately 1 mm which was much larger than those found in real materials (1 to 50 μm) (McClintock (1968b)). Also, their methodology was limited to the simple two dimensional SEM imaging.

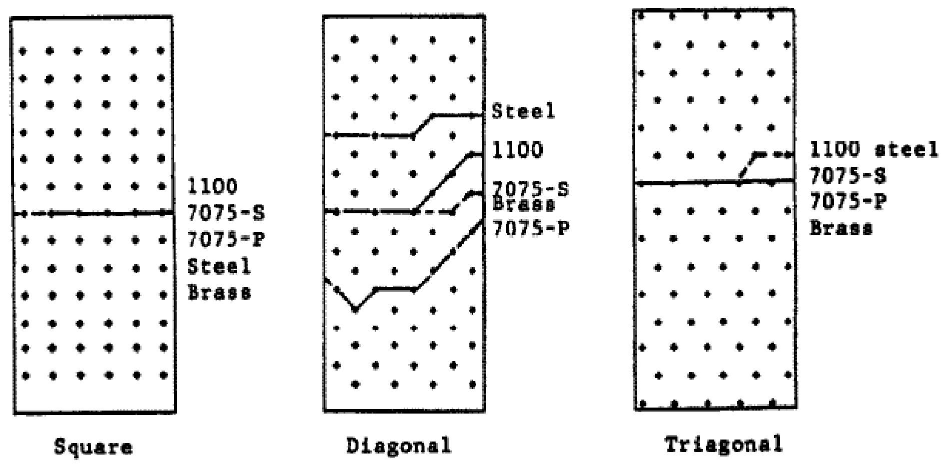

Figure 2.12: Regular hole arrays drilled in different sheet materials. Magnusen et al. (1988).

In order to overcome these problems, Weck et al. (2006) proposed a way to fabricate new model materials using a femtosecond laser to drill holes in the foil materials. The size of the holes were controlled to be comparable with the holes detected in practice (1 to 50 μm). A single sheet model material (Figure 2.13(a)) is eligible for characterization in SEM under in situ uniaxial tensile test. Once embedded with two hole-free sheets (Figure 2.13(b)), it was made very close to the reality, i.e., voids in the bulk with artificial configurations.

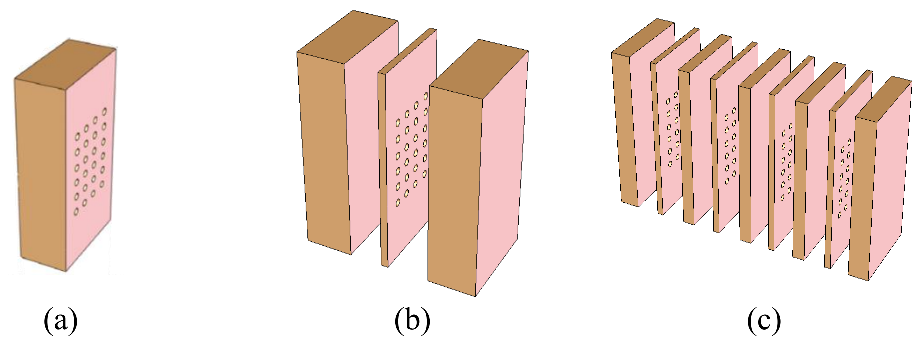

Figure 2.13: Schematic drawing of (a) 2-D single sheet (b) 3-D single sheet (c) 3-D multiple sheets model materials. Weck et al. (2006).

Using the X-ray tomography techniques, the behavior of each void in bulk can be detected and recorded during the interrupted tensile test when the test is stopped at intervals. Hosokawa et al. (2013a, b, and c) also fabricated model materials of multiple layers (Figure 2.13 (c)) with controllable stacking order of voids in different layers. Different methods of image collecting during the tensile test were shown in Figure 2.14.

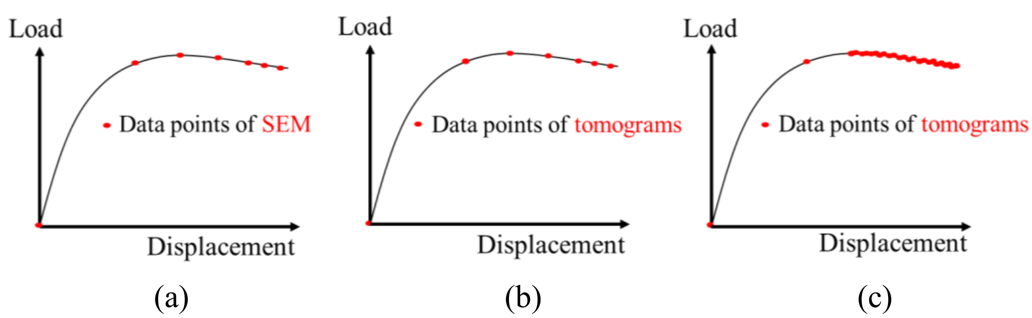

Figure 2.14: Schematic diagram of data collection mode in (a) interpreted in situ SEM, (b) interpreted in situ X-ray tomography, and (c) continuous in situ X-ray tomography.

2.2.2 Selected findings from the work of Weck et al.

2.2.2.1 Visualization of void growth and coalescence in 2-D single-sheet model materials

By taking a series of images during the interrupted in situ tensile test, Weck and Wilkinson (2008) visualized the growth and linkage behavior of two voids and array of voids in 2-D single sheet model materials as shown in Figure 2.15.

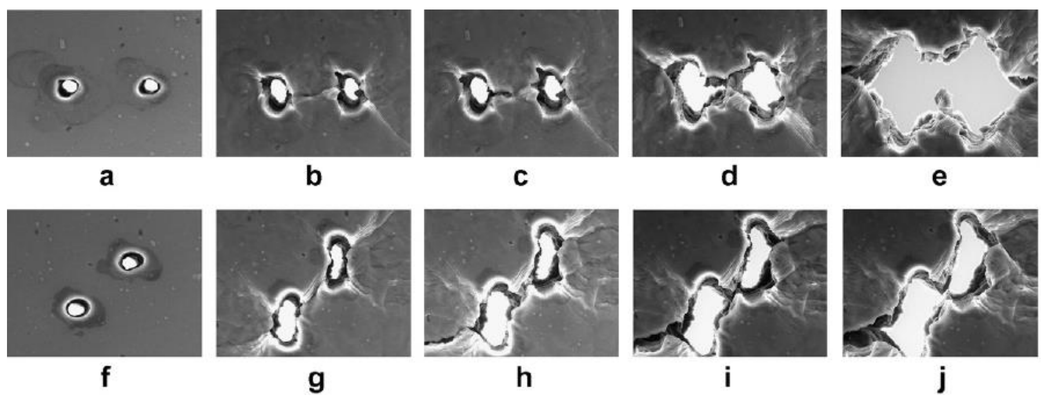

Figure 2.15: In situ SEM images of the deformation sequence of AA 5052. Two holes oriented at 90° (a ~ e) and 45° (f ~ j) with respect to the tensile direction. Weck and Wilkinson (2008).

The coalescence defined in their work was the point of ligament failure which was actually the concept of "linkage". From the quantitative analysis and comparison with classic models, they found that the McClintock void growth model can only predict behavior at low applied strain level because of it ignores voids interaction. Brown and Embury model was in excellent agreement with experimental results except for those voids whose arrangement angle was 45° with respect to the tensile direction and whose spacing was close. Moreover, the

Thomason model seemed not to work well in this case.

2.2.2.2 Visualization of void growth and coalescence in 3-D single-sheet model materials

3-D single sheet model materials were also been fabricated as shown in Figure 2.16. One sheet with laser drilled holes was embedded with two hole-free sheets by diffusion bonding, and the copper and Glidcop-Al 25 samples were pulled in tension in the interrupted in situ tomography test. Not surprisingly, Weck et al. (2008) found that the Brown and Embury model was no longer valid in the 3-D case, because the model did not consider the constraint on the holes in bulk by the hole-free materials. However, the Thomason model gave excellent prediction for copper sample with void arrays normal to the tensile direction. It however failed to predict the 75° case because of the constraint factor in Thomason model was not defined for arbitrary angles. In the Glidcop case, the secondary voids formation was considered to play a role on reducing the coalescence strain which made the prediction poor.

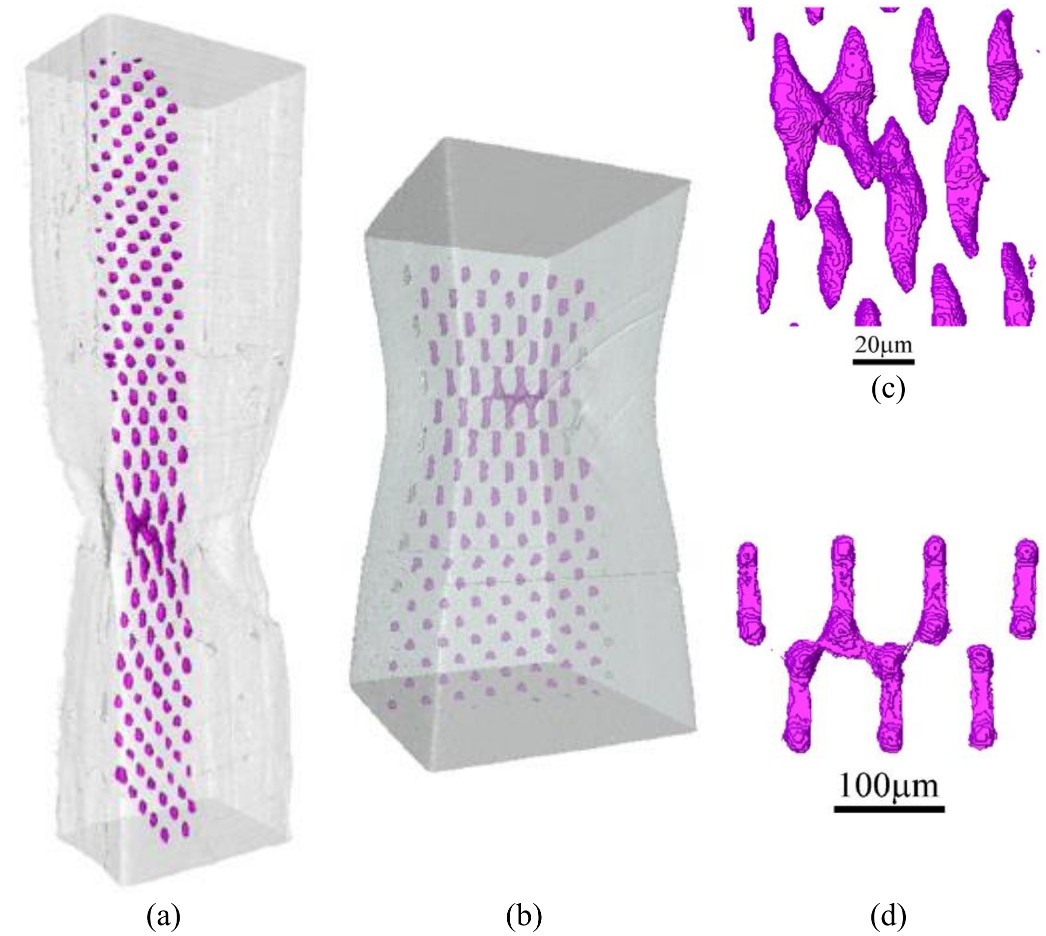

Figure 2.16: Tomographic reconstruction of (a) copper and (b) Glidcop sample containing an array of laser drilled holes 45° with respect to the tensile direction (vertical) at the coalescence stage. Close-up image of the first coalesced voids of (c) copper and (d) Glidcop sample. Weck et al. (2008).

2.2.2.3 Remaining problems

Firstly, to fabricate the 3-D model materials with multiple layers, Weck et al. (2008) bound the stack of the sheets before laser drilling which made it impossible to remove the oxide layer on the surface. As a result, there was a severe delamination problem in the 3-D model materials. Secondly, the coalescence concept used in Weck and co-workers' work (2008) was actually based on linkage which is the later stage after coalescence. The coalescence far field strain and local strain stated in his work were larger than the real ones. Thirdly, Weck and Wilkinson (2008) fabricated the model materials containing void array with 90° and 45° with respect to the tensile axis in order to explore the two different types of coalescence, i.e., internal necking and shear localization. However, only these two configuration were studied and there was a need of a more comprehensive experimental exploration of this difference.

2.2.3 Selected findings from the work of Hosokawa et al.

2.2.3.1 Capture of the onset of void coalescence using continuous X-ray tomography

As mentioned above, void coalescence is a rather stochastic event which occurs in a small strain increment and is not so discernable during the tensile test. In a typical image acquisition process, the tensile machine has to be stopped and the sample detected has to remain stable to prevent blurring. Thus it is difficult to capture it using the traditional imaging approaches. Maire et al. (2007) first proposed the application of fast tomography during the tensile test which allows the non-stop imaging to be conducted. By using this technique, Hosokawa et al. (2013a) first captured the onset of void coalescence ever as shown in Figure 2.17 by measuring the intervoid distance at which moment the lateral shrinking stopped.

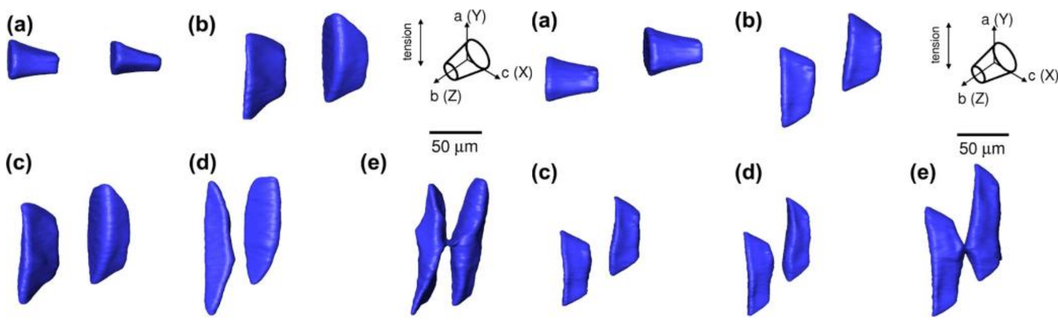

(A) (B)

Figure 2.17: Growth and linkage behavior the first void pair to coalesce at increasing strain increments extracted from the tomograms in the (A) FCC1 model materials at strain ε = 0, 0.44, 0.51, 0.61, 0.96 and (B) FCC2 model materials at strain ε = 0, 0.44, 0.52, 0.64, 0.78. Hosokawa et al. (2013a).

2.2.3.2 Effect of void orientation

Hosokawa et al. (2013a) fabricated two different types of multi-layer 3-D model materials with various packing orders in order to introduce the effect of void orientation as shown in Figure 2.18. The coalescence and linkage was found to occur through thickness (b axis in Figure 2.17). Because of the shear effect, void coalescence was enhanced and the internal necking started earlier in the FCC2 sample (Figure 2.17(B)(d)) than the FCC1 sample (Figure 2.17(A)(d)) at comparable strain level (ε ~ 0.51). In addition, the coalescence and linkage strain were found to be larger for the FCC1 sample than the FCC2 sample. The influence of the misalignment angle θ on the plastic constraint factor (PCF) required for localization was studied under the 2-D plane strain condition.

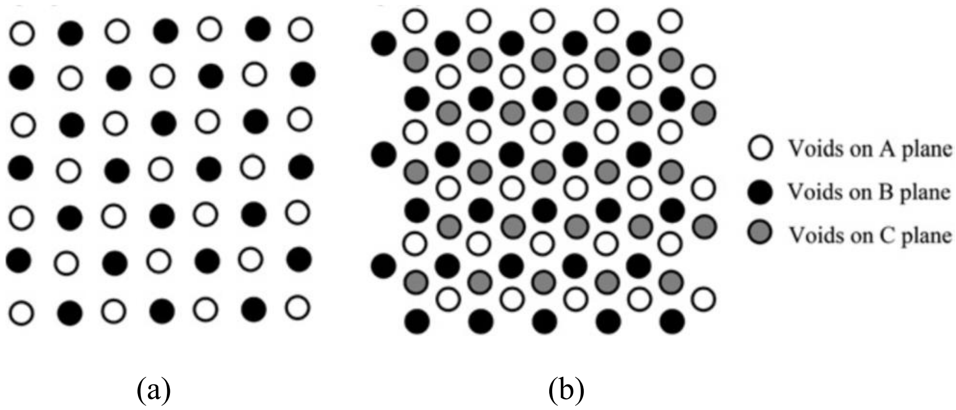

Figure 2.18: Schematic illustrations of the three dimensional void array in (a) FCC1 and (b) FCC2. The tensile direction is vertical.

The PCFs within imaginary localized ligaments were estimated by finite element simulations. By taking a similar approach to that of Bannister and Ashby (1991), the PCF for shear localization between misaligned voids was then recomposed as follows:

$$\frac{\sigma_n}{2\mathrm{k}} = \frac{1}{2\sin\theta} \tag{2.28}$$

The idea of effective shear angle was adopted by considering not only the shear angle θ but also the neck geometry parameter *a/d* as shown in Figure 2.19.

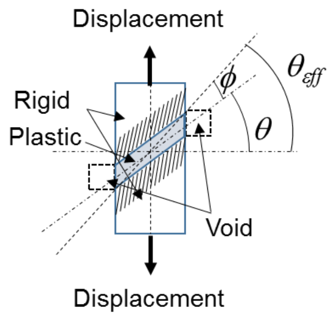

Figure 2.19: The imaginary localization between a misaligned pair of voids considering the effective shear angle. Hosokawa et al. (2013a).

The effective shear angle θ_{eff} is then the sum of the original misorientation angle θ and the angle formed in the plastic region by a diagonal line $\phi = tan^{-1}\left(\frac{a}{d}\right)$. Therefore, a simple model to express the PCF for shear localization is shown as follows:

$$\frac{\sigma_n}{2\mathrm{k}} = \frac{1}{2\sin\theta_{eff}} = \frac{1}{2sin\left(\theta + tan^{-1}\left(\frac{a}{d}\right)\right)} \tag{2.29}$$

2.2.3.3 Remaining problems

Firstly, to fabricate 3-D multi-sheet model materials and overcome Weck's problems, Hosokawa et al. (2013a, b) tried to use a mold with a square prismatic hole to hold the sheets layer by layer to align the voids in certain orders. However, since the void diameter and intervoid distance were ten or tens of micrometers and machining precision of the mold and the sheet materials could not meet the accuracy requirement, there was some misalignment among the sheets as shown in

Figure 2.20. Consequently, voids located in different sheets were closer than the designed distance and the first pair of voids to coalesce were always the voids in adjacent sheets. More efforts have to be taken in order to find an effective method to get not only a clean surface but also a proper alignment. Secondly, the effort to study the impact of shear angle in the 3-D model materials is commendable. However, as the complexities addressed above, it is necessary to come back to the simple 2-D case in order to better control the positions of the voids and this is the origin of the current work.

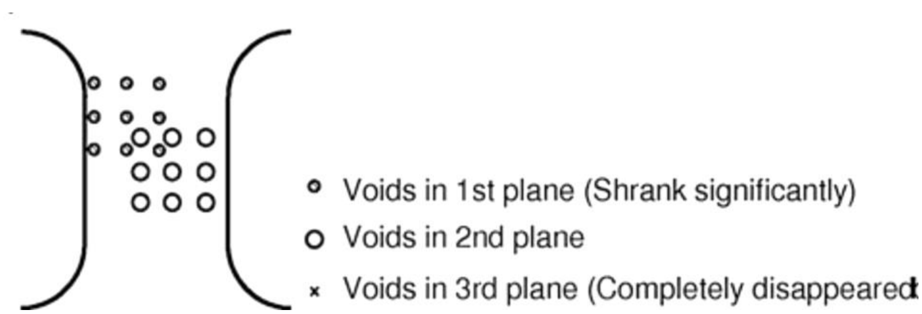

Figure 2.20: Schematic illustration of one of the serious misalignment cases in brass rectangular model materials. Hosokawa et al. (2013b).

From the results of FCC2 samples, the shear effect needs to be included in any analysis of the system compared with the internal necking mechanism in FCC1 samples. It is believed that the shear angle can be controlled by changing the relative positions of the voids, i.e., the orientation of the void array. Due to the lack of knowledge of the shear effect on coalescence, it is important to investigate it by a series of studies with various void orientations.

Chapter 3

Experimental Approach

3.1 Materials

The materials were chosen to consider different properties. Commercial high purity copper (99.999%) purchased from the Alfa Aesear Company was selected because of high ductility which allows large deformations in order to capture the fracture events. α-brass (Cu:Zn = 7:3) has a remarkable work hardening rate compared to copper because of its low stacking fault energy ($\gamma_{Cu} = 78$ mJ/m^2 and $\gamma_{brass} = 14$ mJ/m^2, Murr (1975)), thus was used to study the effect of work hardening.

The α-brass sample was also purchased from Alfa Aesear Company.

3.2 Sample Preparations

The process of sample preparation was shown in Figure 3.1. Raw sheet materials above were cut into tensile samples by electrical discharge machining (EDM). Due to the low volume fraction of the laser drilled holes, the sample with double notches was designed so that fracture events would occur at the section containing the void as shown in Figure 3.2.

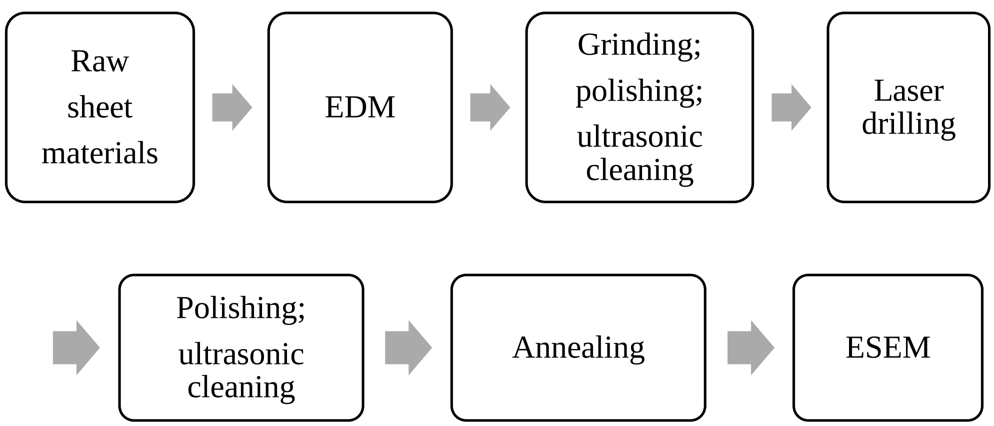

Figure 3.1: Sample preparation process.

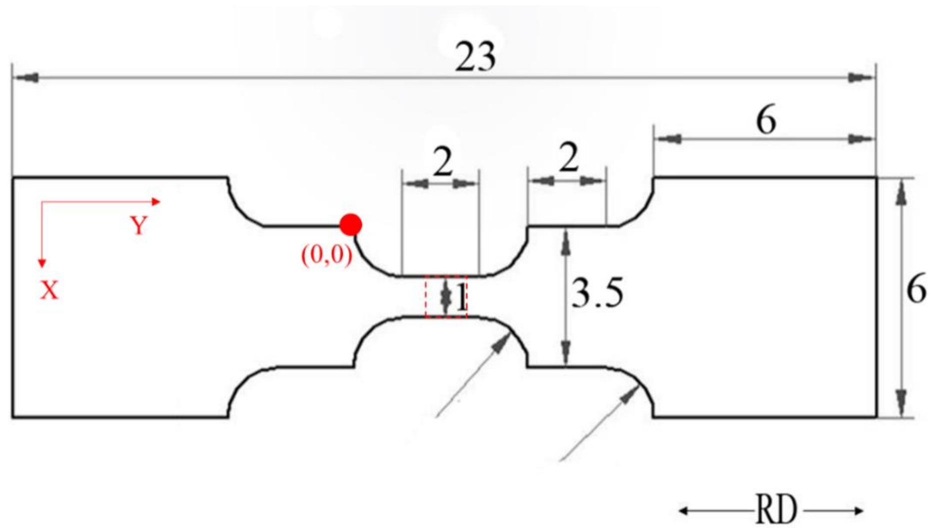

Figure 3.2: Drawing of the tensile samples by EDM with respect to the rolling direction (RD) of the raw materials. Note that the sample is symmetric about the X and Y axis and the dimensions are in millimeters. All radii are 1.25 mm. The dash square indicates the position of laser drilled holes.

3.2.1 Laser drilling

Similarly with the work done by Weck (2007) and Hosokawa (2011), ultra-fast laser was adopted to drill holes in the gauge section of the tensile samples. However, the source of laser drilling adopted in this thesis was the nanosecond laser by the KJ Marketing Services company. Similar holes were drilled with comparable size (~35 μm in diameter). To arrange the holes in the gauge section, a center to center intervoid spacing of ~80 μm was kept constant for all samples. A vertical distance of about ~300 μm from the first and last hole to each edge of the sample was kept as a hole-free section in order to eliminate the artificial effect of the edge and have a better control of the failure process.

In order to study the shear effect of void coalescence, a misorientation angle θ was introduced by drilling a line of voids with θ = 0°, 15°, 30°, and 45°. Thus, different numbers of holes were accommodated in the central section of the sample as shown in Table 3.1. Before drilling, the samples were aligned straight in the laser machining stage, and the location of holes were calculated based on the origin (0, 0). The coordinates for hole centers were listed in Table 3.1. A brief close-up view of the hole configurations in the center of the sample (marked by dash square in Figure 3.2) were also shown in Figure 3.3.

Table 3.1: X and Y coordinates for different void arrangements.

Misorientation angle θ	0°		15°		30°		45°	
Total number of holes	6		6		7		8	
Coordinates	X	Y	X	Y	X	Y	X	Y
Hole #1	1550	2250	1556.8	2198.2	1542.2	2130	1552	2052
Hole #2	1630	2250	1634.1	2218.9	1611.5	2170	1608.6	2108.6
Hole #3	1710	2250	1711.4	2239.6	1680.7	2210	1665.2	2165.1
Hole #4	1790	2250	1788.6	2260.4	1750	2250	1721.7	2221.7
Hole #5	1870	2250	1865.9	2281.1	1819.3	2290	1778.3	2278.3
Hole #6	1950	2250	1943.2	2301.8	1888.6	2330	1834.9	2334.9
Hole #7					1957.9	2370	1891.4	2391.4
Hole #8							1948	2448

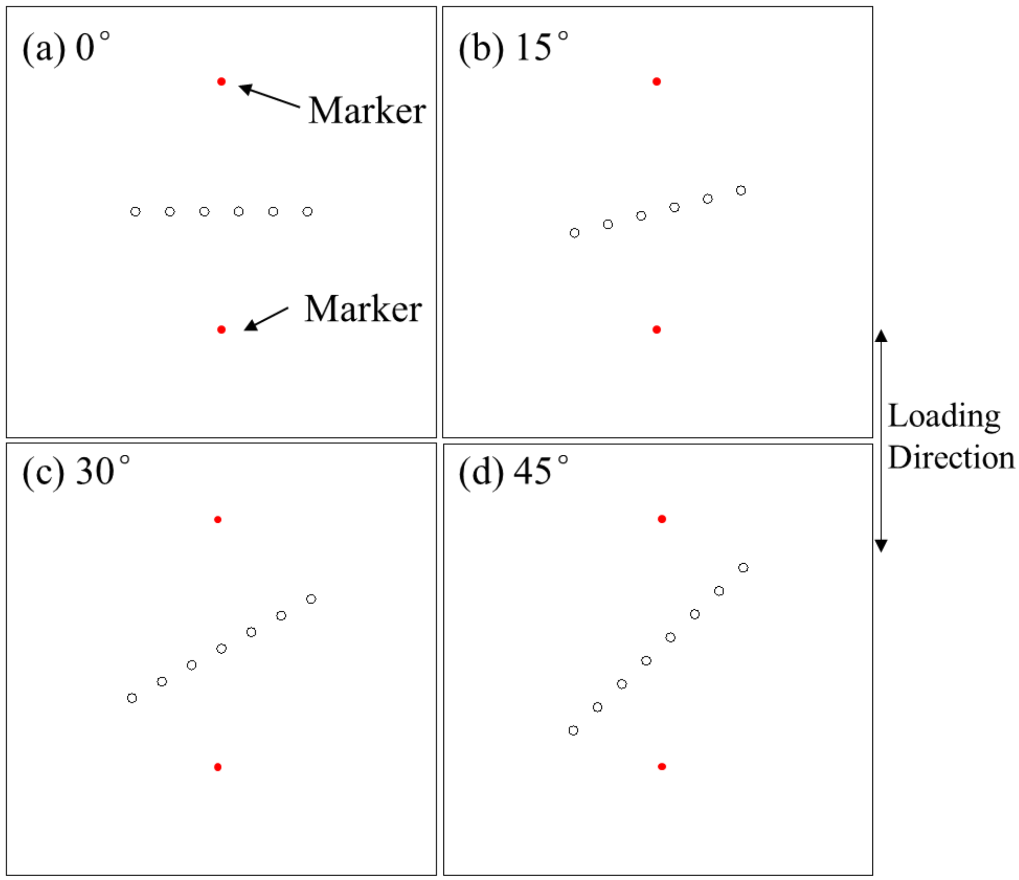

Figure 3.3: Schematic images of gauge center square with void arrangement for laser drilling with respect to the loading direction. Note that the holes are marked in order to see the location of each hole and the size are not in scale. The two points beyond the line of void represent the markers for far field calculation.

3.2.2 Surface refinement and heat treatment

The samples were ground with 4000 SiC paper for 1 minute with running water as the lubricant. Then the samples were polished using 0.05 μm colloidal silica suspension as the final step to produce a smooth surface. Finally, all samples were immersed in ethanol for an ultrasonic bath for 1 minute to remove the residues on the surfaces and debris stuck around the hole walls. For the metallographic examinations, the samples were electropolished after chemical polishing. The voltage was kept at 10V for 20 seconds and the D2 electrolyte was used as shown in Table 3.2.

Table 3.2: D2 electrolyte for electropolishing.

Chemicals	Phosphoric acid	Ethanol	Propan-1-ol	Water
%	25	25	5	45

The annealing procedure was conducted then to remove the damage produced by the laser drilling and the polishing process. The furnace was first heated up with argon atmosphere. The samples were then inserted into the furnace and soaked at the same temperature and cooled down in the furnace to room temperature. The detailed parameters of annealing for the studied materials were shown in Table 3.3.

Table 3.3: Annealing parameters of pure copper and α-brass samples

Materials	Pure copper	α-Brass
Temperature (°C)	400	400
Time (h)	1	2

3.3 Metallographic Examinations

After polishing, the samples were etched using the way described in Table 3.3. Optical examinations were conducted using Nikon Eclipse LV100 microscope following the standard techniques, and the microstructure was shown in Figure 3.4.

Table 3.3: Etching procedure of the studied samples.

Materials	Pure copper	α-Brass
Etchant	20 ml NH_4OH +2 ml 30% H_2O_2 +38 ml H_2O	20 ml NH_4OH +2 ml 30% H_2O_2 +38 ml H_2O
Time (min)	2	1

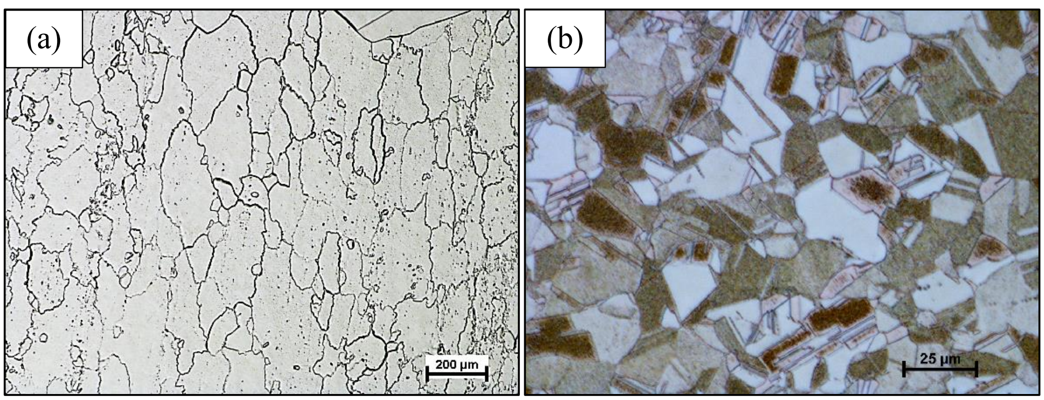

Figure 3.4: Optical micrographs of the (a) copper and (b) α-brass sample.

3.4 Fractography

The fracture surfaces were obtained after samples were pulled to fracture. Fractography measurements were conducted using JEOL 6610LV scanning electron microscope. The accelerating voltage was 10 kV and the working distance was kept to be 10 mm. Images were recorded for all the series of configurations in both of the pure copper and brass samples.

3.5 In situ Mechanical Testing – 2-D Analysis

Based on the methods proposed by Weck and Wilkinson (2008), tensile test coupled with electron microscopy was conducted using the Phillip 2020 Environment Scanning Electron Microscope (ESEM) to capture the void growth and linkage (Figure 3.5).

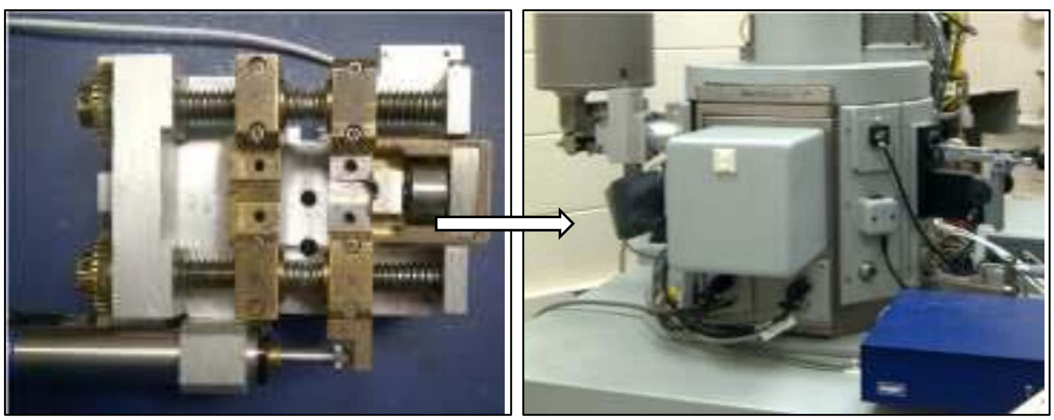

Figure 3.5: Loading cell in the ESEM.

During the in situ experiments, the samples were deformed in tension, and the test was stopped at various intervals, which allowed images to be taken. The load and displacement at each stop was recorded for analysis correspondingly. The crosshead speed was controlled to start from 20 μm/s, and the tests were slowed down to 5 μm/s when the load was seen to be saturated. The deformation was further slowed down to 1 μm/s in order to capture the coalescence point until the linkage of the whole ligament. A typical example of the interrupted load and displacement curve is shown in Figure 3.6. Limited number of images, typically over 10, were gathered and the coalescence strain would therefore be captured. From the images, quantitative measurements can be conducted from the extraction of the lateral and longitudinal lengths of the voids, the intervoid spacing, etc.

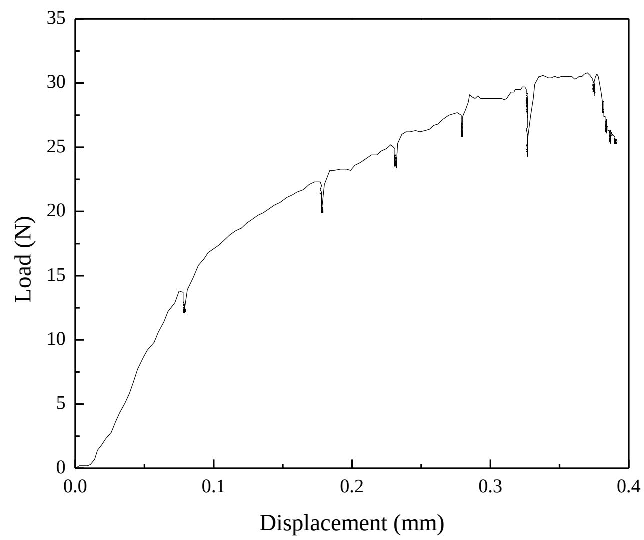

Figure 3.6: A typical interrupted load-displacement curve of a brass sample. The dips in the curve correspond to SEM image collections, where the loading was stopped, and the stress relaxation was observed.

In order to measure the lengths of the elongated gauge section at various testing increments, two markers with the same initial length l_0 = 460 μm were drawn as the initial gauge length before putting the sample into the chamber so that the spacing of the markers can accommodate the whole section of the void line. The far field true strain was then measured by keeping track of the distance between the markers ($\ln(l/l_0)$). The local true strain are determined based on the principal void diameters ($\ln(a/a_0)$ and $\ln(c/c_0)$). A free image analysis software ImageJ was used to measure all of the parameters from the SEM images. Since the contrast of the void and the material is high and the boundaries between voids and materials will appear to be bright and dark fringes, it is easy to define the interface of the voids and materials. The SEM images was taken to be with 1024 × 1024 pixels, 8 bit. When measuring, the image was zoomed in to the limit of the software (3200%) so that even the pixels on the boundaries can be easily detected. Thus, the measurement was conducted with the highest accuracy and the measurement error is down to 1 pixel. Therefore, the error bar according to the measurement accuracy will not be shown in the following discussions.

3.6 3-D X-ray Micro Tomography Testing

X-Ray tomography is a non-destructive technique allowing to perform three-dimensional observations of the damage in a material. The principle of the technique was shown in Figure 3.7. The source is an x-ray beam which will lose some of its intensity after interaction with the material. If the material contains particles, porous structures or even some phases having different x-ray absorption coefficients, this will result in an intensity contrast on the detector. By taking radiographs at various rotation angles and using proper reconstruction methods, the various phases of the material can be observed in three dimensions.

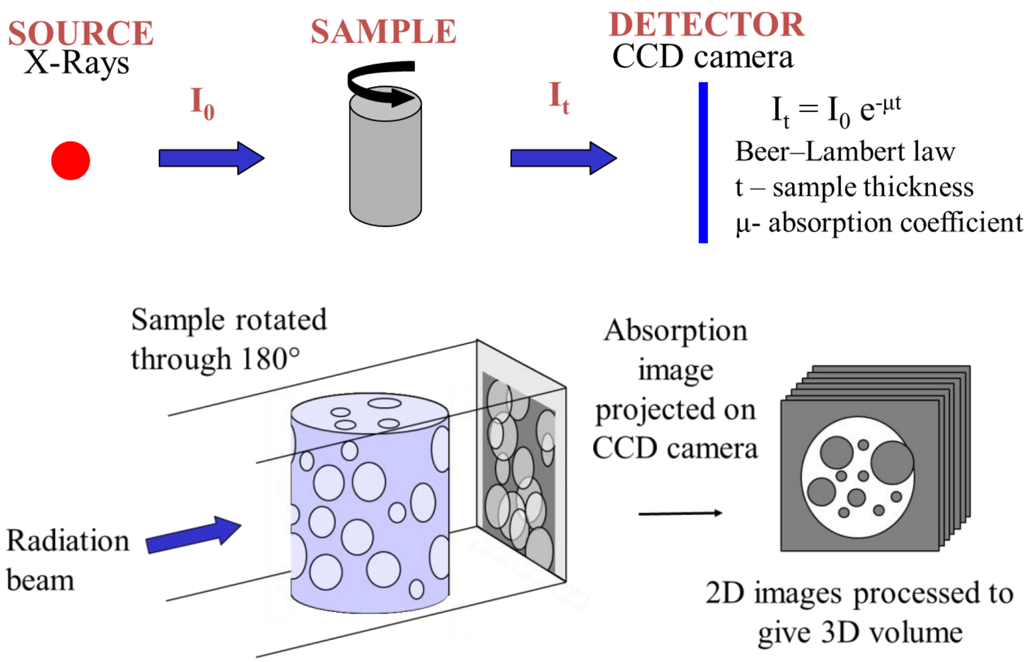

Figure 3.7: Brief drawing of the working principle of X-ray micro tomography.

Figure 3.8: SkyScan 1172 high-resolution micro-CT unit.

The X-ray micro tomography unit used in this work is the SkyScan 1172 lab based unit as shown in Figure 3.8. Compared with the beams produced by the synchrotron sources, the beams produced by this source are polychromatic and divergent. Longer exposure time is needed during the scanning process, and a series of adjustments have to be done during the reconstructing process to remove the beam hardening effect, ring effect and misalignment effect.

Unlike the work by Weck (2007) and Hosokawa (2011) using X-ray tomography coupled with in situ tensile testing, the tensile testing was conducted in the environment scanning electron microscope until the deformation was detected to localize in the ligament between the voids. The scanning was then performed to provide evidence of non-uniform growth of the voids in the line.

Because copper based materials have high X-ray absorption coefficients, a high voltage (typically over 90 keV) would be needed for the current samples to make a good scanning with high contrast. The scanning time is normally over 4 hours for the current materials. After that, the reconstruction process was conducted, and the 3-D model can be developed using the CTAn software.

Chapter 4

Results and Discussions

As described in Table 3.1, a line of voids were drilled at different orientations with respect to the tensile direction. The absolute intervoid spacing, i.e., the center to center spacing was kept constant. The longitudinal diameter $2a$, lateral diameter $2c$, edge to edge intervoid distance $2e$ and the pole to pole intervoid distance $2w$ were defined as shown in Figure 4.1. Note that in the initial state, the center to center intervoid spacing is the same as the pole to pole intervoid distance. However with increasing deformation, the shearing effect intervened, and the voids were subject to a shape change and small cracks form at the bellies of the voids. As a result, the shape of the void was never regular which made it difficult to define the void center. Also, the two poles are never aligned in the line with the center of the void. Accordingly, the dimensions were measured using the way addressed in Figure 4.1(c).

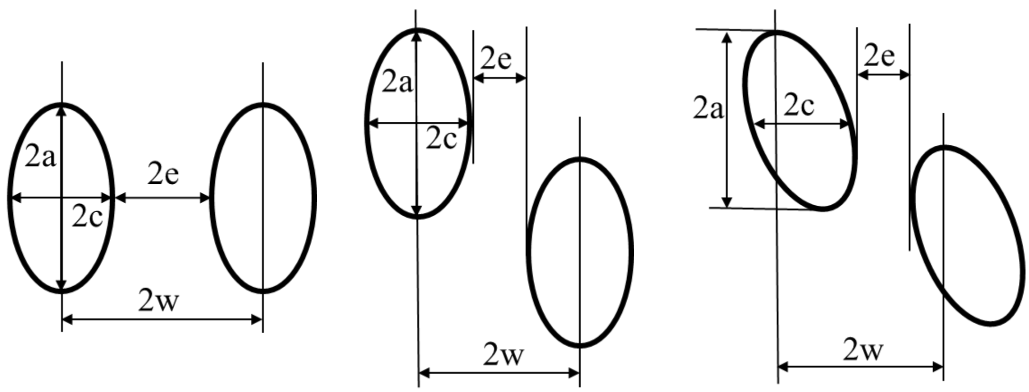

(a) (b) (c)

Figure 4.1: Schematic drawing of void dimensions depending on the void orientation with respect to the tensile axis (vertical in the picture). Note that only two voids were drawn to represent the whole line of voids. (a) A line of voids normal to the tensile axis, (b) a line of voids oriented at an arbitrary angle initially and (c) a line of voids underwent the shape change during deformation oriented at an arbitrary angle.

4.1 Void Growth and Coalescence in 2-D Pure Copper Model Materials

4.1.1 In situ SEM images

During the tensile deformation process, the test was stopped at different displacements to allow the capture of the SEM images. After the capture of the failure process of the whole line of voids, the first pair of voids to link was extracted and the growth, and coalescence behaviors were presented from Figure 4.2 to Figure 4.5.

With the proper alignment in the loading cell, the voids in the whole line grow uniformly from their circular shape to elliptical. Due to the constraining effect of the hole-free materials on both side of the void line, the voids at the two ends always grow more slowly than the ones in the middle. Therefore, the first pair of voids to link are always the ones in the middle region of the void line.

When the line of voids is oriented normal to the tensile direction, coalescence occurs by internal necking in the similar manner with the features reported by Weck and Wilkinson (2008) in AA 5052. The angle of the failure path also tilted with the increasing of misorientation angle θ from 0° to 45°. In the meantime, the coalescence mechanism turns into a shear localization process and the slip patterns are changed as the schematic drawings show in Figure 4.6 (a, b and c).

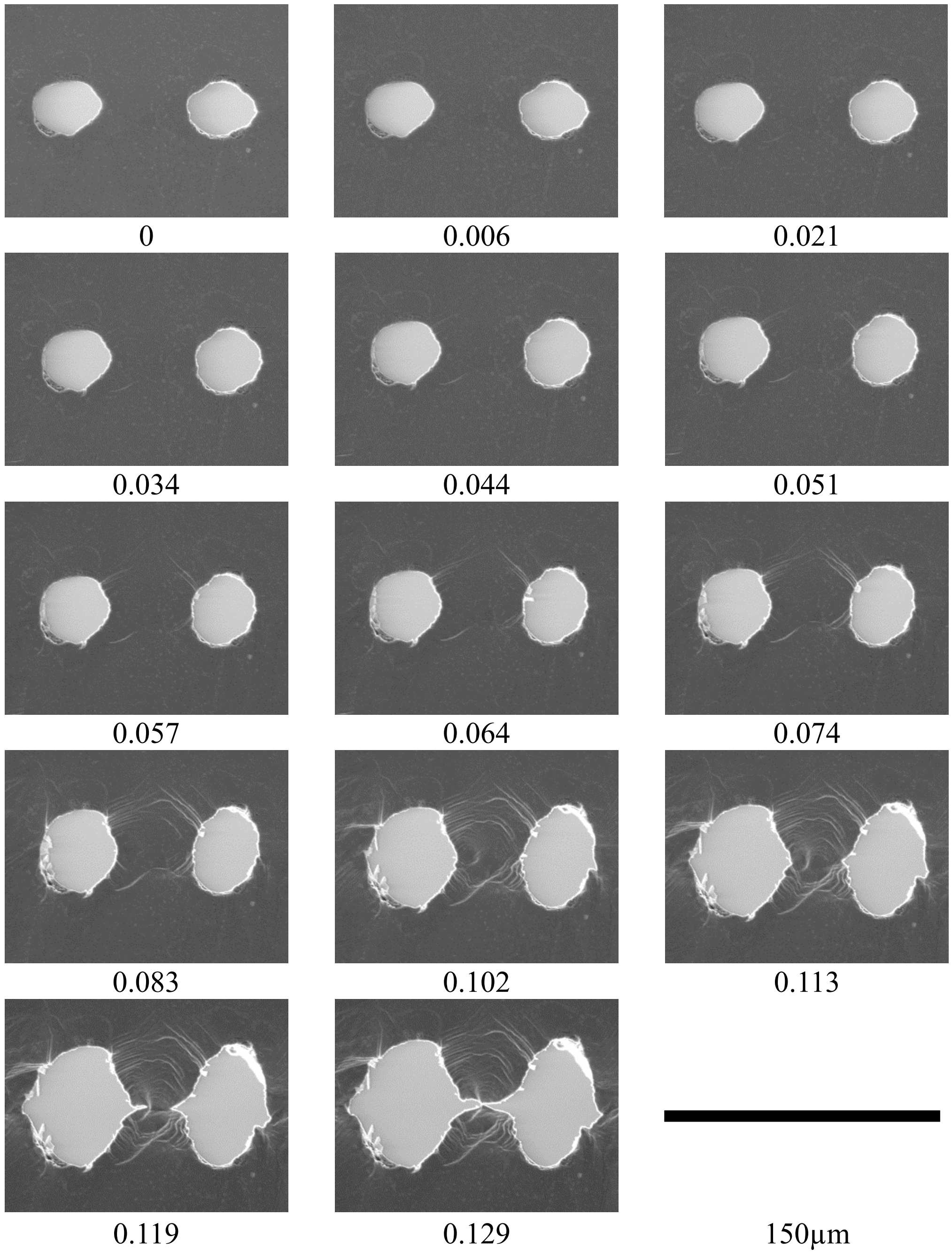

Figure 4.2: Deformation process of the first pair of voids to link of a pure copper sample containing 6 voids with the misorientation angle $\theta = 0°$ at different far field true strain increments shown below each image. The tensile direction is vertical.

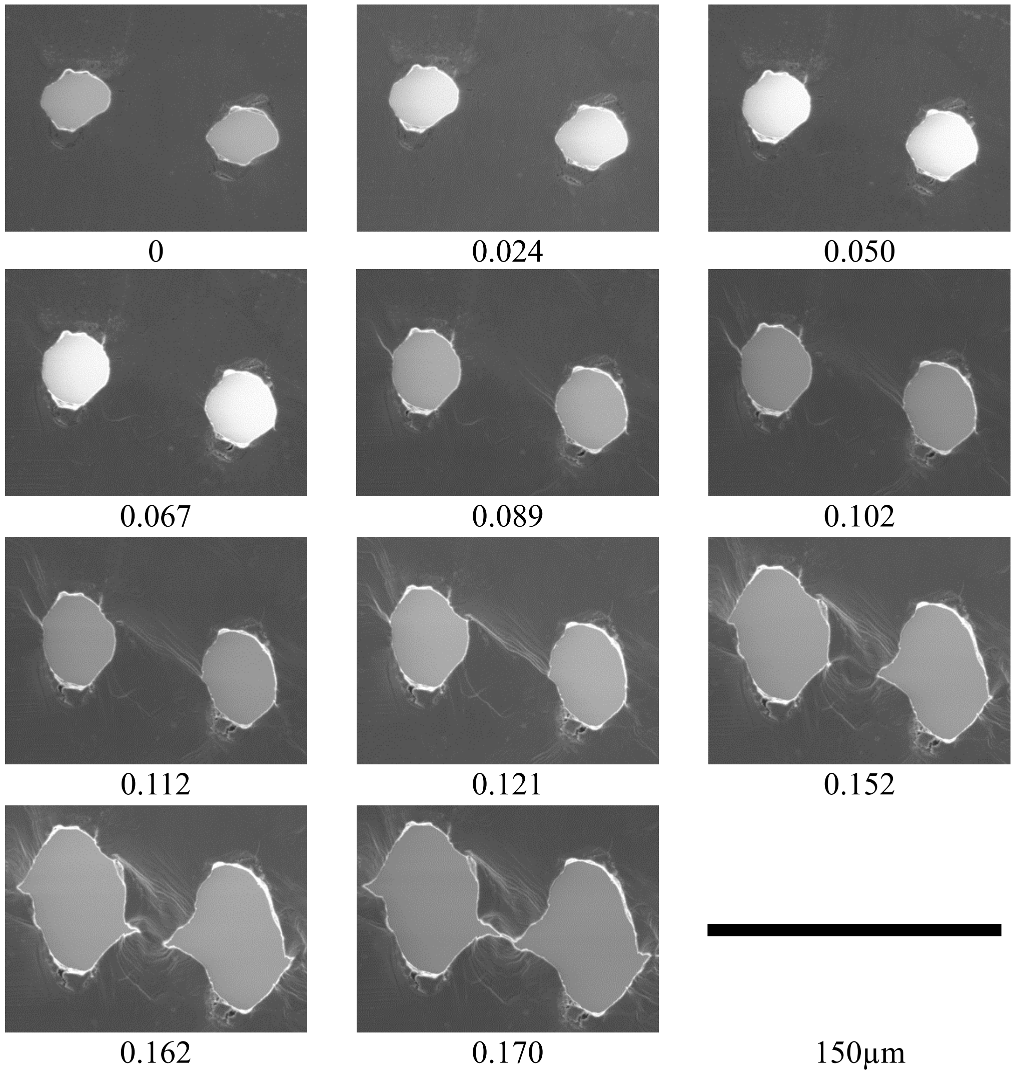

Figure 4.3: Deformation process of the first pair of voids to link of a pure copper sample containing 6 voids with the misorientation angle $\theta = 15°$ at different far field true strain increments shown below each image. The tensile direction is vertical.

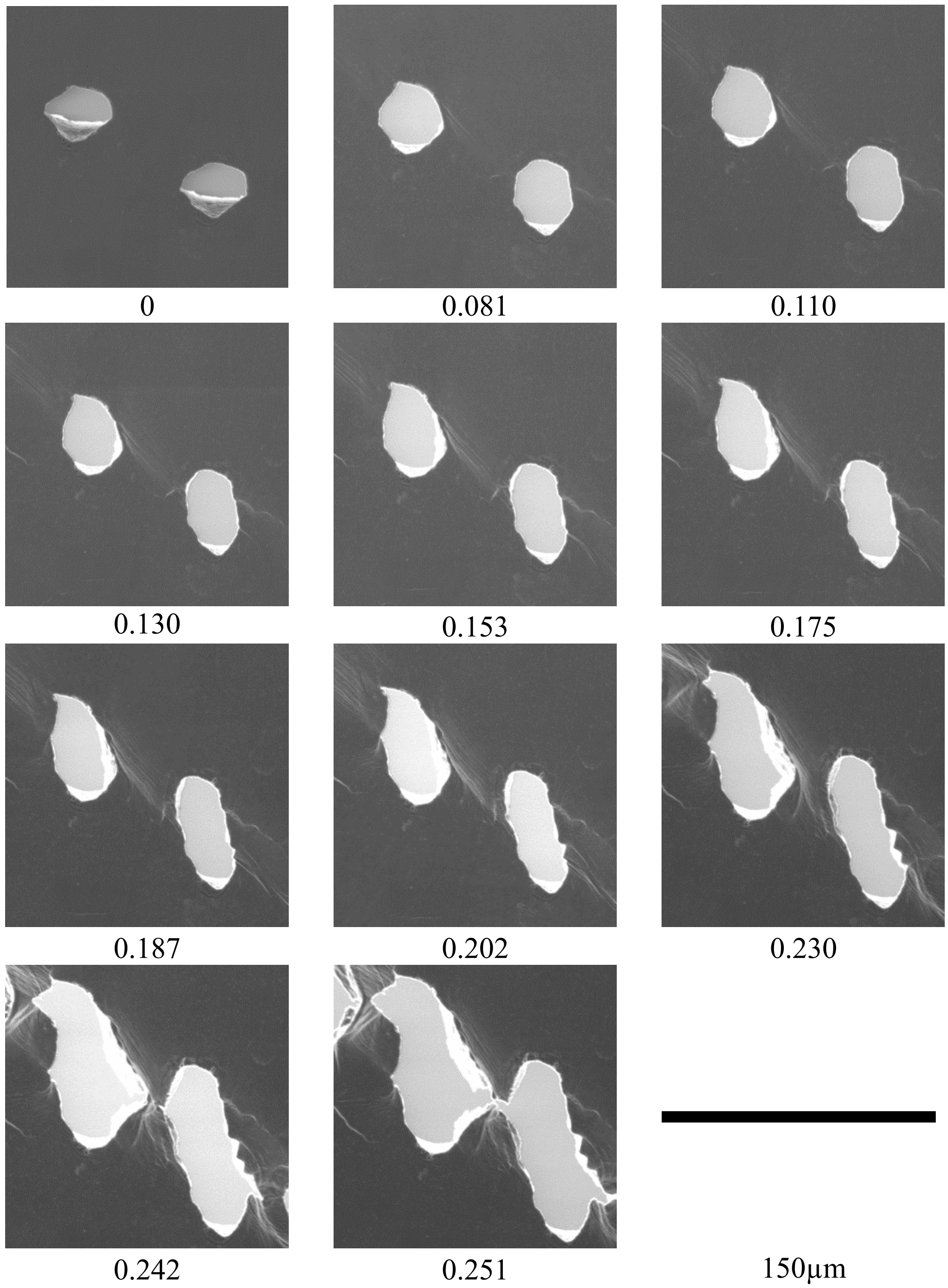

Figure 4.4: Deformation process of the first pair of voids to link of a pure copper sample containing 7 voids with the misorientation angle $\theta = 30°$ at different far field true strain increments shown below each image. The tensile direction is vertical.

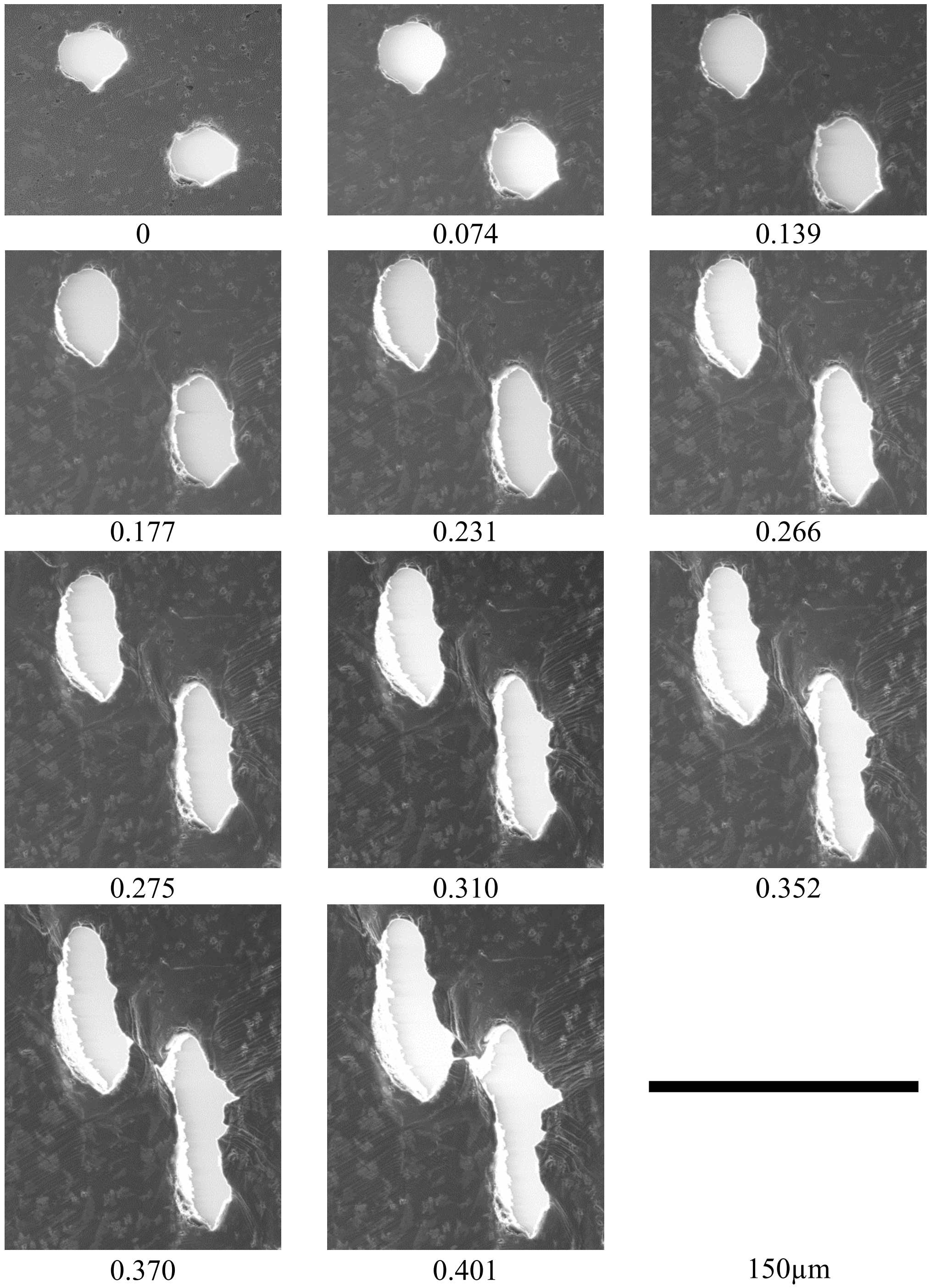

Figure 4.5: Deformation process of the first pair of voids to link of a pure copper sample containing 8 voids with the misorientation angle $\theta = 45°$ at different far field true strain increments shown below each image. The tensile direction is vertical.

Based on the Thomason criterion (1990) for plane strain and plane stress, the plane stress condition can be satisfied when the thickness h is less than five times of the hole spacing 2*e*. Given the geometry of the 0° and 15° samples, the stress state of the current experiments is plane stress. This is further confirmed by the existence of slip lines on all of the samples. Since the initial center to center intervoid distance is kept constant and the orientation angle is changed, the 2*e* value for 30° and 45° samples are designed to be reduced. Therefore, the stress state for these samples is turned from plane stress to plane strain. Attention has to be paid here to specify the stress state for each sample. Since the thickness from the sample to sample is not the same due to the polishing process, nor is the void spacing and the regularity of the holes in the initial state. Even in the same sample, the thickness through a different part of void ligaments is still not uniform. As a result, the stress state during deformation in the current 2-D experiments is complex, neither pure plane stress nor plane strain, and the stress state discussed in this work should therefore be regarded as an approximation.

Another feature of the slip lines is that they are formed with a diamond shape for the 0° case, not the cross lines proposed by Brown and Embury (1973). During further deformation, the amount of the slip lines increases until the deformation is further localized to cause the formation of cracks. With the decreasing of the orientation angle, the diamond shape slip lines are transformed as shown in Figure 4.6 (b). When voids are oriented at 45°, the slip lines at 45° can be drawn directly from one void to the other. What's more, since the first pair of voids to coalesce is never the ones at the end of the line, there is no constraining effect for either void like the two voids case of Weck and Wilkinson (2008). Therefore, the shearing process can go through the whole part of the ligament. Supports for this can be found in the fractography images of brass samples where the shear inducing elongated dimples are distributed on the whole parts of the ligaments. Another phenomenon detected is that the voids rotated during deformation for 15°, 30°, and 45° specimens. This is not shown in Figure 4.6 and will be discussed in Section 4.34.

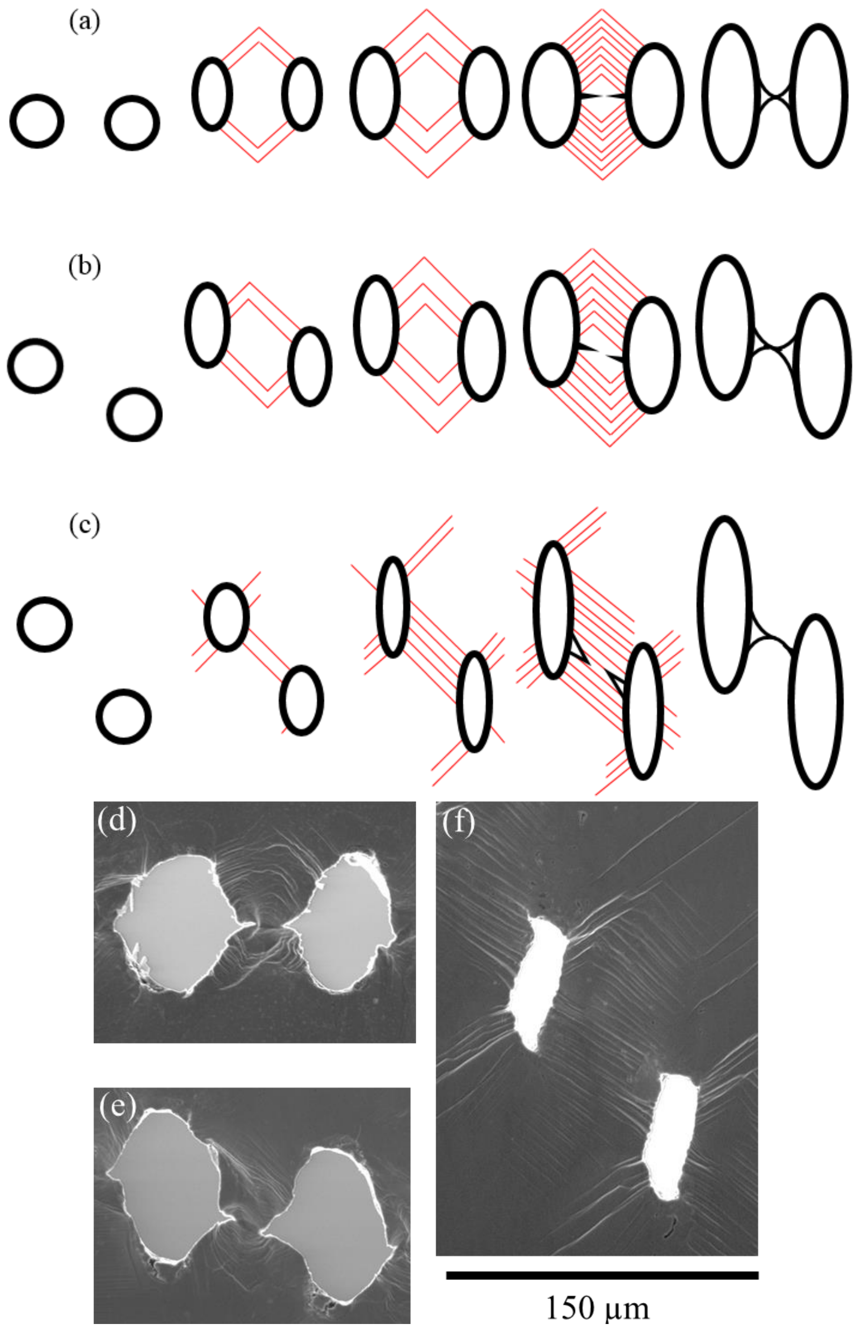

Figure 4.6: Schematic drawings of the deformation pattern of the pure copper samples containing voids with the misorientation angle θ = (a) 0°, (b) 15° and (c) 45° with respect to the tensile direction (vertical in the image). Slip features of a corresponding pair of voids were shown in (d), (e), and (f) as the experiment support, respectively.

4.1.2 Fracture surfaces

Because of the high purity of the copper samples, there are no voids detected on the hole-free thin sheet material and the thin sheet necks down to a line to form the fracture surfaces. The slip lines are also clearly seen in Figure 4.7(a). With the laser holes drilling through the sample, the ligament between the linked holes also necks down to a thin ridge (Figure 4.7(b)) indicating the high ductility of the copper sample. Due to the shearing effect, the ridges are not straight and subjected to a bending though thickness. Moreover, there is no secondary void population detected in the close-up image (Figure 4.7(c)).

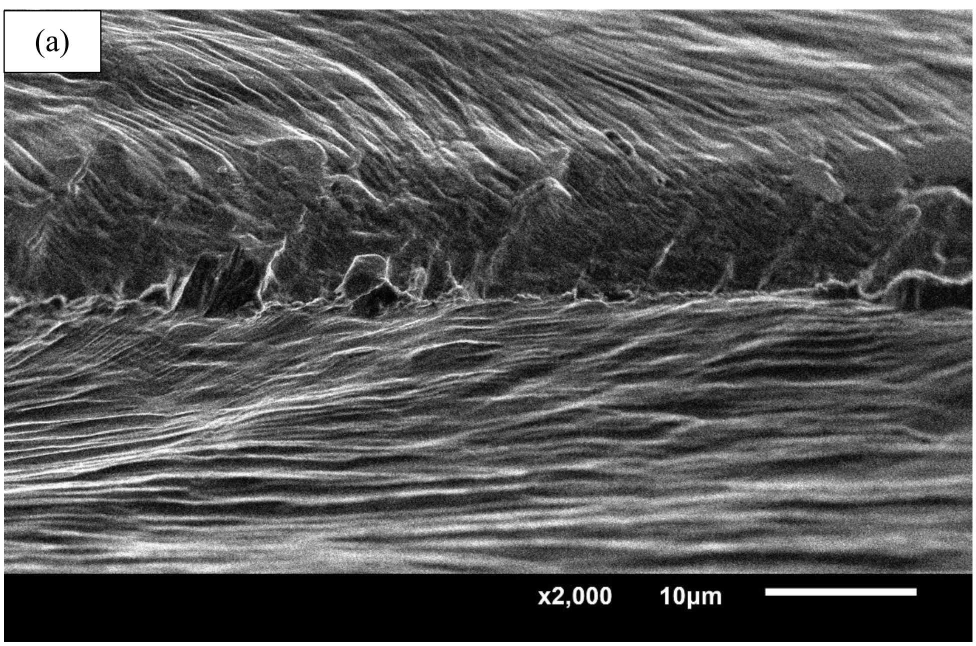

Figure 4.7: Fractograph of (a) a hole-free pure copper foil sample and (b) the pure copper sample containing a line of voids with misorientation angle θ = 45°. The close-up of the ligament ridge of the 45° is shown in (c). The black arrows indicate the ligaments between the voids.

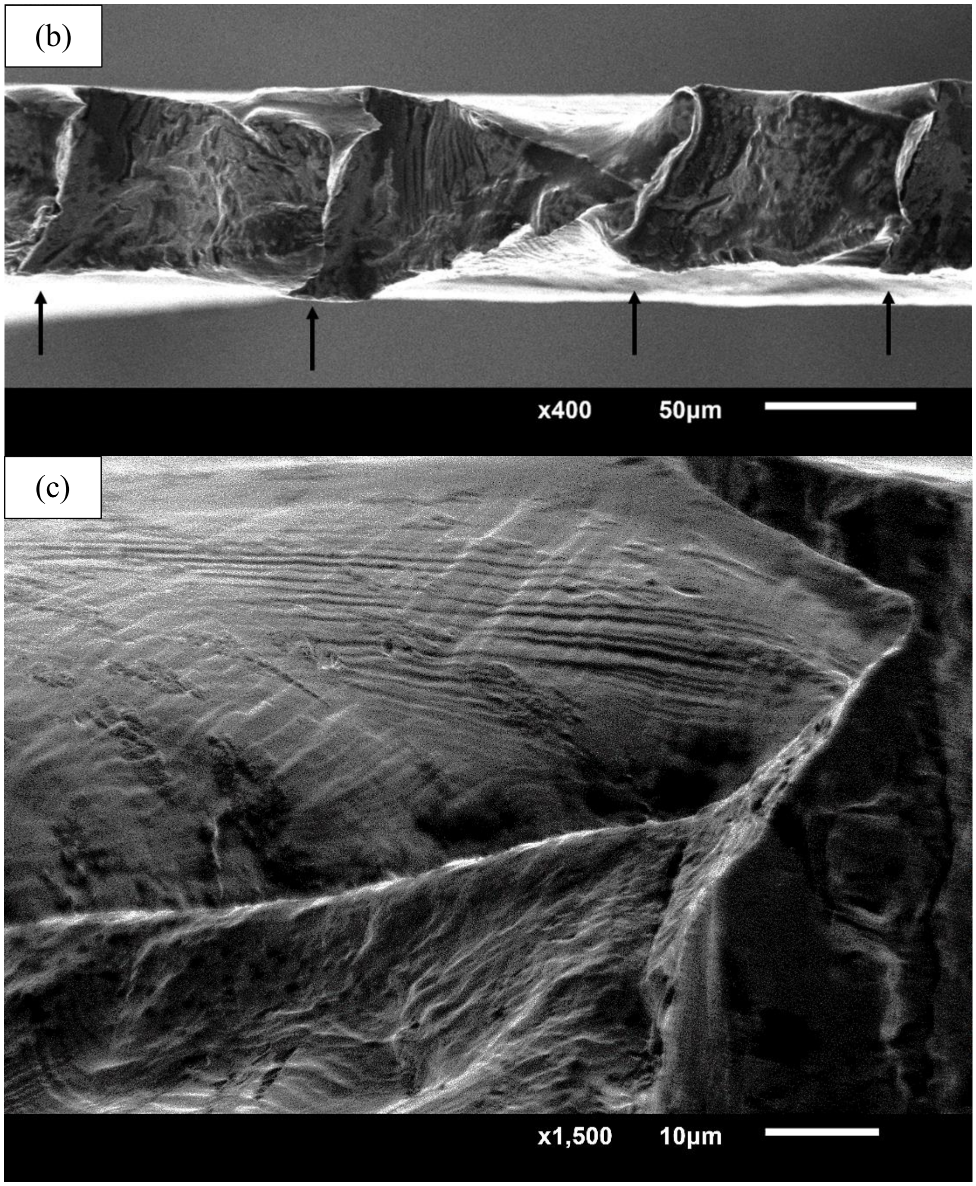

Figure 4.7: Continued.

4.2 Void Growth and Coalescence in 2-D α-brass Model Materials

4.2.1 In situ SEM images

Using the same method as described above, the deformation sequences of brass samples were captured as shown from Figure 4.8 to Figure 4.11. The features of void growth showed no significant difference from pure copper samples. For all the samples tested in the current work (pure copper and brass), the failure of the materials were all induced by the coalescence and linkage of the voids as an example shown in Figure 4.12.

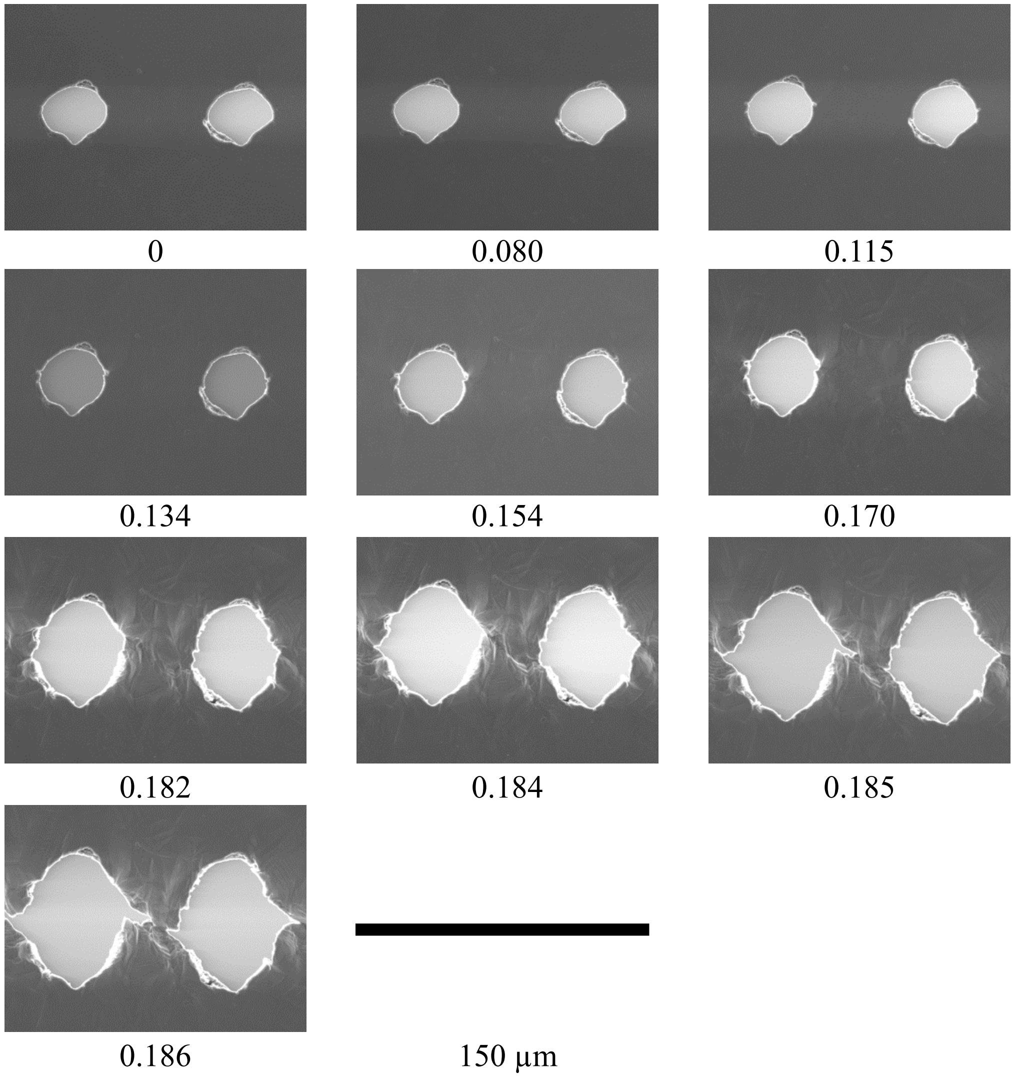

Figure 4.8: Deformation process of the first pair of voids to link of a α-brass sample containing 6 voids with the misorientation angle θ = 0° at different far field true strain increments shown below each image. The tensile direction is vertical.

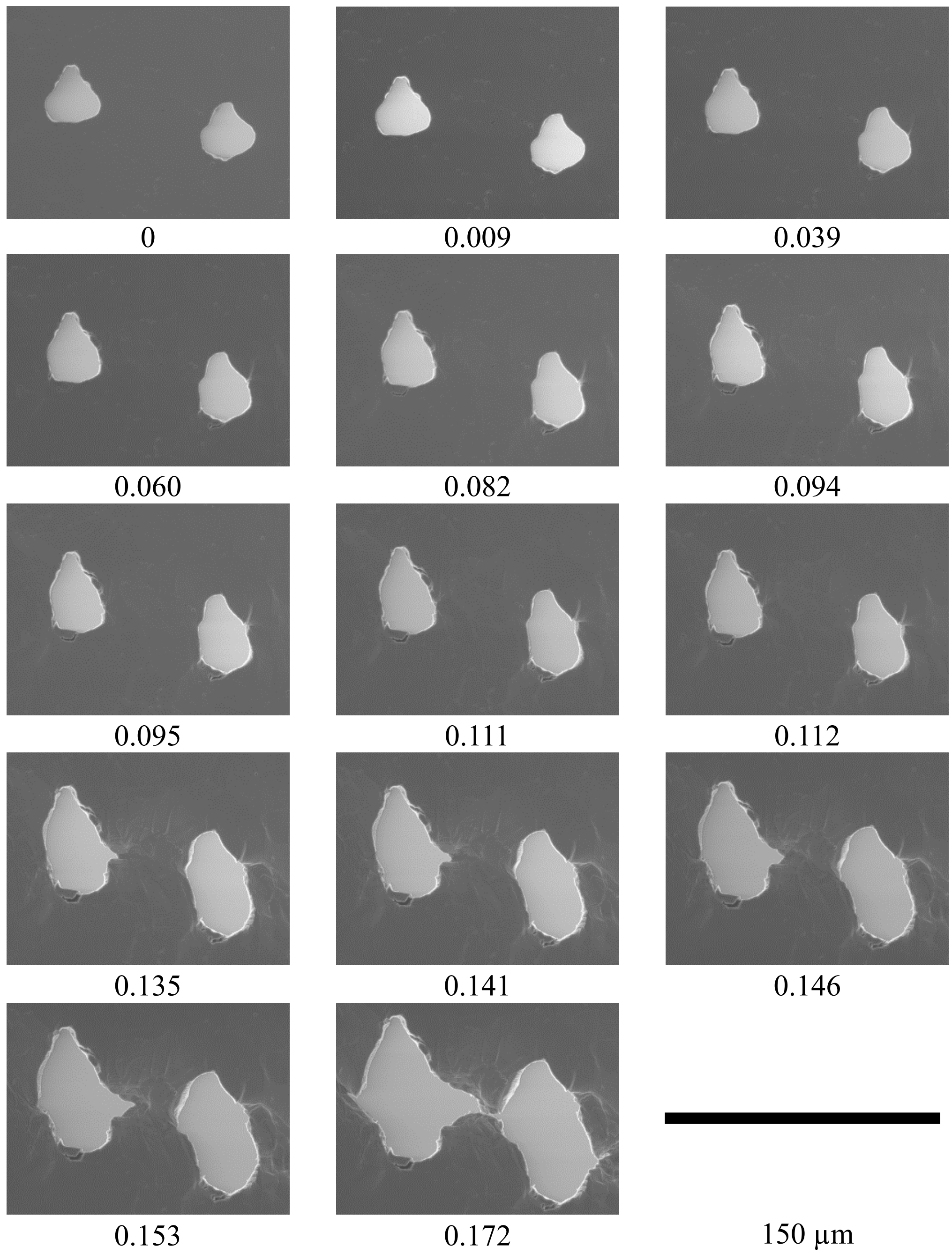

Figure 4.9: Deformation process of the first pair of voids to link of a α-brass sample containing 6 voids with the misorientation angle $\theta = 15°$ at different far field true strain increments shown below each image. The tensile direction is vertical.

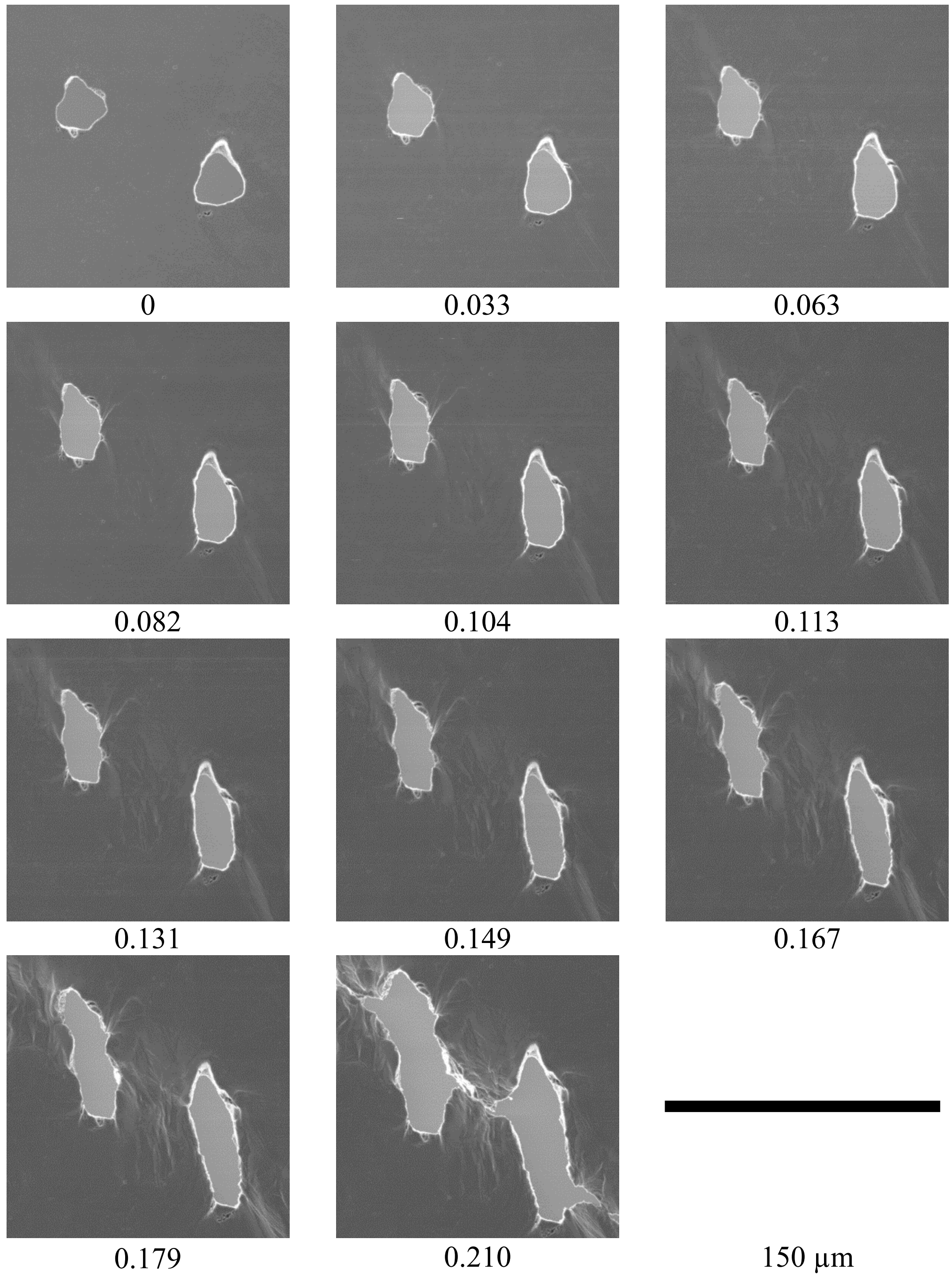

Figure 4.10: Deformation process of the first pair of voids to link of a α-brass sample containing 7 voids with the misorientation angle $\theta = 30°$ at different far field true strain increments shown below each image. The tensile direction is vertical.

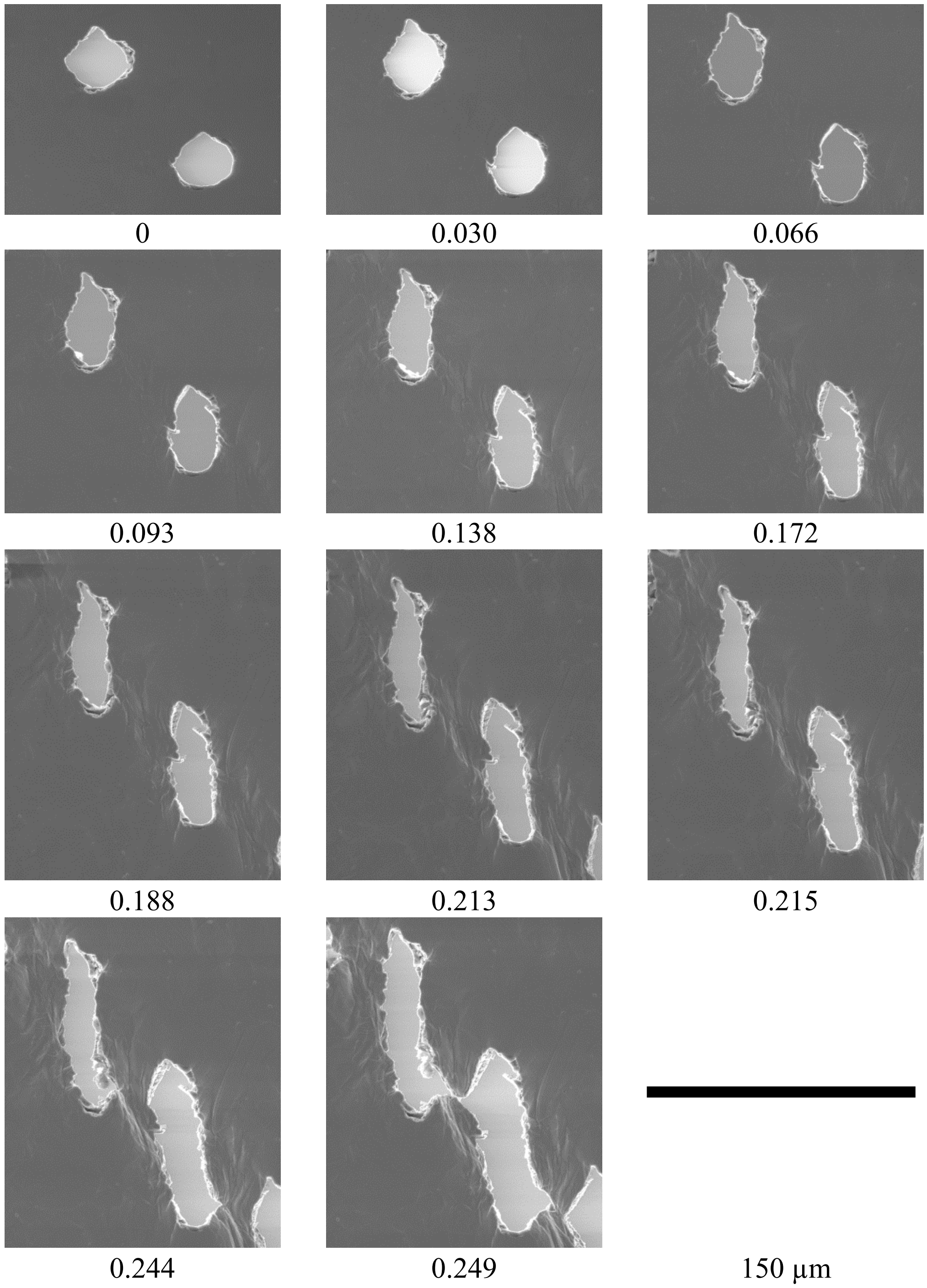

Figure 4.11: Deformation process of the first pair of voids to link of a α-brass sample containing 8 voids with the misorientation angle $\theta = 45°$ at different far field true strain increments shown below each image. The tensile direction is vertical.

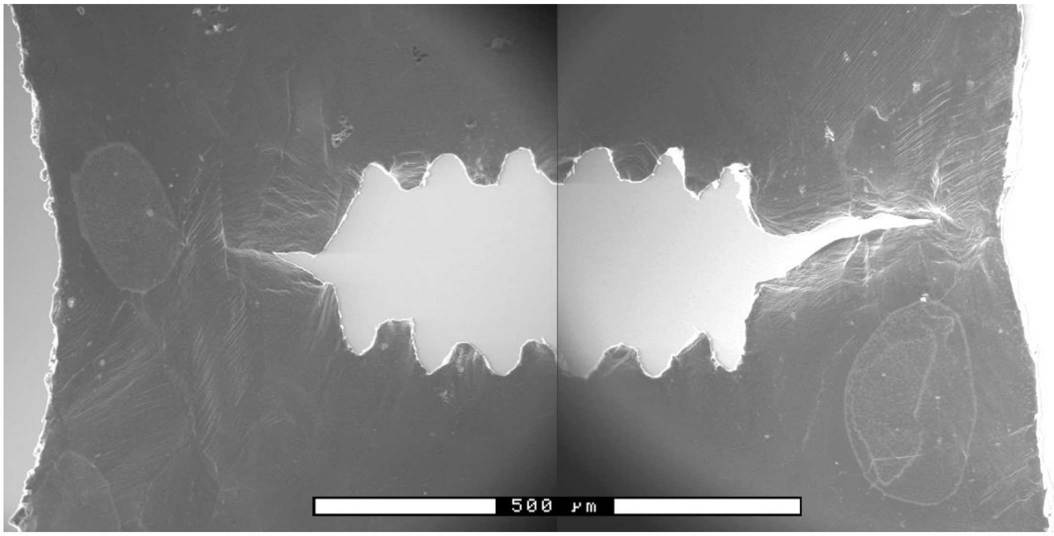

Figure 4.12: SEM image of an α-brass sample containing the void line with the misorientation angle $\theta = 0°$ right prior to the failure of the entire section. The tensile direction is vertical in the picture.

4.2.2 Fracture surfaces

The hole-free α-brass sheet material also necks down to a line, but the ridge is not as sharp as that in the pure copper samples (Figure 4.13(a)). At regions near the ridge, a large amount of deep dimples were detected as the close-up image shown in Figure 4.13(b). The features in the samples with laser holes showed similar features (Figure 4.14), and again the ligament narrows down but not to a sharp ridge as found in pure copper samples. The existing of elongated dimples on the ligament region indicates the shear localization and void sheeting occurred during the deformation.

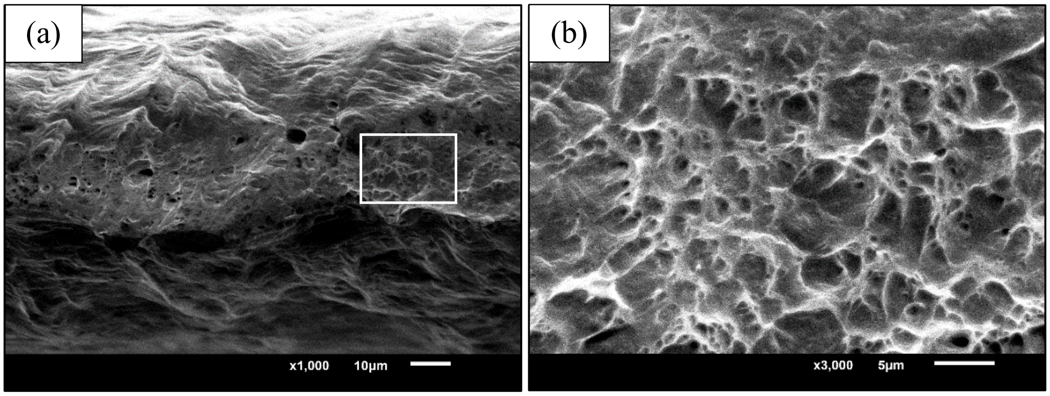

Figure 4.13: Fractograph of (a) hole-free α-brass sheet sample and (b) close-up image above the ridge of the fracture.

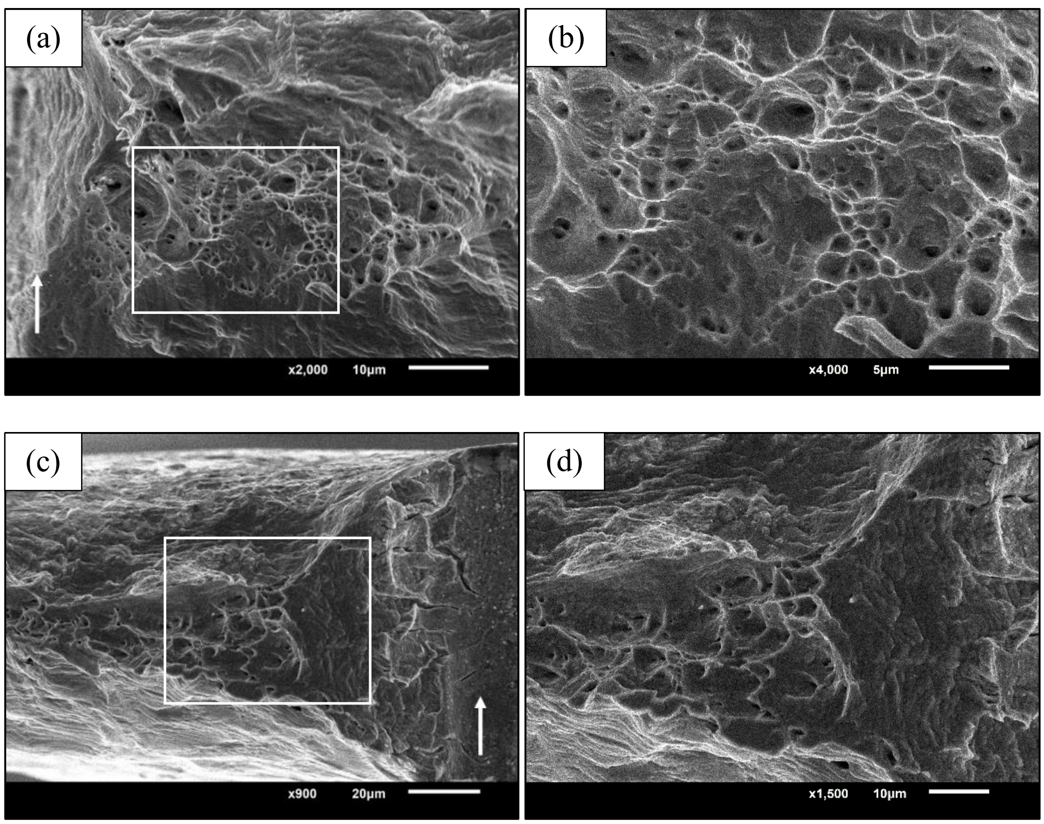

Figure 4.14: Fractograph of the α-brass sample containing a line of voids with the misorientation angle θ = (a) 0° and (c) 45°. The tensile direction is vertical in the picture. The arrows indicate the position of the voids. The close-up images are also shown in (b) and (d) respectively.

4.3 Analysis of 2-D Results

The quantitative analysis of the 2-D single line samples was conducted by measuring the parameters from the SEM images taken in the in situ tensile tests. The longitudinal diameter $2a$, the lateral diameter $2c$, the edge to edge intervoid distance $2e$ (ligament length), the center to center intervoid distance $2w$, and the pole to pole intervoid distance were measured accordingly and the initial dimensions are a_0, c_0, e_0, and w_0, respectively.

4.3.1 Definition of coalescence and intervoid distance

Weck et al. (2008) used a simple way to measure the intervoid distance by defining it as the edge to edge distance ($2e$) in the similar 2-D single sheet model materials. This distance would keep decreasing during the deformation process and reach zero when two voids linked together. In their work, the coalescence was defined as the intervoid ligament failure. However, following the terminology established in the numerical study by Koplik and Needleman (1998) and following work by Benzerga (2002), it has been proved possible by Hosokawa (2013a, c) to capture the onset of coalescence when the intervoid distance stops shrinking. In comparison with the three definitions of intervoid distances, i.e., centroid to centroid distance, surface to surface, and pole to pole distance as shown in Figure 4.15. Hosokawa et al. (2013a, c) pointed out that an effective way to measure the distance was by measuring the pole to pole distance, which would stop decreasing at the onset of coalescence. It is expected that, at that moment, the voids stop shrinking in the lateral direction and start expanding towards their neighbors in uniaxial tension. Thus, the coalescence definition proposed by Weck et al. (2008) was too simplistic, and the strain recorded was actually that at the linkage point which was larger than the real coalescence strain.

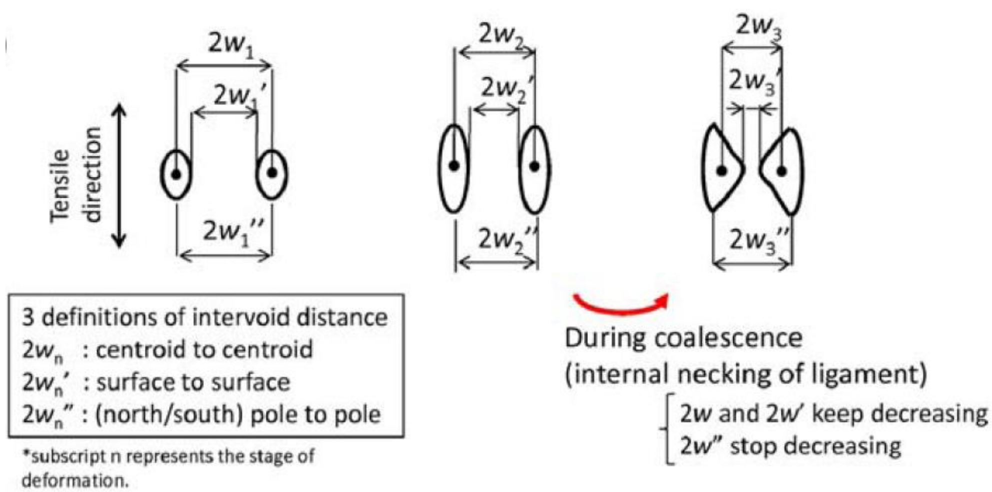

Figure 4.15: Three different definitions of intervoid distance by Hosokawa et al. (2013a, c).

However, the method proposed by Hosokawa et al. (2013a, c) is based on the vertical distance between two poles. It has not been discussed for the cases when the line of voids is aligned with an arbitrary orientation angle. In order to verify whether this method can be applied to the current situation, different intervoid distances were plotted as a function of far field strain in the following discussions and the definition used in this work is to be verified.

4.3.2 Major diameter

Figure 4.16(a) shows the relationship between the local true strain concerning about the longitudinal growth of the voids defined as $\ln(a/a_0)$ and the far field true strain. In the 2-D condition, since the reduction of cross sectional area cannot be measured, the far field strain was then defined as the elongation of a fixed initial length of two markers on the sample surface as $\ln(l/l_0)$. Note that the data were collected over small strain increments during the tensile test in order not to miss the coalescence and linkage event, and only selected data points were shown in the figures of the following sections. From Figure 4.16, one can see that the slope of void growth curve is decreasing with increasing the misorientation angle θ, meaning that to reach the same local strain, the whole gauge of material needs to extend longer for the 45° sample than the 0° sample. This is reasonable because of the following reasons. When the material containing a line of voids is pulled in uniaxial tension, the voids act as the stress concentrator and the deformation is localized in the void region. The localized void regions are elongated more than the hole-free material region which contribute more in the calculation of far field true strain. Compared with the voids normal to the tensile axis, the misoriented voids occupy a longer region in the longitudinal direction in the gauge. Therefore, it is reasonable to see a larger far field strain at the same level of local expansion. The similar behavior is confirmed by the growth curve of brass sample in Figure 4.15 (b). One can also see an enhancement of the final linkage strain not only in terms of the far field strain, but also the local strain. This will be discussed later in section 4.3.5.

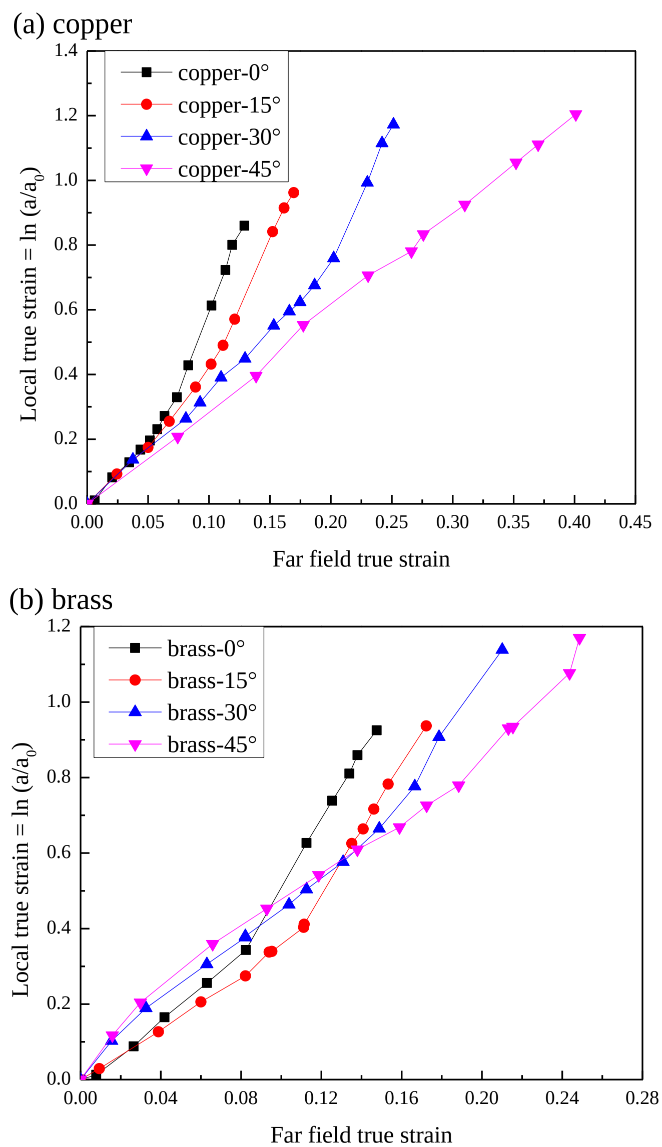

Figure 4.16: Local strain on the longitudinal dimension $\ln(a/a_0)$ plotted as a function of the far field strain for (a) pure copper and (b) α-brass samples containing a line of voids with the misorientation angle θ = (a) 0° and (c) 45°. The tensile direction is vertical in the picture.

4.3.3 Minor diameter

By taking SEM images over small strain increments, the coalescence events were carefully captured. The shrinkage of lateral diameter was well visualized for the first time in the 2-D thin sheet model materials. From Figure 4.18, when the void line is normal to the tensile direction, the lateral shrinkage is not significant. Similar behavior is confirmed in the experiments in AA 5052 by Weck and Wilkinson (2008). With increasing the misorientation angle, the shrinkage behavior become conspicuous. For some samples tested, the voids even closed up at a point in the pure copper 45° samples due to the strong shearing effect as shown in Figure 4.17. Even to some extent, this event is related to the irregular shape of the initial void, this phenomenon, however, is still non-negligible and has been detected for several times.

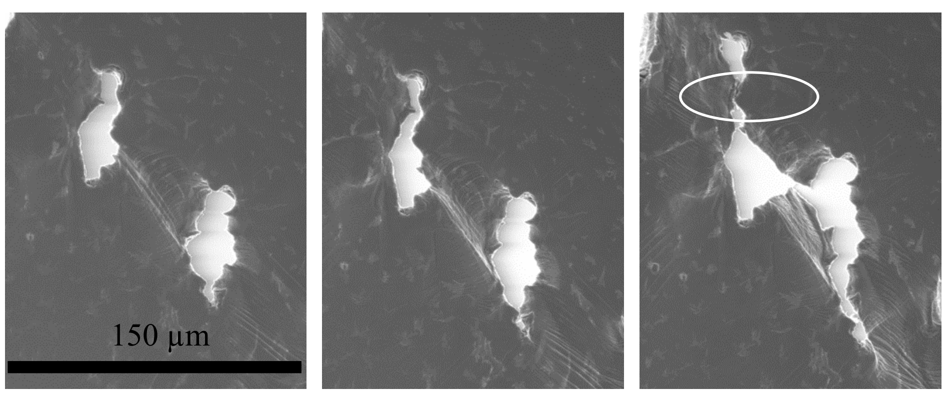

Figure 4.17: SEM images of selected deformation sequences in a pure copper with the misorientation angle $\theta = 45°$ showing the void closure.

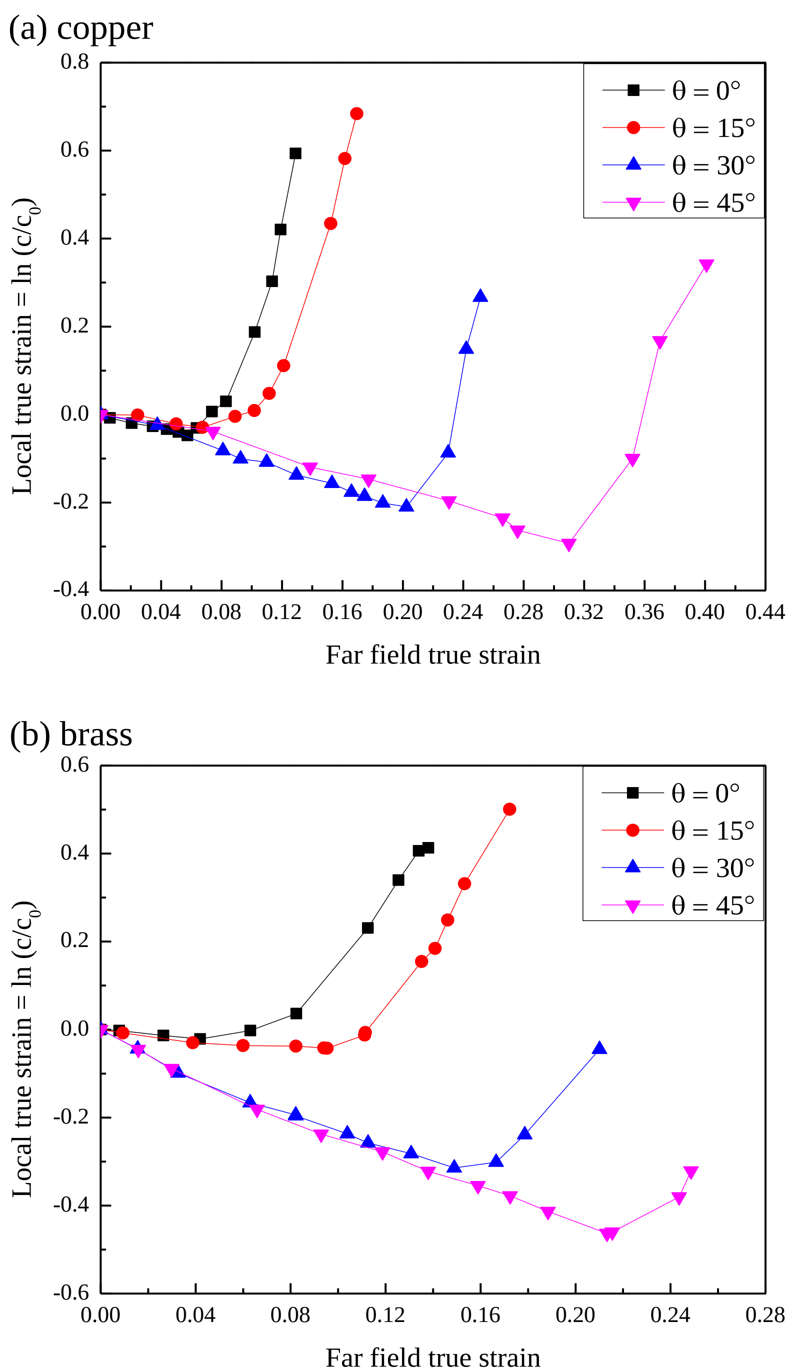

Figure 4.18: Local strain on the lateral dimension $\ln(c/c_0)$ plotted as a function of the far field strain for (a) pure copper and (b) α-brass samples containing a line of voids with the misorientation angle $\theta = 0°$, 15°, 30°, and 45°.

The initial void is spheroidal despite the fact that the drilling is not perfect enough to produce ideal circular shape. With deformation, the major and minor diameter were changed as described above and the voids became elliptical and lost its spheroidicity. Scheyvaerts et al. (2011) investigated the variation of the ratio between the two radii of one void using FE unit cell modelling. Their results showed that the variation is independent of the initial void shape (oblate or prolate) under low triaxiality conditions and plane strain except for the order for voids to coalesce. The normalized value of the minor/major diameter ratio for the first pair of voids to coalesce was plotted in Figure 4.19. The evolution of c/a is consistent with the modeling results being almost independent of the misorientation angle except that coalescence starts later with larger misorientation.

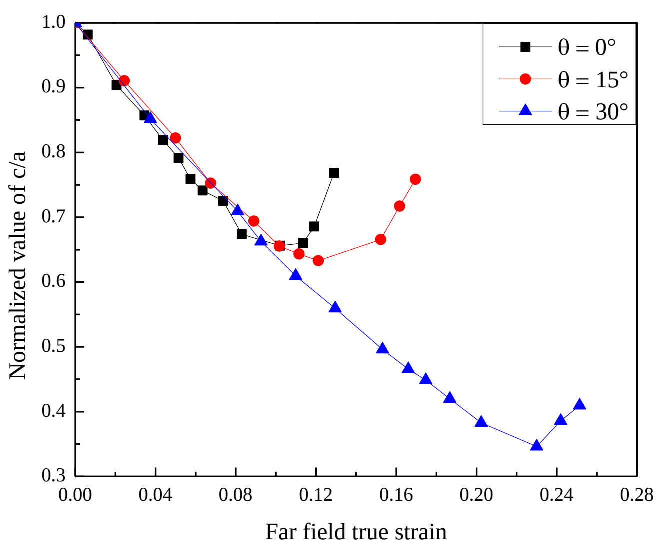

Figure 4.19: Normalized value of the void dimension c/a plotted as a function of far field true strain for pure copper samples containing a line of voids with the misorientation angle $\theta = 0°$, 15°, and 30°.

4.3.4 Ligament length and void rotation

The ligament length (also known as the edge to edge intervoid distance, $2e$) was normalized to plot as a function of far field true strain as shown in Figure 4.20. The edge to edge intervoid distance was believed never to stop decreasing during deformation (Hosokawa et al. (2013a, c)) and thus could give no evidence of void coalescence. This was also proved by Weck and Wilkinson (2008) in the AA 5052 2-D experiments and the current samples containing void line normal to the tensile axis. However, for the sample with $\theta = 30°$, we observed an increase in the edge to edge intervoid distance. For voids with $\theta = 45°$, this trend was enhanced. This might result from the rotation of the materials due to the formation of shear band during the localized necking.

Looking back to the SEM images, at the early stage of deformation, the voids also experienced a rotation process together with the shape change prior to the coalescence event. This is also the reason for the mismatch of the pole to pole distance with the center to center distance for the 30° and 45° arrangements. The void rotation within the shear band during deformation has been well studied in the unit cell simulations (Gologanu et al. (1997), Paisalam and Ponte Castañeda (1998), Butcher and Chen (2009), Scheyvaerts et al. (2011), Rahman et al. (2012)). Surprisingly, there is no systematic study to visualize this process experimentally.

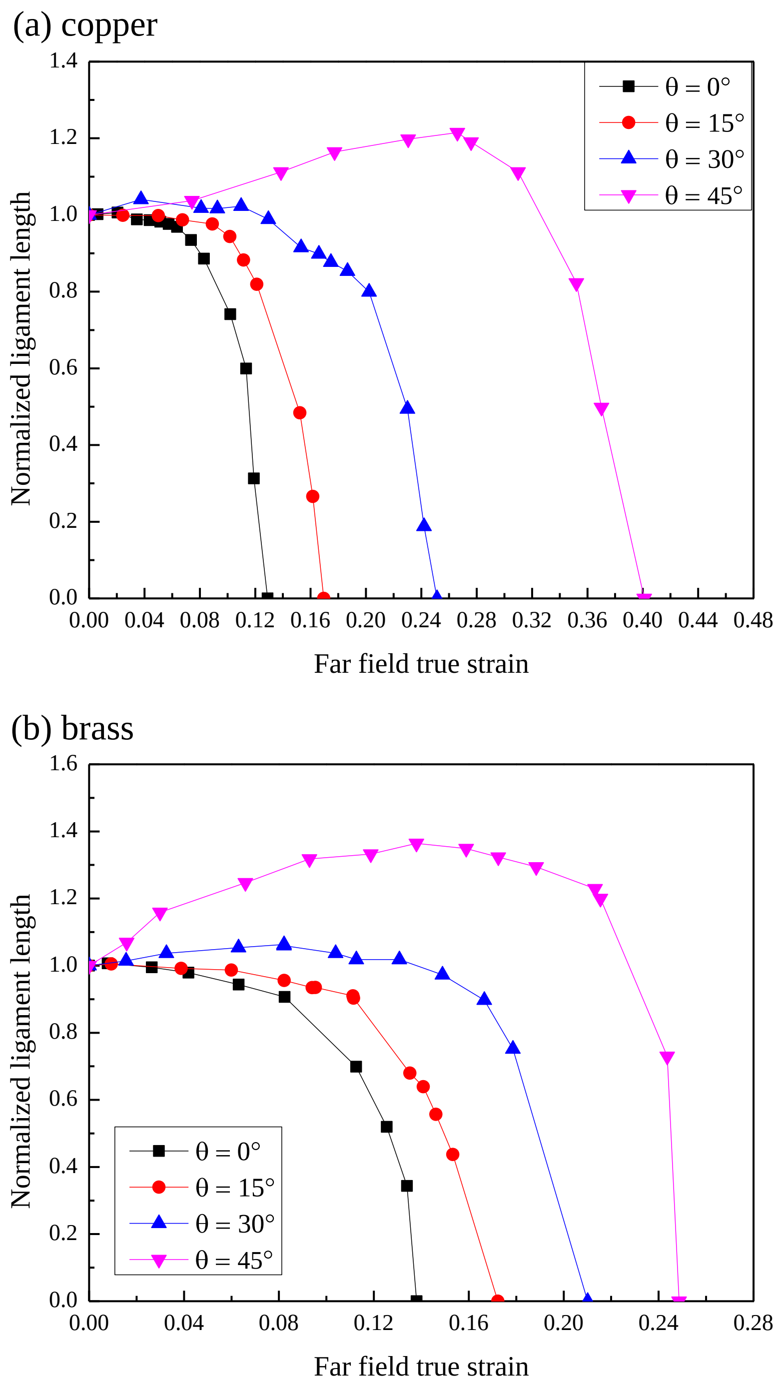

Figure 4.20: Normalized length of the ligament between the voids (edge to edge intervoid distance) plotted as a function of far field true strain for (a) pure copper and (b) α-brass samples containing a line of voids with the misorientation angle θ = 0°, 15°, 30°, and 45°.

The void rotation is a quite important phenomenon in the shear localization process. However, most modelling works are based on the condition of simple shear loading on a unit cell. The rotation behavior for a line of voids under uniaxial tensile loading is still not clear. Moreover, even when the rotation has been captured by some experimental or modelling work, it was still ignored (Bandstra et al. (1998), Ma et al. (2012)). The rotation of a line of voids under uniaxial tensile loading has never been studied comprehensively, and understanding of the rotation effect is still limited to the modelling results. Therefore, a quantitative analysis was conducted to visualize the void rotation during deformation for both pure copper and brass samples as shown in Figure 4.21.

The rotation angle was determined by measuring the angle between the poles of the void and the vertical tensile axis. As shown in Figure 4.21, for the copper and brass samples with voids normal to the tensile direction, the rotation angle fluctuates indicating that the voids do not rotate significantly due to the uniaxial loading condition. For samples with misorientation angle θ, the voids are rotated towards the shearing angle during the deformation process. This phenomenon can also be seen in Figure 4.2 to Figure 4.5 and Figure 4.8 to Figure 4.11. It has been proved that the rotation of the voids can give rise to the loss of ductility which decreases their spacing and brings them into a configuration favorable for coalescence (Tvergaard (2008), Scheyvaerts et al. (2011)). Figure 4.21 shows the rotation angle reaches the peak at the coalescence point and then decreases with the further deformation. There is a tendency for both of copper and brass samples that with the orientation closer to the 45° shear angle, the maximum rotation angle increases. One exception is the copper 45° sample. There is a strong interference between the voids at the right hand side and the artifacts on the edge of the sample. This strong interaction also produces a crack on the right side of that void and then offsets the localization effect to cause the void rotation.

One important difference between this work and the modelling is that, the modelling results are mostly dealing with a unit cell under loading conditions dominated by shearing, where the hydrostatic tension is zero or even negative ((Barsoum and Faleskog (2007a, b), Scheyvaerts (2008), Leblond and Mottet (2008), Nahshon and Hutchinson (2008), Tvergaard (2008, 2009), Xue et al. (2010), Jodlowski (2009), Tvergaard and Nielsen (2010), Barsoum and Faleskog (2007), Nielsen and Tvergaard (2011), Scheyvaerts et al. (2011), et al.) Therefore, the contribution of the matrix material rotation on the rotation of the voids cannot be neglected as studied by Scheyvaerts et al. (2011). As a comparison, the current loading condition is uniaxial tension. With misorientating the void lines, the shear band is forced to initiate and localize in the void ligament. The texture effect is not clear, and the contribution of the rotation of the matrix material is still not clear under the current situation.

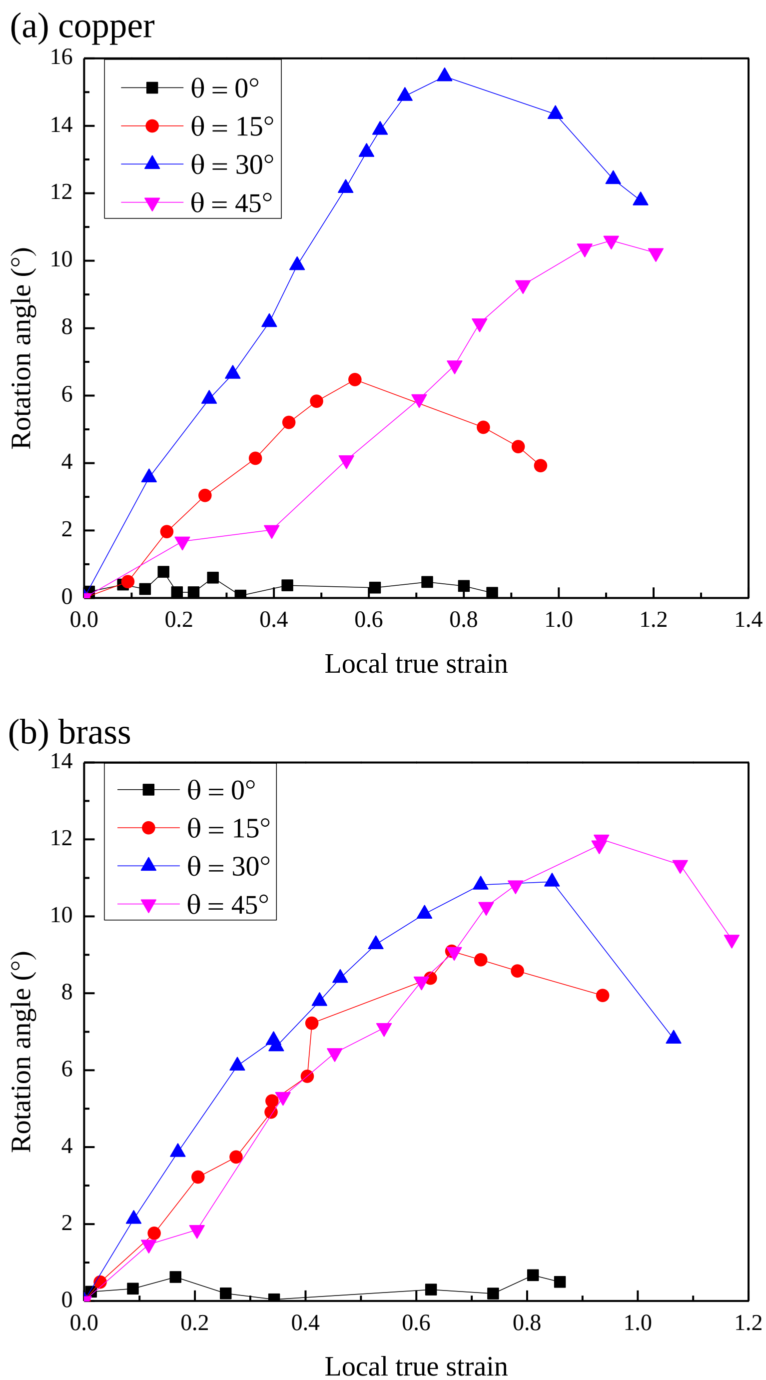

Figure 4.21: Rotation angle plotted as a function of local true strain for (a) pure copper and (b) α-brass samples containing a line of voids with the misorientation angle $\theta = 0°$, 15°, 30°, and 45°.

4.3.5 Effect of the misorientation angle

As the results shown in section 4.3.2 and 4.3.3, the void line with larger misorientation angle incorporates a longer region of the gauge section and contributes more on the calculation of far field true strain. It results in not only the decreasing slope of void growth curve, but also the delaying of void coalescence in terms of the far field strain for both copper and brass as shown in Figure 4.22(a).

However, there is also an increase in the local true strain in terms of major void diameter expansion and minor void diameter shrinkage at the onset of coalescence and final linkage for larger misorientating (Figure 4.22(b)). One thing to be emphasized is that the initial configuration was designed to contain voids with the same center to center distance. Thus, the pole to pole distance is initially shorter with increasing the misorientation angle. Weck and Wilkinson (2008) reported that decreasing the spacing of two voids normal to the tensile direction would lower the final linkage strain. Moreover, the coalescence event should be accelerated due to the shear localization effect (Cox and Low (1974)), Hosokawa (2013a)). However, in the current study, coalescence was found to be postponed with a misorientation angle to introduce the shearing effect which seems to be contradictory with the previous theory.

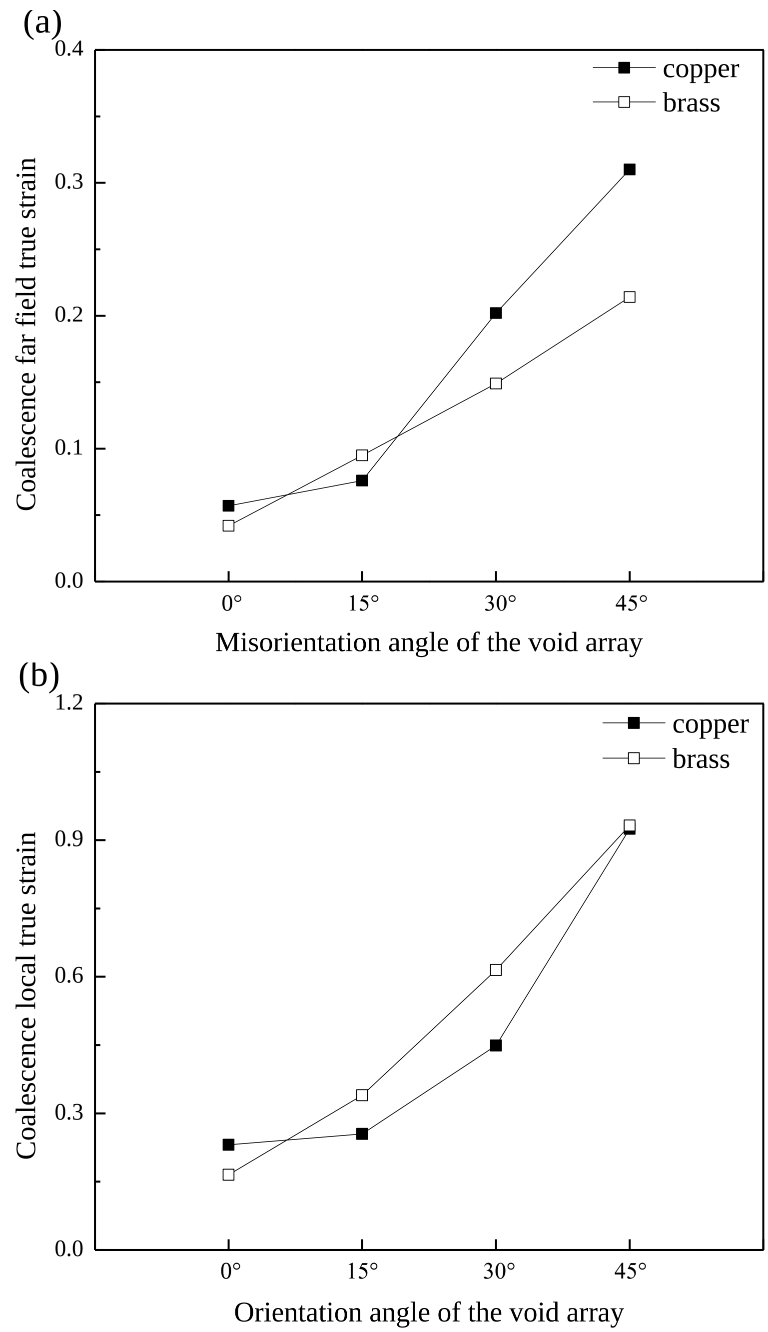

Figure 4.22: (a) Far field and (b) local true strain at coalescence plotting as a function of orientation angle of the void line with respect to the tensile axis for the pure copper and brass samples.

One possible reason for this is that the voids in the current experiment are closely arranged (void diameter = (33 ± 5) µm, center to center distance = (83 ± 5) µm, edge to edge distance = (50 ± 5) µm). The initial intervoid distance is only larger than the void size by a factor of 1.5 which is comparable to one of the cases studied by Weck and Wilkinson (2008) with two voids (void diameter = 10 µm, center to center distance = 25 µm, edge to edge distance = 10 µm). It has been widely assumed that a larger and faster strain concentration will occur at the belly of the intervoid ligament. The strain localization is favored in the case with closely located voids. The interaction of the strain fields by the neighboring voids will be smaller with the increasing in misorientation angle θ.

Another important thing to notice is the volume fraction (in this specific case referring to the area fraction) of the initial voids at the local region as shown in Figure 4.23. Experimentally, it is challenging to separate the effect of local volume fraction and shear localization. In this work, a line of voids with the same size was put in the specimens regardless of orientations. Therefore, the local volume fraction of voids in the section perpendicular to the loading direction varies with orientations. The area fraction were calculated by extracting the contour of the voids using image J. The initial area fraction for the pure copper samples are 17.5%, 4.3%, 2.4%, and 2.0%, respectively. Note that the calculation area fraction of voids in a line were only conducted to contain the area of the first voids to coalesce and not to contain more materials for the symmetry consideration. There have been extensive experimental studies showing the relationship between the volume fraction and the coalescence strain. The coalescence strain is sensitive with increasing the volume fraction. As the results show in this work, the effect of local volume fraction plays a much greater role than the shear localization.

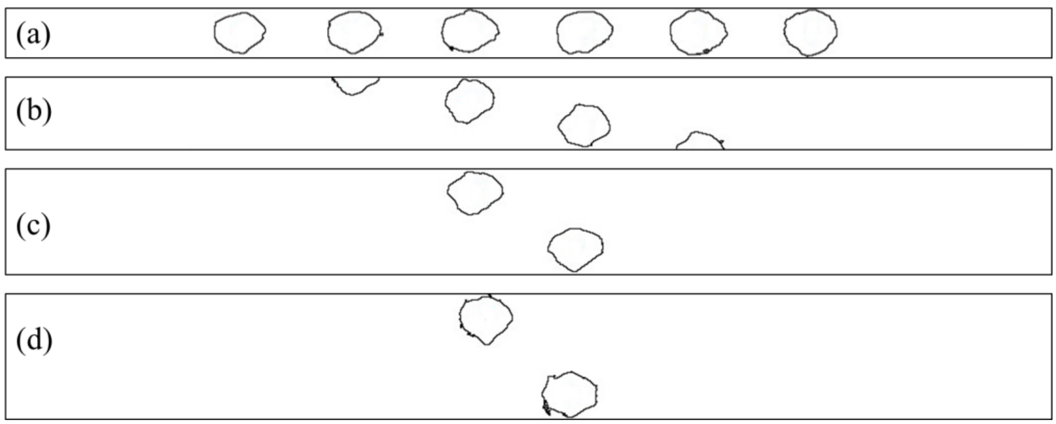

Figure 4.23: Outlines of the first pair of voids to coalesce extracted from the SEM images in the pure copper samples with the misorientation angle θ = (a) 0°, (b) 15°, (c) 30°, and (d) 45°.

4.3.6 Effect of the work hardening behavior

Comparing the pure copper and brass samples, one can see that there is no significant difference of the void growth behaviors. However, the brass samples exhibit larger coalescence local strain compared to the pure copper samples except for the 0° samples. The exception is believed to be due to the irregularity of the initial voids leading to experimental artifacts. Similar results have been confirmed by Hosokawa (2013b) on the 3-D copper and brass model materials. It is believed that a higher work hardening exponent can suppress the void coalescence event in both 2-D and 3-D range.

4.3.7 Comparison with the classic models

4.3.7.1 Rice and Tracey model

The equation used here to fit the Rice and Tracey void growth model is the integrated form as described in Equation (2.16) and (2.17). Similar with the methodology used by Weck and Wilkinson (2008), the stress triaxiality was assumed to be constant and equal to 0.33 because the diffuse necking during the deformation process is not significant and can be neglected in the shin sheet 2-D model materials cases. The local true strain, that is, the change in longitudinal and lateral diameters, was plotted as a function of the far field strain.

$$\varepsilon = \ln\left(\frac{A_0}{A}\right) \tag{4.1}$$

$$\varepsilon = \ln\left(\frac{l}{l_0}\right) \tag{4.2}$$

To determine the far field true strain, Weck et al. (2008) and Hosokawa et al. (2013a, b, and c) directly measured the cross section area from the tomograms during deformation in their 3-D visualization software and the far field true strain is then given by Equation 4.1. In the current 2-D experiments, the cross section area cannot be measured directly during the in situ tensile test and the only way is by using the elongation of the gauge. Hence, two markers with l_0 = 460 μm apart was drawn before deformation on all the samples which can accommodate the whole range of the voids. Then the far field true strain can be obtained by keeping track of those markers and measuring the distances between them from the SEM images taken in low magnification. The local true strain is determined by the elongation of longitudinal (2*a*) and lateral diameter (2*c*) of the voids.

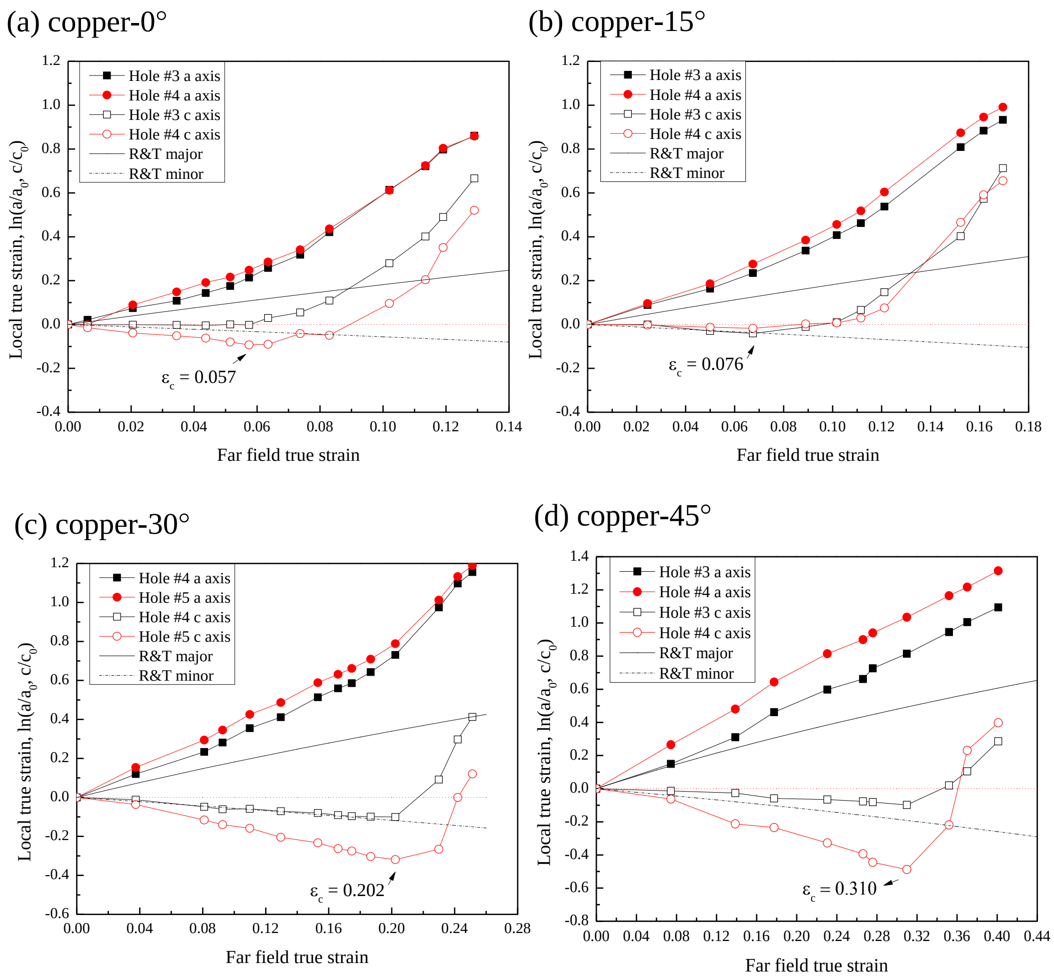

Figure 4.24: The local true strain of the first pair of voids to link plotted as a function of the far filed true strain showing the void growth and coalescence behaviors until linkage for **pure copper** samples containing a line of voids with the misorientation angle θ = (a) 0°, (b) 15°, (c) 30°, and (d) 45°. The Rice and Tracey void growth model was also plotted as a comparison with the experimental results.

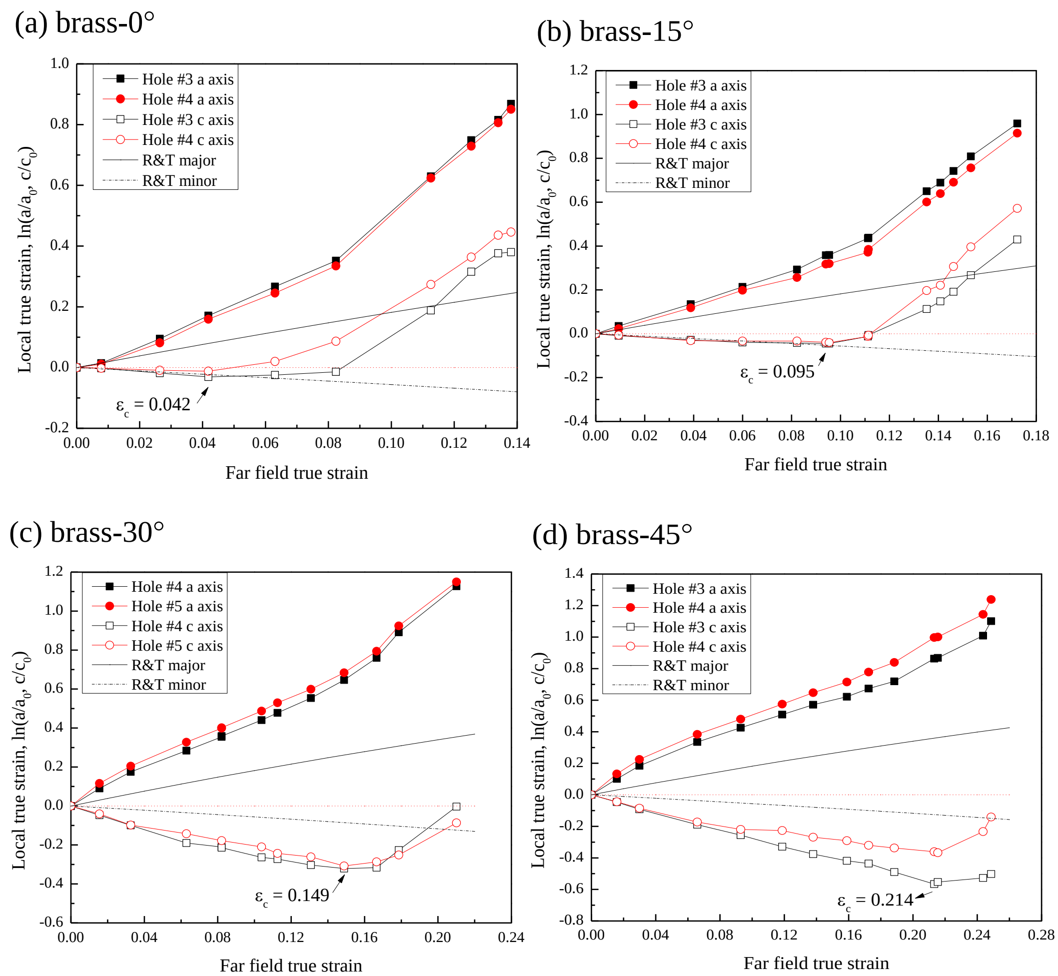

Figure 4.25: The local true strain of the first pair of voids to link plotted as a function of the far filed true strain showing the void growth and coalescence behaviors until linkage for **α-brass** samples containing a line of voids with the misorientation angle θ = (a) 0°, (b) 15°, (c) 30°, and (d) 45°. The Rice and Tracey void growth model was also plotted as a comparison with the experimental results.

During the deformation process, the voids will act as the stress concentrator and the region of the voids will elongate more in the whole gauge section. It is easy to understand that if the initial distance of the markers l_0 is set to be longer, that is, the section containing more material which elongates less than the voids, the slope of the curve in Figure 4.24 and Figure 4.25 would be gentler. Therefore because of the way the far field true strain was measured, which was based on arbitrary initial length l_0 = 460 μm, one cannot expect a perfect fitting of the curve with Rice and Tracey model. With the acknowledgement of this, it can be seen in the low far field strain region when voids grow individually, the Rice and Tracey model gives relatively good prediction of the trend of void growth in the longitudinal *a* axis and void shrinkage in the lateral *c* axis. However, when voids start to interact with each other at higher far field strain values, the model is no longer valid. This is mainly because the fact that the Rice and Tracey model was developed for an isolated spherical void in an infinite unit. The cylindrical voids in the current 2-D experiments are also under complex stress state which is discrepant with the model.

Moreover, the longitudinal diameter was increasing all the way during the tensile test. The lateral diameter was decreasing until the coalescence event was triggered. After that, voids started expanding towards their neighbor with the similar slope to the longitudinally expanding. Hence, in the current work, we keep the same way defining the onset of coalescence as the point when voids stop shrinkage in the lateral direction, and this is different from the coalescence concept by Weck and Wilkinson (2008) which is the point of ligament failure.

4.3.7.2 Brown and Embury model

The Brown and Embury model for void coalescence indicates that coalescence occurs when shear bands at 45° can be drawn between the voids meaning that the void length is equal to the intervoid spacing. Therefore, it can be validated by plotting the major void diameter and the intervoid distance as a function of far field true strain or local true strain. The intersection of the two curves represents the coalescence strain as shown in Figure 4.26 to Figure 4.29.

Weck and Wilkinson (2008) used the edge to edge distance to plot the prediction value of the model Figure 4.30(b) and the coalescence strain they used was the experimental linkage strain for comparison. Looking at this in another way, it is straightforward to see from Figure 4.16(a) that, for large voids with close intervoid spacing in the current work, it is not reasonable to use the edge to edge distance as the intervoid distance by Weck et al. (2008) when the angle φ is less than 45° in Figure 4.30(b). The same misinterpretation of the intervoid distance concept by Brown and Embury has also been found in other works (Seppälä et al. (2004)). Therefore, the intervoid distance used to compare with the Brown and Embury model was the pole to pole distance and this method was also been validated and utilized by others (Ma et al. (2011, 2012), Landron et al. (2013)). When void length $2a$ grows until it reaches the intervoid distance, the requirement of this model can be met. The comparisons of the experimental data with the Brown and Embury prediction were shown in Table 4.1. The method used by Weck and

Wilkinson (2008) was also plotted as a comparison by using the experimental linkage strain as the coalescence strain.

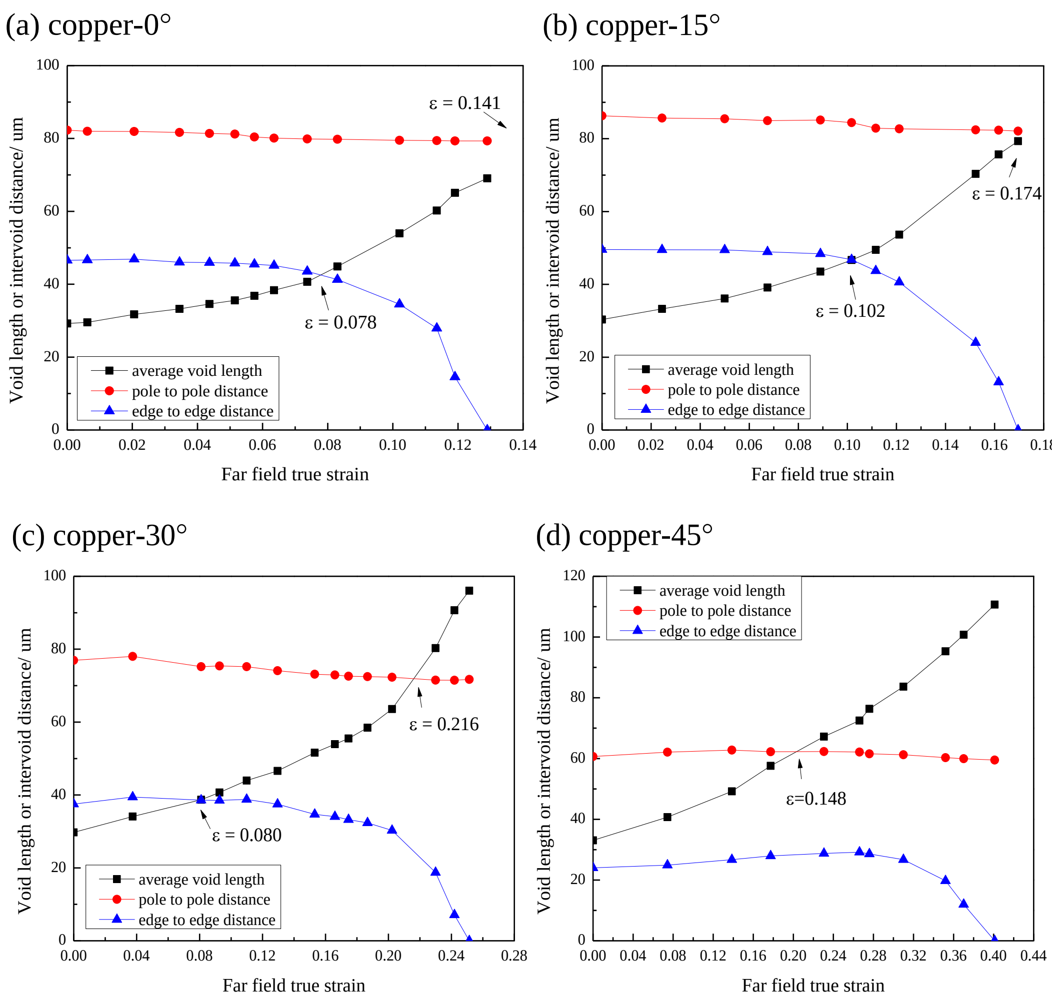

Figure 4.26: Average length of the first pair of voids to link and the intervoid distance plotted as a function of far field true strain for **pure copper** samples containing a line of voids with the misorientation angle θ = (a) 0°, (b) 15°, (c) 30°, and (d) 45°.

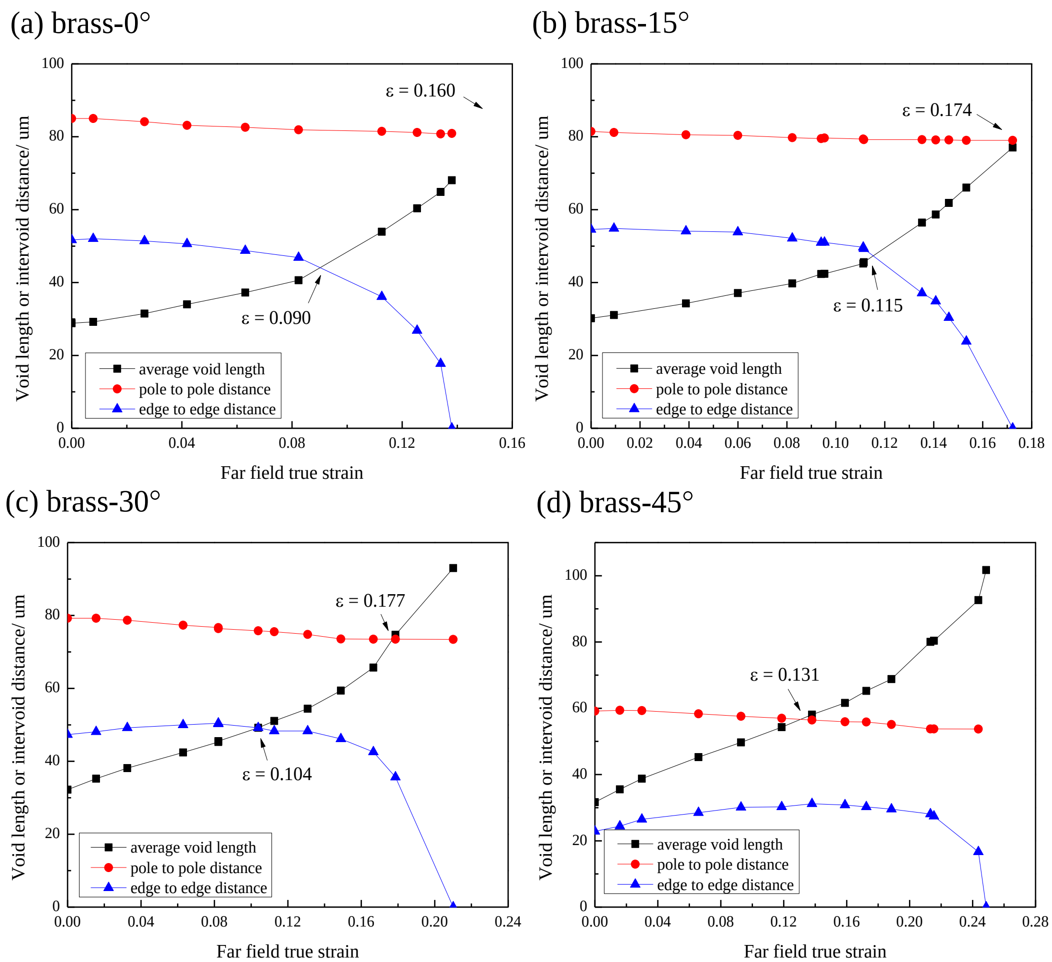

Figure 4.27: Average length of the first pair of voids to link and the intervoid distance plotted as a function of far field true strain for **α-brass** samples containing a line of voids with the misorientation angle θ = (a) 0°, (b) 15°, (c) 30°, and (d) 45°.

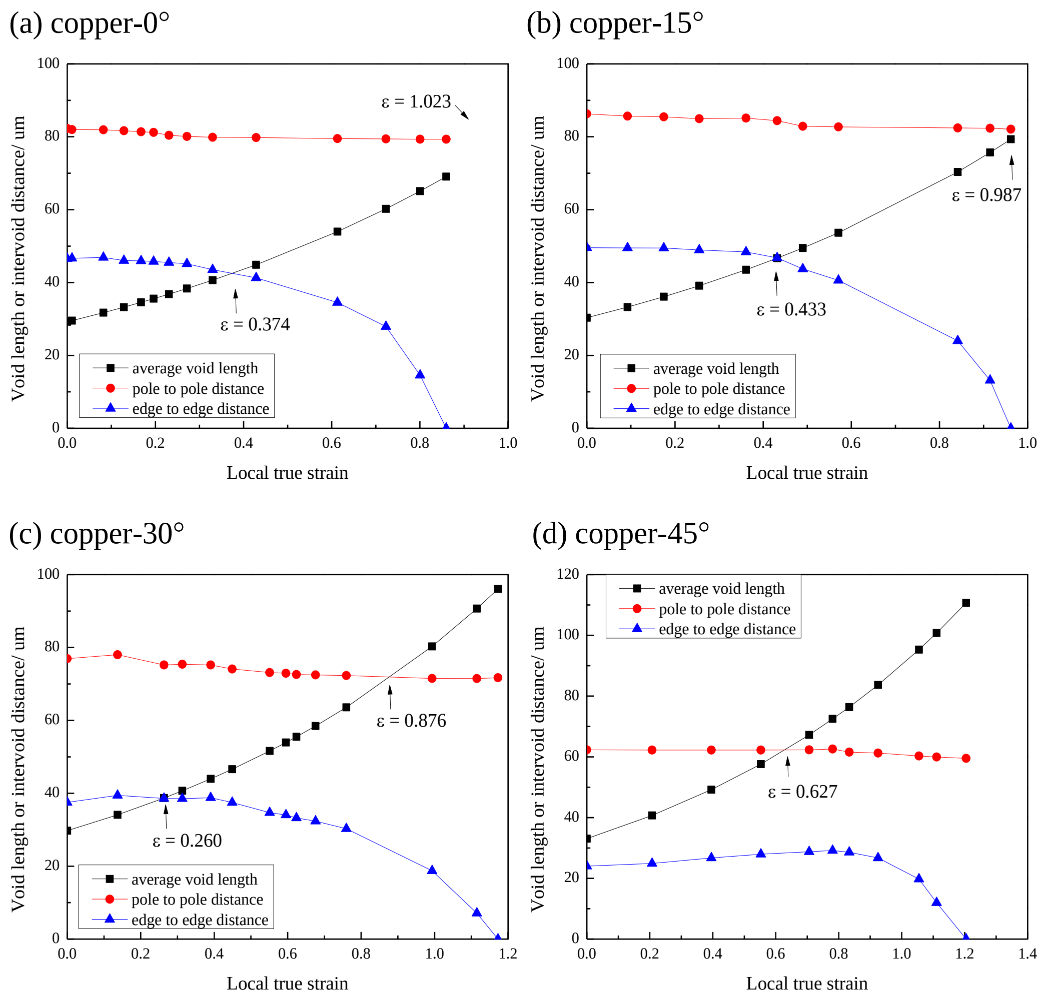

Figure 4.28: Average length of the first pair of voids to link and the intervoid distance plotted as a function of local true strain for **pure copper** samples containing a line of voids with the misorientation angle θ = (a) 0°, (b) 15°, (c) 30°, and (d) 45°.

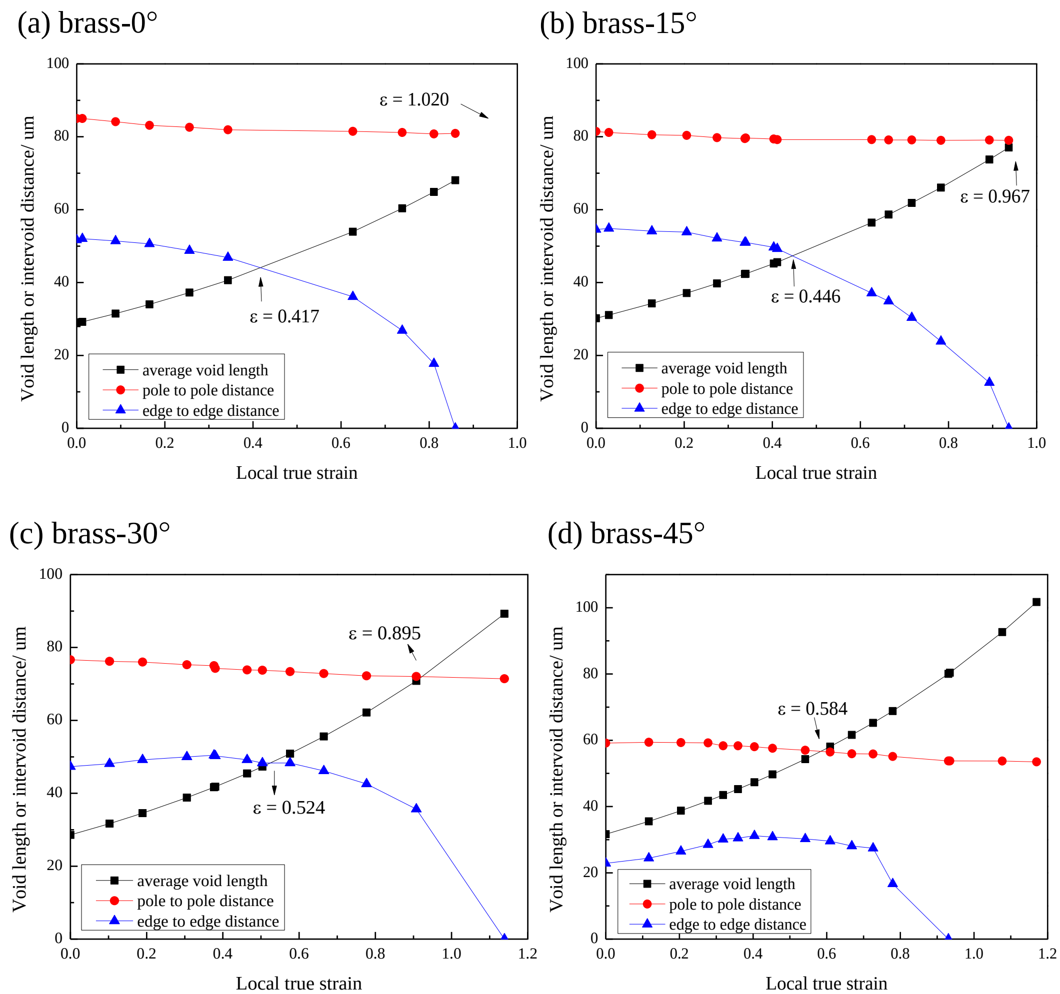

Figure 4.29: Average length of the first pair of voids to link and the intervoid distance plotted as a function of local true strain for **α-brass** samples containing a line of voids with the misorientation angle θ = (a) 0°, (b) 15°, (c) 30°, and (d) 45°.

Table 4.1: Experimental coalescence and linkage strain for different void configurations in pure copper and brass samples and the corresponding prediction from the Brown and Embury model and Thomason model.

Configurations		Cu-0 °	Cu-15 °	Cu-30 °	Cu-45 °	brass-0 °	brass-15 °	brass-30 °	brass-45 °
Coalescence far field strain		0.057	0.067	0.202	0.31	0.042	0.095	0.149	0.214
Coalescence local strain		0.231	0.255	0.449	0.925	0.165	0.34	0.615	0.932
Linkage far field strain		0.129	0.17	0.251	0.401	0.138	0.172	0.21	0.249
Linkage local strain		0.86	0.962	1.173	1.205	0.859	0.937	1.065	1.17
Brown and Embury	Far field strain	0.141	0.174	0.216	0.203	0.16	0.174	0.177	0.131
	Difference (%)	147.4	159.7	6.9	-34.5	281.0	83.2	18.8	-38.8
	Local strain	1.023	0.987	0.876	0.627	1.02	0.967	0.941	0.584
	Difference (%)	342.9	287.1	95.1	-32.2	518.2	184.4	53	-37.3
Weck Method Brown and Embury	Difference (far field) (%)	9.3	2.4	-13.9	-49.4	15.9	1.2	-15.7	-47.4
	Difference (local) (%)	19.0	2.6	-25.3	-48.0	18.7	3.2	-11.6	-50.1
Thomason	Far field strain	0.116	0.145	0.205	0.401	0.123	0.139	0.158	0.247
	Difference (%)	103.5	116.4	1.5	29.4	192.9	46.3	6.0	15.4
	Local strain	0.763	0.78	0.786	1.205	0.715	0.65	0.724	1.136
	Difference (%)	230.3	205.9	75.1	30.3	333.3	91.2	17.7	21.9

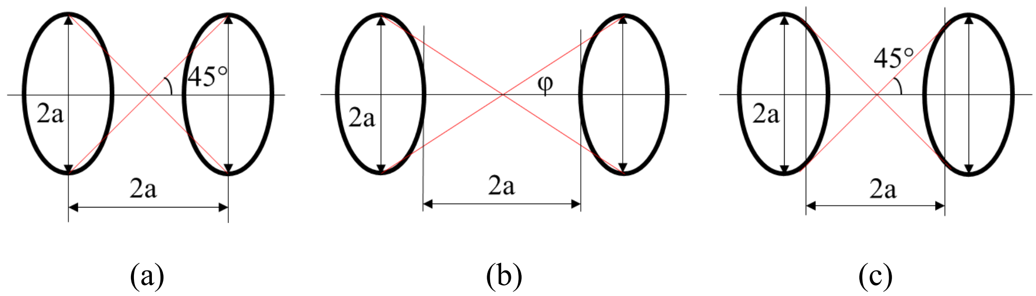

Figure 4.30: Comparison of the (a) pole to pole intervoid distance and (b) edge to edge intervoid distance when Brown and Embury coalescence criterion is met.

Hosokawa et al. (2013a, c) showed that the pole to pole distance will stop shrinking at the onset of void coalescence. However, in this study, it is found that the pole to pole distance keeps decreasing until the final fracture. Moreover, the decreasing of this distance is not significant in comparison with that by Hosokawa et al. (2013a) which decreases from 120 μm to 80 μm approximately for both of the FCC1 and FCC2 model materials. This difference may result from the different constraint condition in 3-D multi-sheet case of Hosokawa et al. (2013a) and the 2-D single sheet case in this work, as well the difference between a void array as compared to a single line of voids.

Despite of the situation addressed by the model when the shear bands can be drawn from the north pole of one void to the south pole of the other void, in the real situation for the closely located voids, however, the interaction between the voids may concentrate on a smaller area in the ligament as shown in Figure 4.30(c). Therefore, even though the shear band at 45° can still be drawn from some particular points of the voids, the premature coalescence will occur. Evidence to show this features can be found from the SEM images. This is also consistent with the poor prediction for closely arranged voids in AA 5052 by Weck and Wilkinson (2008). Under this condition, the intervoid distance to plot in the model will be some value between the pole to pole and the edge to edge distance. Therefore, both of the two distances were plotted as shown in Figure 4.26 to Figure 4.29.

Weck and Wilkinson (2008) found the prediction was in good agreement with the experimental data for voids without misorientation. However, using the current methodology which gives better interpretation of the model, it shows significant discrepancies for the copper sample. Moreover, since the Brown and Embury model was developed without considering the effect of work hardening rate of the materials, the prediction for brass 0° samples shows even larger discrepancies. For the 0° and 15° samples, the large volume fraction of voids plays a great role to localize the deformation rapidly as addressed in Section 4.35. Therefore, voids even link together without growing as long as the distance between them. This premature failure due to the volume fraction effect also results in the overestimation of the model not only by the current method but also by the method adopted by Weck and Wilkinson (2008).

For the original Brown and Embury model, only geometrical conditions were considered to achieve the coalescence. Given the voids with large misorientation and close spacing, it reaches the geometrical condition from the beginning without any deformation meaning that the prediction strain is zero. For those cases, further deformation has to be applied in order to exhaust the work hardening capacity of the ligaments between the voids which is the additional conditions for the model. This is also the reason why the Brown and Embury model underestimate the coalescence strain significantly for samples with misorientation angle $\theta = 30°$ and 45°.

4.3.7.3 Thomason model

To obtain the 2-D Thomason prediction of void coalescence strain, the left hand side (LHS) and the right hand side (RHS) of Equation (2.21) were plotted as a function of the far field true strain and local true strain for copper and brass sample respectively as shown in Figure 4.31 and Figure 4.32. The intersections of these curves suggest the coalescence strain and the values are shown in Table 4.1. Due to the 2-D condition, the stress triaxiality on the RHS is assumed to be constant all over the deformation and is taken to be the value under uniaxial tension $\sigma_m/Y = 0.33$ as the say way as described by Weck and Wilkinson (2008).

The prediction given by the Thomason model showed less discrepancy than the Brown and Embury model for all the samples, even though the prediction is still with considerable mismatch for the 0° and 15° samples. One of the reasons is that the Thomason model was produced by assuming a plane strain stress state. As the results shown in section 4.11 indicate, the current 0° and 15° experiments were designed to be far apart and tend to be under the plane stress state. The farther apart the voids are (0°), the larger the discrepancies the prediction show. The 30° and 45° samples tend to be plane strain, so there shows less dissonance especially for the Cu 30° and brass 30° far field strain prediction with only 1.5% and 6% difference, respectively. Another reason, as addressed by Weck (2007), is that the void growth data were extracted from the experimental void dimensions, not from the Rice and Tracey equation. The data points at the final stage contain those that have already coalesced which also contributes to the error. Again, the effect of local volume fraction also dominates the large discrepancies for 0° and 15° samples.

(a) copper

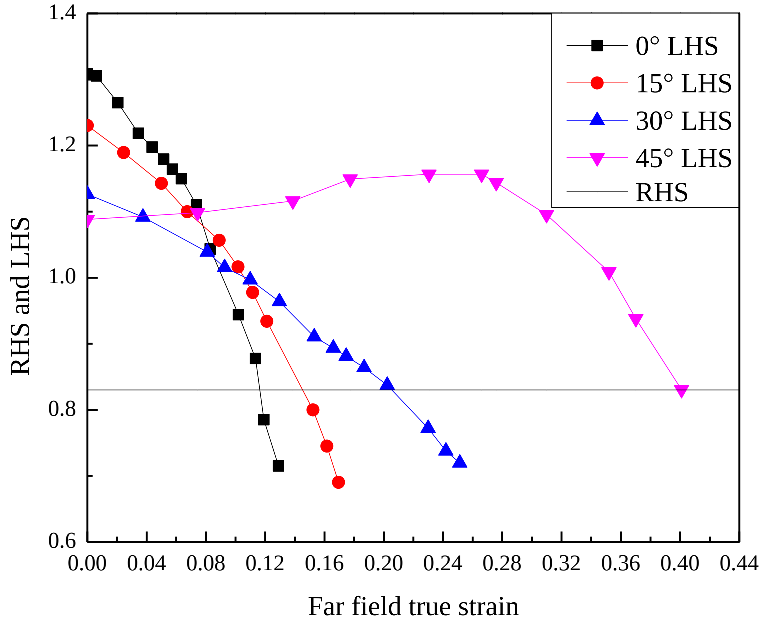

(b) α-brass

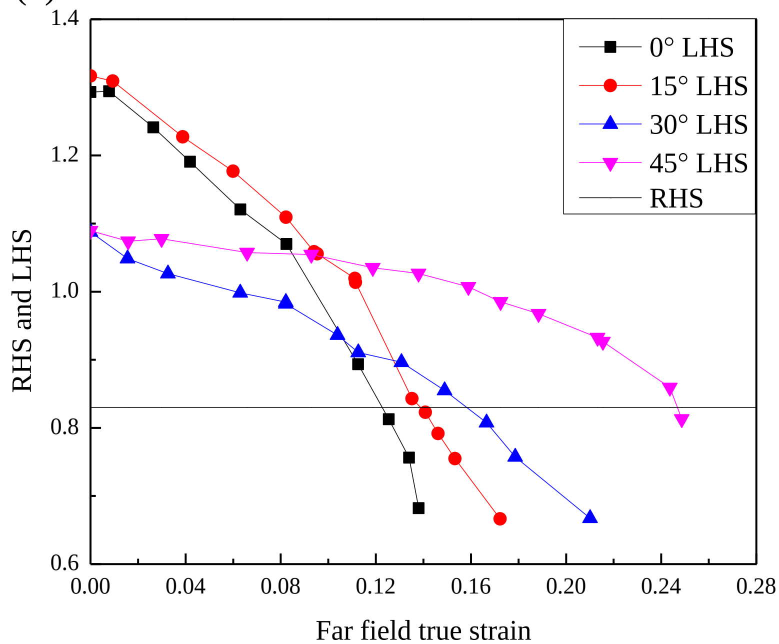

Figure 4.31: RHS and LHS of Thomason model (Equation (2.21)) plotted as a function of far field true strain for (a) pure copper and (b) α-brass samples containing various void line arrangements. The intersection of the LHS and each RHS gives the coalescence strain followed by Thomason model.

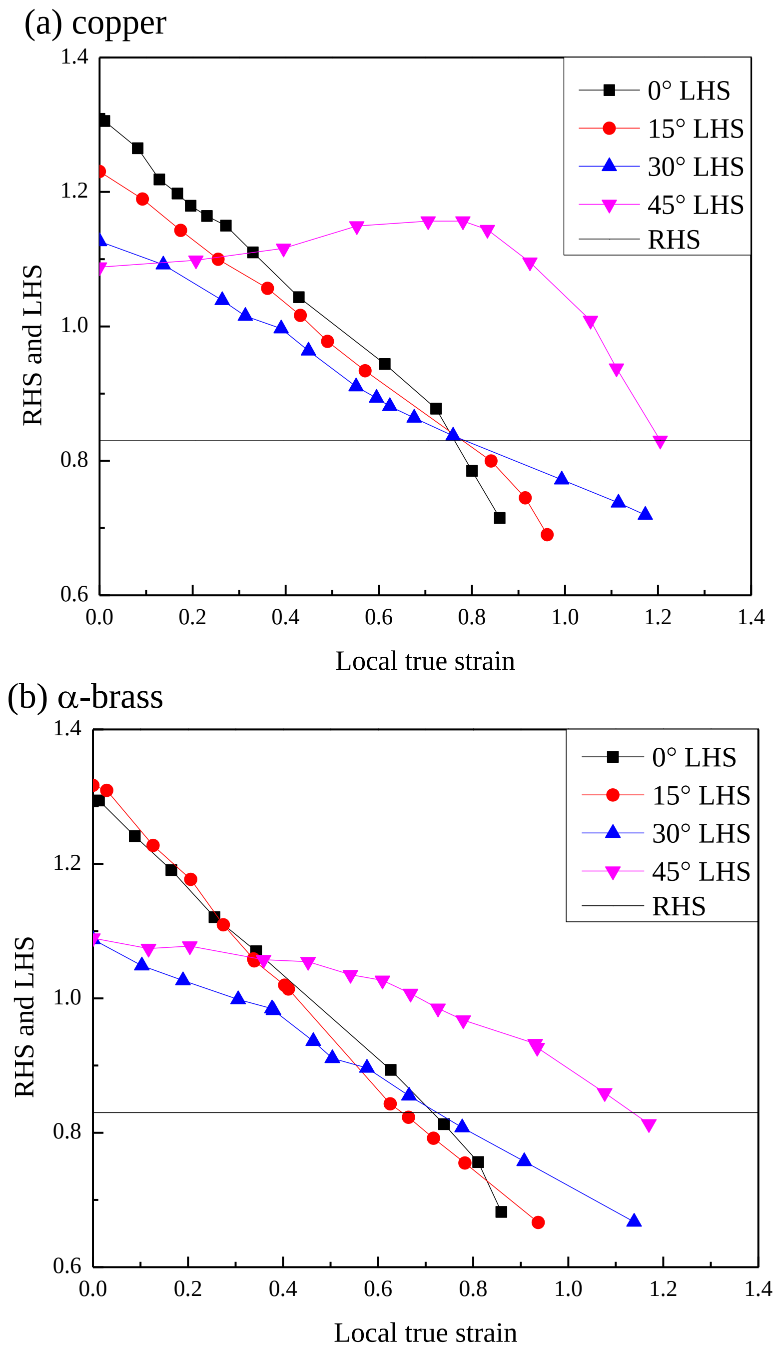

Figure 4.32: RHS and LHS of Thomason model (Equation (2.21)) plotted as a function of local true strain for (a) pure copper and (b) α-brass samples containing various void line arrangements. The intersection of the LHS and each RHS gives the coalescence strain followed by Thomason model.

4.4 3-D X-ray Tomography Examinations

In order to examine the void growth behavior through the thickness of the sample, a commercial software called Dataviewer was used to slice the sample in a different layer as shown in Figure 4.29. Since the simple 2-D examination adopted in the major part of this work was limited to the information of one surface, the behavior behind can never be visualized. From the figure, we found that even starting with a cylindrical void through the thickness, the voids visualized in the SEM have linked together. On the other hand, the ligaments sliced in the middle layer was still joining. Thus, the stress state during deformation is complex, sometimes neither pure plane stress nor plane strain. Even for the 2-D single sheet model material, it is still not confirmed to describe the void growth and coalescence behaviors by purely using 2-D measurements.

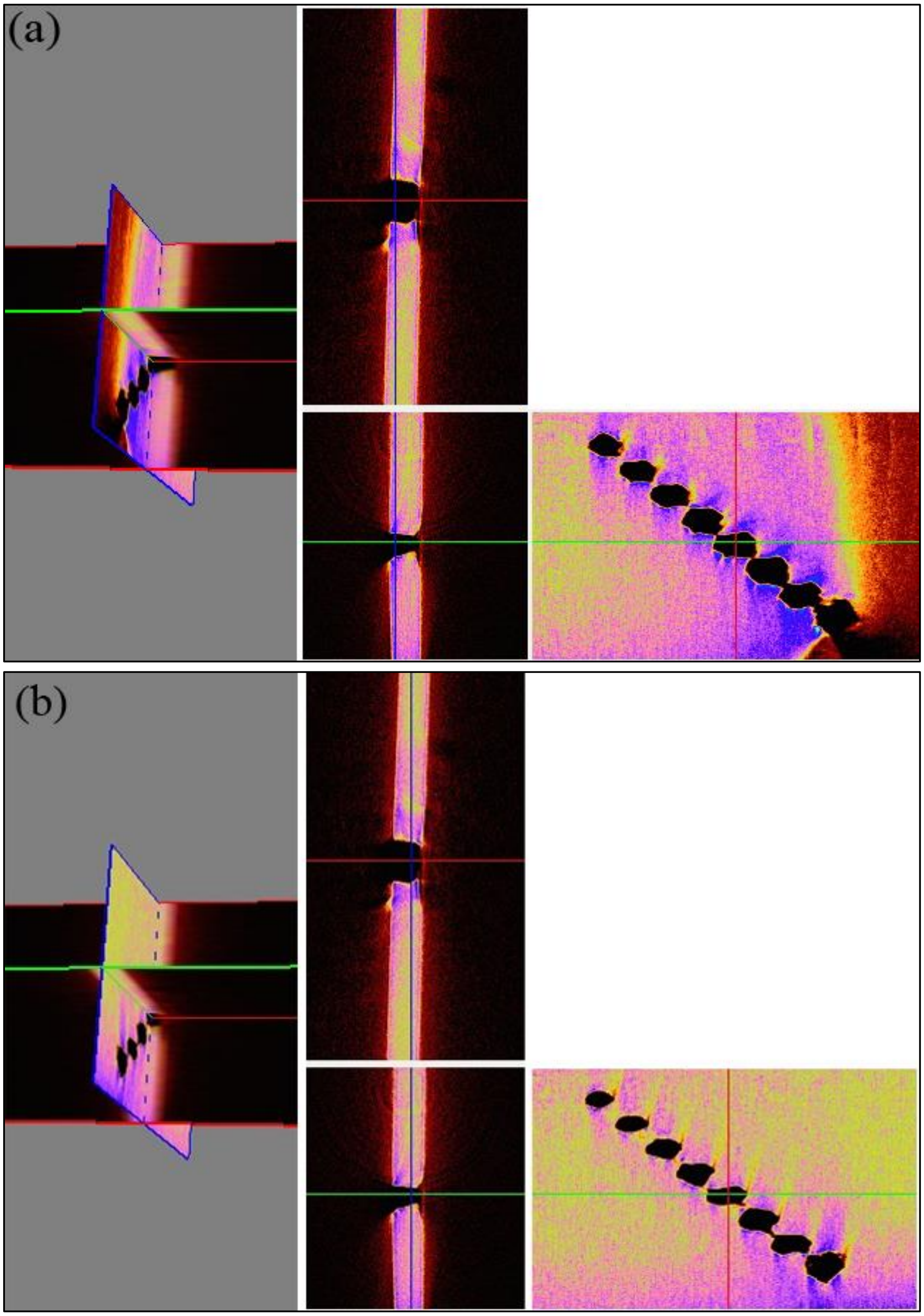

Figure 4.33: Three plane projection images of a brass sample cutting at a layer (a) near the bottom and (b) in the middle layer.

Chapter 5

Conclusions and Future Work

This thesis was focused on visualizing the void growth and coalescence behaviors during the deformation process in the 2-D model materials. The effect of void orientation was studied in detail to explore the effect of shear localization mechanism on the ductile fracture process. Detailed quantitative experimental results were collected to compare with the classic models. The main contributions of this work were listed as follows:

- A series of 2-D model materials were fabricated in pure copper and α-brass samples containing laser drilled holes with the misorientation angle $\theta = 0°$, 15°, 30°, and 45°.

- The void growth sequences were recorded in detail and the coalescence and linkage strain was successfully captured in the 2-D single sheet model materials.

- At the onset of coalescence, the lateral diameter of voids was found to stop shrinking, however, the pole to pole intervoid distance did not. This is the first time this level of detailed information was captured in the 2-D model materials.

- Prior to coalescence, the voids rotated with the decreasing of void orientation and the ligament length showed a tendency of increasing for 30° and 45° samples which is also the first time to be visualized in the 2-D model materials.

- The effect of orientation angle on the coalescence and linkage strain was systematically studied with a line of voids with the misorientation angle θ = 0°, 15°, 30°, and 45°.

- The local volume fraction, together with the shear localization impacts on the coalescence and linkage events and the effect of local volume fraction dominates in this study.

- The void growth behavior followed the tendency of Rice and Tracey model.

- The prediction of Brown and Embury model showed large discrepancies for the studied samples using the current measurement methodology.

- Thomason model could not give reliable prediction for samples with 0° and 15° misorientation because of the stress state was different with the initial assumption of the model. Better agreement with the experimental value was found for samples with 30° and 45° misorientation, especially the 30° sample.

Since the quantitative experimental data to visualize the void coalescence process is still in great need, this work provided some information for exploring this field further. We still suggest more experimental efforts to overcome the problems of this work and help to understand the void coalescence better. These improvements are described as follows:

- The size and regularity of the voids play a great role in the growth and coalescence process. Also, the coalescence is known to be influenced by the aspect ratio, intervoid spacing, and if the voids are perfectly cylindrical or tapered through thickness. Therefore, it is crucial to develop practical techniques using the ultrafast laser to drill holes with controllable parameters.

- The local volume fraction of the voids play a greater role than the shear localization in the current experiment with 0° and 15° misorientation. The growth of the local plasticity in the ligaments is still not clear for the case with large and closely located voids. Therefore, it is helpful to use the finite element modeling to explore how these effects correlate.

- As addressed in the literature review and the results shown in section 4.4, the two-dimensional method is limited to the surface visualization which cannot predict the void behavior on the overall situation. The previous work also showed different prediction results of the classic models compared with the experiment data. Thus, it is important to develop sandwiched 3-D model materials to detect the void growth and coalescence in the bulk.

References

Argon, A., Im, J. and Safoglu, R. (1975). Metallurgical and Materials Transactions A 6(4): 825-837.

Argon, A. S. and Im, J. (1975). Metallurgical Transactions A 6(4): 839-851.

Babout, L., Brechet, Y., Maire, E. and Fougeres, R. (2004). Acta Materialia 52(15): 4517-4525.

Babout, L., Maire, E., Buffiere, J. Y. and Fougeres, R. (2001). Acta Materialia 49(11): 2055-2063.

Babout, L., Maire, E. and Fougeres, R. (2004). Acta Materialia 52(8): 2475-2487.

Bandstra, J. P., Goto, D. M. and Koss, D. A. (1998). Materials Science and Engineering A 249(1-2): 46-54.

Bannister, M. and Ashby, M. F. (1991). Acta Metallurgica et Materialia 39(11): 2575-2582.

Barsoum, I. and Faleskog, J. (2011). International Journal of Solids and Structures 48(6): 925-938.

Beckmann, F., Grupp, R., Haibel, A., Huppmann, M., Noethe, M., Pyzalla, A., Reimers, W., Schreyer, A. and Zettler, R. (2007). Advanced Engineering Materials 9(11): 939-950.

Benzerga, A. A. (2002). Journal of the Mechanics and Physics of Solids 50(6):

1331-1362.

Benzerga, A. A., Besson, J. and Pineau, A. (2004). Acta Materialia 52(15): 4623-4638.

Brocks, W., Sun, D. Z. and Honig, A. (1995). International Journal of Plasticity 11(8): 971-989.

Brown, L. M. and Embury, J. D. (1973). Institute of Metals (London), Monograph and Report Series 1(3): 164-169.

Brown, L. M. and Stobbs, W. M. (1976). Philosophical Magazine 34(3): 351-372.

Buffiere, J. Y., Maire, E., Cloetens, P., Lormand, G. and Fougeres, R. (1999). Acta Materialia 47(5): 1613-1625.

Butcher, C. and Chen, Z. T. (2009). Modelling and Simulation in Materials Science and Engineering 17(2): 025007.

Chen, C. W. (1961). Acta Metallurgica 9(1): 68-71.

Cormack, A., (1963). Journal of Applied Physics, 34:2722-2727.

Cormack, A., (1964). Journal of Applied Physics, 35:2908-2913.

Cox, T. and Low, J. (1974). Metallurgical and Materials Transactions B 5(6): 1457-1470.

Faleskog, J. and Shih, C. F. (1997). Journal of the Mechanics and Physics of Solids 45(1): 21-50.

French, I. E. and Weinrich, P. F. (1974). Scripta Metallurgica 8(2): 87-90.

Gammage, J., Wilkinson, D., Brechet, Y. and Embury, D. (2004). Acta Materialia

52(18): 5255-5263.

Garrison, W. M. and Moody, N. R. (1987). Journal of Physics and Chemistry of Solids 48(11): 1035-1074.

Gologanu, M., Leblond, J., Perrin, G., and Devaux, J. (1997). In P. Suquet (Ed.), Continuum micromechanics (CISM Courses and Lectures no. 377: 61-130). New York: Springer.

Goods, S. H. and Brown, L. M. (1979). Acta Metallurgica 27(1): 1-15.

Gupta, C., Van de Casteele, E. and Chakravartty, J. K. (2009). Nuclear Instruments & Methods in Physics Research Section B-Beam Interactions with Materials and Atoms 267(20): 3488-3490.

Gurland, J. and Plateau, J. (1963). The mechanism of ductile rupture of metals containing inclusions. Trans. ASM., 56:442.

Gurson, A. L. (1977). Journal of Engineering Materials and Technology 99(1): 2-15.

Hounsfield, G., (1972). Patent Specification 1283915, (1283915).

Hosokawa, A., Wilkinson, D. S., Kang, J. D. and Maire, E. (2012). Acta Materialia 60(6-7): 2829-2839.

Hosokawa, A., Wilkinson, D. S., Kang, J. and Maire, E. (2013a). Acta Materialia 61(4): 1021-1036.

Hosokawa, A., Wilkinson, D. S., Kang, J., Kobayashi, M. and Toda, H. (2013b). International Journal of Fracture: 1-16.

Hosokawa, A., Wilkinson, D. S., Kang, J. and Maire, E. (2013c). Philosophical

Magazine Letters: 1-8.

Hosokawa A., (2011). McMaster University, Ph. D. thesis.

Huber, G., Brechet, Y. and Pardoen, T. (2005). Acta Materialia 53(9): 2739-2749.

Jia, S., Raiser, G. F. and Povirk, G. L. (2002). International Journal of Solids and Structures 39(9): 2517-2532.

Kadkhodapour, J., Butz, A. and Rad, S. Z. (2011). Acta Materialia 59(7): 2575-2588.

Kailasam, M. and Ponte Castañeda, P. (1998). Journal of the Mechanics and Physics of Solids 46(3): 427-465.

Kanetake, N., Nomura, M. and Choh, T. (1995). Materials Science and Technology 11(12): 1246-1252.

Koplik, J. and Needleman, A. (1988). International Journal of Solids and Structures 24(8): 835-853.

Kuna, M. and Sun, D. Z. (1996). International Journal of Fracture 81(3): 235-258.

Landron, C., Bouaziz, O., Maire, E. and Adrien, J. (2010). Scripta Materialia 63(10): 973-976.

Landron, C., Maire, E., Bouaziz, O., Adrien, J., Lecarme, L. and Bareggi, A. (2011). Acta Materialia 59(20): 7564-7573.

Landron, C., Bouaziz, O., Maire, E., and Adrien, J. (2013). Acta Materialia. Accepted.

Leblond, J.-B., and Mottet, G. (2008). Comptes Rendus Mécanique 336(1–2): 176-

189.

Le Roy, G., Embury, J. D., Edward, G. and Ashby, M. F. (1981). Acta Metallurgica 29(8): 1509-1522.

Magnusen, P. E., Dubensky, E. M. and Koss, D. A. (1988). Acta Metallurgica 36(6): 1503-1509.

Maire, E., Babout, L., Buffiere, J. Y. and Fougeres, R. (2001). Materials Science and Engineering A 319: 216-219.

Maire, E., Carmona, V., Courbon, J. and Ludwig, W. (2007). Acta Materialia 55(20): 6806-6815.

McClintock, F. A. (1968a). International Journal of Fracture Mechanics 4(2): 101-130.

McClintock, F. A. (1968b). Journal of Applied Mechanics 35(2): 363-371.

Murr, L., (1975) Interfacial Phenomena in Metals and Alloys. Addison-Wesley.

Nagaki, S., Nakayama, Y. and Abe, T. (1998). International Journal of Mechanical Sciences 40(2-3): 215-226.

Needleman, A. and Tvergaard, V. (1987). Journal of the Mechanics and Physics of Solids 35(2): 151-183.

Nahshon, K. and Hutchinson, J. W. (2008). European Journal of Mechanics A-solids 27(1): 1-17.

Nutt, S. R. and Needleman, A. (1987). Scripta Metallurgica 21(5): 705-710.

Pan, X., Wu, X. L., Mo, K., Chen, X. A., Almer, J., Ilavsky, J., Haeffner, D. R. and

Stubbins, J. F. (2010). Journal of Nuclear Materials 407(1): 10-15.

Pardoen, T. and Hutchinson, J. W. (2000). Journal of the Mechanics and Physics of Solids 48(12): 2467-2512.

Ponte Castañeda, P. and Zaidman, M. (1994). Journal of the Mechanics and Physics of Solids 42(9): 1459-1497.

Puttick, K. E. (1959). Philosophical Magazine 4(44): 964-969.

Puttick, K. E. (1963). Acta Metallurgica 11(8): 986-989.

Pyzalla, A., Camin, B., Buslaps, T., Di Michiel, M., Kaminski, H., Kottar, A., Pernack, A. and Reimers, W. (2005). Science 308(5718): 92-95.

Rahman, M. A., Butcher, C. and Chen, Z. T. (2012). International Journal of Fracture 177(2): 129-139.

Rice, J. R. and Tracey, D. M. (1969). Journal of the Mechanics and Physics of Solids 17(3): 201-217.

Scheck, C. and Zupan, M. (2011). Scripta Materialia 65(12): 1041-1044.

Scheyvaerts, F., Onck, P. R., Tekoglu, C. and Pardoen, T. (2011). Journal of the Mechanics and Physics of Solids 59(2): 373-397.

Seppälä, E. T., Belak, J. and Rudd, R. E. (2004). Physical Review Letters 93(24): 245503.

Tanaka, K., Mori, T. and Nakamura, T. (1970). Philosophical Magazine 21(170): 267-279.

Taylor, K. L. and Sherry, A. H. (2012). Acta Materialia 60(3): 1300-1310.

Thomason, P. F. (1968). Journal of the Institute of Metals 96: 360-365.

Thomason, P. F. (1985a). Acta Metallurgica 33(6): 1079-1085.

Thomason, P. F. (1985b). Acta Metallurgica 33(6): 1087-1095.

Thomason, P. F. (1990). Ductile fracture of metals, Pergamon Press.

Toda, H., Maire, E., Yamauchi, S., Tsuruta, H., Hiramatsu, T. and Kobayashi, M. (2011). Acta Materialia 59(5): 1995-2008.

Tvergaard, V. and Needleman, A. (1984). Acta Metallurgica 32(1): 157-169.

Tvergaard, V. (2008). International Journal of Mechanical Sciences 50(10-11): 1459-1465.

Tvergaard, V. and Nielsen, K. L. (2010). Journal of the Mechanics and Physics of Solids 58(9): 1243-1252.

Weck, A., Wilkinson, D. S., Toda, H. and Maire, E. (2006). Advanced Engineering Materials 8(6): 469-472.

Weck, A. (2007). McMaster University, Ph. D. thesis.

Weck, A. and Wilkinson, D. S. (2008). Acta Materialia 56(8): 1774-1784.

Weck, A., Wilkinson, D. S., Maire, E. and Toda, H. (2008). Acta Materialia 56(12): 2919-2928.

Weinrich, P. F. and French, I. E. (1976). Acta Metallurgica 24(4): 317-322.

Williams, J. J., Flom, Z., Amell, A. A., Chawla, N., Xiao, X. and De Carlo, F. (2010). Acta Materialia 58(18): 6194-6205.

Worswick, M. J. and Pick, R. J. (1990). Journal of the Mechanics and Physics of Solids 38(5): 601-625.

Zhao, D., Tuler, F. R. and Lloyd, D. J. (1994). Acta Metallurgica et Materialia 42(7): 2525-2533.